Remote Sensing Series 79

Elías Méndez Domínguez

Change Detection with Synthetic Aperture Radar Imagery

Remote Sensing Laboratories
Department of Geography
University of Zurich, 2018

Front page: Detection of the slewing of a crane using synthetic aperture radar tomography. Change map overlaid on the reference amplitude 3D radar image. Green and red voxels indicate changed areas. Acquisition made using the MEMPHIS sensor over Hinwil, Switzerland in 2009.

Méndez Domínguez, Elías

Change Detection with Synthetic Aperture Radar Imagery

Remote Sensing Series, Vol. 79
Remote Sensing Laboratories, Department of Geography, University of Zurich
Switzerland, 2018

ISBN: 978-3-906894-08-9

The following thesis was accepted by the Faculty of Science at the University of Zurich in the fall semester 2018.

Doctoral committee: Prof. Dr. Michael E. Schaepman (Head), Dr. Daniel Henke (PhD advisor), Dr. David Small, Prof. Dr. Alexander Damm-Reiser. External examiner: Prof. Dr. Lorenzo Bruzzone (University of Trento, Italy).

Change Detection with Synthetic Aperture Radar Imagery

Dissertation

zur

Erlangung der naturwissenschaftlichen Doktorwürde
(Dr. sc. nat.)

vorgelegt der

Mathematisch-naturwissenschaftlichen Fakultät

der

Universität Zürich

von

Elías Méndez Domínguez

aus

Spanien

Promotionskommission

Prof. Dr. Michael E. Schaepman (Vorsitz)
Dr. Daniel Henke (Leitung der Dissertation)
Dr. David Small
Prof. Dr. Alexander Damm-Reiser
Prof. Dr. Lorenzo Bruzzone

Zürich, 2018

SUMMARY

Image change detection is defined as a technique comparing a pair of images of the same geographical area acquired at different times. This technique enables mapping applications for Earth environmental observation, risk management, human activity monitoring and urban studies. Radar sensors are particularly suitable for these applications as they are able to realiably provide high resolution imagery over large areas at low cost.

In change detection with radar images, the extent of most error sources hinges upon the accuracy and consistency of the focusing algorithm in use, and therefore, the characteristics of the resulting images. In this work, the processing chain of the Synthetic Aperture Radar (SAR) data is utilized in the change detection procedure to extract additional information on the targets and image artifacts, with the main goal of improving overall performance.

Within this thesis, diverse airborne SAR experiments were conducted for change detection purposes focusing on human activity monitoring and urban studies. The experiments were carried out with two high-resolution frequency agile sensors operating at X- and Ka-band respectively. In the first chapter, diverse pulse compression approaches applied to the signals acquired in the range dimension were studied and evaluated for SAR image focusing purposes. The study showed that adaptive processing methods yielded images with slightly higher spatial resolution and lower sidelobes while producing a negligible signal to noise ratio loss in comparison to that achieved with typical deterministic approaches. In the second chapter, a change detection method exploiting spatial information gathered by means of multisquint processing was designed to reduce errors caused by the presence of image artifacts. The kappa coefficient improved on average by a factor 1.9 while preserving 95% of the detection rate obtained with traditional techniques. The change detector was also shown to be less sensitive to errors caused by small differences between the acquisition geometries. Complementing the two previous research areas, the performance offered by adaptive and multisquint processing to reduce errors caused by image artifacts is analyzed in chapter three. Results showed that adaptive and multisquint processing improved the kappa coefficient by at least a factor 1.22 when applied separately in comparison to that offered by the SAR images focused with deterministic approaches and single-look processing. This factor rose to 1.86 when range adaptive pulse compression and multisquint processing mode were utilized in combination. In chapter four, a change detector exploiting the 2-D and 3-D SAR image focusing chain was designed to improve the performance offered by other approaches based on 2-D or 3-D information only. The method takes advantage of the 2-D SAR focusing chain by using spatial information gathered via multisquint processing to reduce errors caused by artifacts without significantly increasing computation time. It also benefited from the volumetric structure of the targets, and a more accurate backscatter estimate of the objects, obtained after performing pulse compression with the signals acquired in the normal dimension. Evaluation of the kappa coefficient showed that the proposed method performed well at detecting changes caused by short and tall targets. Combination of backscatter and height difference information using a conditional random field led to the best performance.

This thesis contributes to broadening the knowledge of SAR image formation techniques and provides performance improvements in change detection methods, proving that change detection with SAR imagery delivers more reliable results when the processing chain participates in the change detection procedure. The dissertation concludes with a discussion of the main findings and possible future research lines.

ZUSAMMENFASSUNG

Als Image Change Detection definiert man eine Technik, die Paare von Bildern derselben geografischen Region, die aber zu unterschiedlichen Zeitpunkten aufgenommenen wurden, vergleicht. Solche Techniken werden zur Kartierung verwendet, um z.B. in der Erdbeobachtung, beim Risikomanagement, zur Überwachung menschlicher Aktivitäten und in der Urbanistik angewendet zu werden. Für solche Zwecke besonders geeignet sind Radarsensoren, da sie zuverlässig und günstig hochaufgelöste Bilder von großen Flächen liefern können.

Bei der Change Detection von Radarbildern hängen die meisten Fehler von der Genauigkeit und Robustheit des verwendeten Fokussierungsalgorithmus' und damit von den Charakteristika der prozessierten Bilder ab. In der vorliegenden Arbeit trägt die Prozessierungskette der Synthetic Aperture Radar-Daten (SAR) durch Informationsgewinn über Ziele und Bildartefakte zur Change Detection mit dem primären Ziel bei, dessen Gesamtleistung zu verbessern.

Im Rahmen der Arbeit wurden verschiedene luftgestützte SAR-Experimente zur Change Detection durchgeführt, wobei der Schwerpunkt auf der Urbanistik und der Überwachung menschlicher Aktivitäten lag. Die Experimente wurden mit zwei hochauflösenden frequenzagilen Sensoren im X-Band und im Ka-Band durchgeführt. Im ersten Kapitel wurden verschiedene Ansätze zur Range-Pulskompression der erfassten Signale untersucht und ihre Anwendbarkeit für die SAR-Bildfokussierung ausgewertet. Der Vergleich zwischen adaptiven Methoden und herkömmlichen deterministischen Ansätzen zeigte bei ersteren eine leicht höhere räumliche Auflösung und kleinere Nebenkeulen bei einem vernachlässigbar geringeren Signal-Rausch-Verhältnis. Im zweiten Kapitel wurde eine Change Detection-Methode entwickelt, die mittels Multisquint Prozessierung räumliche Informationen nutzt, um Fehler durch Bildartefakte zu reduzieren. Der Kappa-Koeffizient verbesserte sich durchschnittlich um einen Faktor von 1,9 bei einer Erkennungsrate von 95% im Vergleich zu herkömmlichen Techniken. Auch erwies sich der Algorithmus als robuster gegenüber Fehlern, die durch geringfügig unterschiedliche Erfassungsgeometrien verursacht werden. Ergänzend zu den vorhergehenden Forschungsarbeiten wird im dritten Kapitel die Leistungsfähigkeit der adaptiven und der Multisquint Prozessierung zur Reduktion der von Bildartefakten verursachten Fehlern analysiert. Die separate Anwendung adaptiver und Multisquint Prozessierung verbesserten den Kappa-Koeffizienten um einen Faktor von mindestens 1,22 im Vergleich zu deterministischen Ansätzen und Single-Look-Verarbeitung, die Kombination beider erhöhte ihn auf 1,86. Im vierten Kapitel wird ein Change Detection-Algorithmus vorgestellt, der 2-D- und 3-D-SAR-Fokussierung kombiniert, um die Leistungsfähigkeit gegenüber reinen 2-D- oder 3-D-Ansätzen zu verbessern. Das Verfahren nutzt die aus der 2-D-Multisquint-Prozessierung hergeleiteten räumlichen Informationen aus, um ohne signifikant höhere Rechenzeit die durch Bildartefakte verursachten Fehler zu reduzieren. Nach der Pulskompression in der zur Range-Azimut-Ebene orthogonalen Dimension führen die so zusätzlich gewonnenen Informationen der dritten Dimension und die präzisere Abschätzung der Rückstreuung zu verbesserten Ergebnissen. Die Auswertung zeigt, dass diese Methode bei der Zielerkennung sowohl in geringen als auch in großen Höhen gut funktioniert. Die besten Ergebnisse wurden mittels eines Conditional Random Fields erzielt, das die Differenzen der Rückstreuung und der Höhen kombiniert.

Die vorliegende Arbeit erweitert unser Wissen über die SAR-Prozessierung, erhöht die Leistungsfähigkeit von Change Detection-Methoden und zeigt auf, dass SAR-Change Detection durch die Integration der Bildfokussierung in den Change Detection-Prozess zuverlässiger gemacht werden kann. Die Dissertation schließt ab mit einer Diskussion der wichtigsten Ergebnisse und Vorschlägen für zukünftige Forschungsrichtungen.

TABLE OF CONTENTS

1 INTRODUCTION

1.1 Background

Remote sensing encompasses methods and technologies to retrieve information about the Earth's surface measured at a distance using electromagnetic radiation reflected or emitted from the Earth's surface [1]. It provides spatial information for both monitoring human activity and its impact on planet Earth and understanding the interactions of natural and man-made processes.

Depending on the source of electromagnetic radiation, there are two classes of remote sensing systems, active and passive. Passive systems measure the radiation reflected from targets illuminated with a natural source, like the sun, or naturally emitted, like thermal radiation. Active sensors provide their own source for illumination, emitting radiation towards the surface under investigation and measuring the reflected radiation. Active sensors can be divided into lidar (light detection and ranging) and radar (radio detection and ranging). Lidar employs a laser as the source of radiation and operates in the optical part of the electromagnetic spectrum. Radar employs a set of antennae to transmit electromagnetic waves and receive the corresponding backscattered field. Radar operates in the microwave and radio parts of the electromagnetic spectrum.

Major topics in remote sensing are related to agriculture, forestry, biodiversity, 3-D city modelling, risk management and urban studies [1]. There, identification and understanding of changes on the Earth's surface by time series data analysis is important, as changes in the current state of our environment have a natural and socio-economic impact ranging at different scales from local to global. This application, referred to as change detection, is the main focus of this work. In some cases, a continuous collection of time series data is required, for example in frequently cloudy areas. For this reason, this work aimed at improving performance of existing change detection methods utilizing data acquired by active radar sensors in urban scenarios or areas with man-made objects present. The change detection methods described here are suitable for human activity monitoring and urban studies.

1.2 Image Change Detection

Image change detection (CD) is defined as an enhancement technique comparing two or more images of the same geographical area acquired at different times [2]. The methods compare a so-called test image with a reference image to produce a change map with information on objects that underwent change [3].

Many approaches have been proposed for the analysis of images acquired by passive sensors [4-8]. Analysis of different change detection methods applied to agricultural surveys and land-cover change studies has been reported in [8, 9]. Work reported in [10] has focused on the detection of oil-spill in marine environments, while detection of changes in forested areas was studied in [11, 12].

Despite the complexity of data processing and the large number of error sources [13-16], Synthetic Aperture Radar (SAR) sensors have also proved particularly useful in addressing change detection applications related to urban studies [17-20], human activity monitoring [21], risk management [4, 6], environmental observations [2], and forest studies [22].

Fig. 1.1 illustrates a simplified scheme of a typical change detector, where noise is assumed to be the only source of error. First, a dissimilarity function is applied to a reference and test image [23]. The corresponding output is denoised to mitigate errors caused by speckle [24, 25].

A change map is derived after thresholding or classifying the restored image [3]. Image restoration techniques, such as denoising [26] have a smoothing effect and eliminate some informative components of the SAR image content [13]. For change detection purposes, an intensive noise suppression reduces the detection rate of changes caused by the high-frequency components of the objects, but reduces the false alarm rate in unchanged relatively homogeneous areas [13]. Due to this contrasting property, the design of most change detectors has traditionally focused on reducing errors caused by noise [27].

In SAR-CD, one can distinguish between coherent and incoherent methods [27-29]. Coherent change detection exploits both the amplitude and phase of the images and has the potential to detect subtle changes. It is mainly based on the correlation coefficient, assumed to consist of two main contributions [30]: 1) temporal decorrelation, relating to changes between the reference and a test data acquisition, and 2) spatial decorrelation, caused by differences between the acquisition geometries. Methods based on the correlation coefficient have been reported in [2, 27, 30, 31], showing the performance of the sampled coherence when applied to natural hazards damage assessment and human activity surveys. If the SAR reflectivity of the image pair is similar, then coherent SAR-CD based on the maximum likelihood estimate of the refined sampled coherence performs better than that based on the correlation coefficient [29, 32, 33]. Alternatively, Principal Component Analysis (PCA) of the complex-valued image pair has been utilized in [14]. Although coherent change detection has been proved to be more robust against errors caused by noise [2], it requires short-term scenarios and data sets recorded with very similar flight paths, so the coherence is still a useful metric to evaluate changes [29].

Input	**Dissimilarity function**	**Image restoration**	**Thresholding or classification**
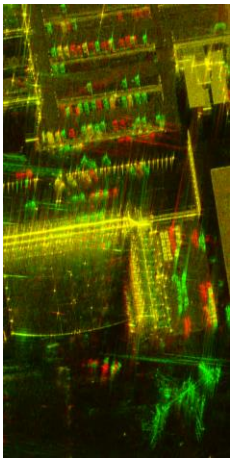	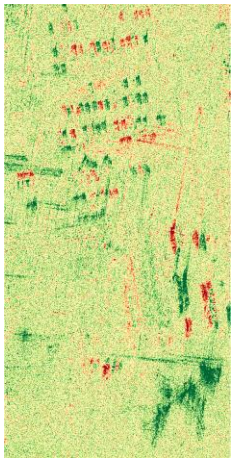	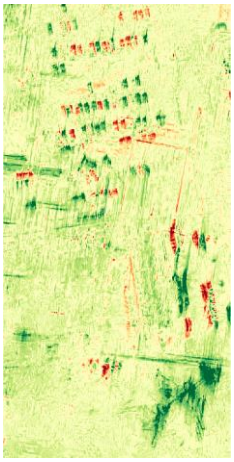	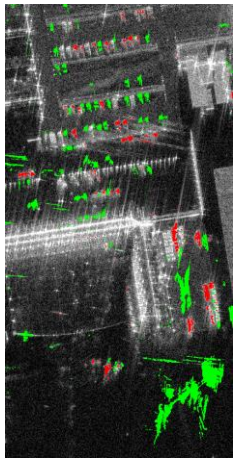
RG(B=0) composite: R=reference image G=test image	Difference Image (DI)	Restored (DI)	Overlaid change map

Fig. 1.1 General architecture of a SAR change detector.

Incoherent change detectors are more suitable when the interferometric phase of the image pair does not carry information due to spatial and temporal decorrelation. Temporal decorrelation occurs due to a physical change of the propagation path of the electromagnetic waves; i.e. it relates to different atmospheric conditions. Spatial decorrelation occurs when the image pair is not acquired with identical flight paths. In airborne SAR, inaccuracies in the navigation information and the effect of the wind and turbulence often cause significant flight track offsets. For incoherent SAR-CD, subtraction is one of the most common operators [3, 13, 17, 34]. The resulting Difference Image (DI), computed by subtracting the amplitudes of the log-transformed

images, is sensitive to noise, and performs poorly when detecting changes in distributed targets, such as trees or meadows [23]. Nonetheless, by using the DI, changes are detected in the resolution space of the input SAR images. In addition, in the log transform domain, the nature of the noise is assumed to be Gaussian and additive [26]. This property provides mathematical consistency with current available denoising and classification methods, which assume inputs disturbed with this type of noise [26, 35-37]. In SAR-CD, the DI is also referred to as the Log-Ratio Image (LRI) [34].

Methods based on statistical analysis of the SAR images are also important in incoherent change detection [38-40]. The approach described in [41] utilizes the Kullback Leibler Divergence (KLD) operator to measure the differences between two probability distribution functions. The method was validated to detect changes caused by flooding. Focusing on an urban scenario, the method in [17] investigates different probability distribution functions to model the change and no-change classes.

During the last decade, wavelets have been widely used to perform incoherent change detection [13, 42-45]. In [24] a directive complex wavelet transform was employed to denoise the input SAR images. In [45] and [46] wavelets were exploited as a fusion framework of the low and high frequency components of the mean-ratio and LRI images. In those studies, the performance of the methods was evaluated in the context of agricultural surveying and flood damage assessment. A method focusing on analysis of a wavelet-based multiresolution sequence of the LRI was proposed in [13]. Changes were detected at different resolution scales depending on their level of detail and noise level at the resolution scale. A combination of the wavelet domain and statistical algorithms was reported in [44] and [39] applied to damage assessment of flooding and volcanic eruptions respectively. To mitigate errors caused by noise, the approaches utilized a multiresolution sequence framework based on the KLD operator.

In addition to the wavelet domain, the suitability of other transforms, such as curvelets and surfacelets, were examined in [47]. In [36], a curvelet-based approach was proposed to detect changes in urban environments, to highlight the structures of man-made objects. A similar idea was proposed in [46] using the contourlet transform. Work in [48] and [49] was based on an enhancement technique of the curvelet coefficients of the power of the scattering mechanisms to highlight changes related to man-made objects.

Leaving the single-channel scenario, polarimetric data offers a good solution to alleviate errors caused by noise, yielding improved results compared to single channel SAR imagery [50-52]. The approach in [53], introduced the log-likelihood test, assuming that the coherence matrices follow a complex Wishart distribution, showing a good detection performance in forested areas. The work presented in [54] showed a comparison of diverse statistical- and non-statistical-based approaches to extract changes from polarimetric data sets using simulated scenarios. The method described in [55] exploited the coherence in combination with a log-likelihood test utilizing polarimetric and interferometric SAR data (PolInSAR) to detect changes caused by vehicles and foot tracks. In addition to statistical approaches, other dissimilarity functions suitable for polarimetric data sets were summarized in [56], where a comparison of their performances was provided.

Apart from errors caused by noise, there exist other sources of error in SAR-CD [14], for example: 1) registration noise due to geometrical distortions and differences between the acquisition geometries [57, 58], 2) amplitude and phase signal distortions caused by the radar equipment and antenna gain patterns resulting in different radiometric properties and Point Spread Functions (PSFs), 3) activation or deactivation of different point spread functions due to different illumination conditions, and 4) differences in the atmospheric conditions causing unknown phase changes in the received signals.

In SAR-CD, the extent of most error sources hinges upon the accuracy and consistency of the focusing algorithm in use. The main reason is that the characteristics of the resulting images

play a major role in change detection. A SAR image can be characterized with three parameters [59-61]: 1) the spatial resolution, 2) the Signal to Noise Ratio (SNR), and 3) the strength of artifacts, measured using the Peak to SideLobe Ratio (PLSR) or Integrated SideLobe Ratio (ISLR). The SNR relates to the detectability of an object [29, 62]. The spatial resolution of a SAR image relates to the level of detail of the objects, being a key parameter in target recognition [29]. Artifacts relate to information loss [62, 63], restricting target detection and recognition. In SAR-CD, the detection and recognition of the changes depends on the SNR and resolution of the targets involved, and image artifacts cause false alarms and misdetections. For this reason, in this work the processing chain of the SAR data cooperates in the change detection procedure by providing additional information on the targets or image artifacts.

1.3 SAR image processing: pulse compression and processing modes

For pulse sensors, SAR image focusing is achieved by means of pulse compression techniques [64, 65], performed by filtering the received signals to increase spatial resolution and SNR. A range profile is obtained after applying pulse compression to the signals recorded in the range dimension. A 2-D image is focused after applying pulse compression to the signals in range and azimuth. By extension, a 3-D image is obtained after applying pulse compression to the signals in the range, azimuth and normal dimensions. Fig. 1.2 shows on the left the imaging geometry of an airborne SAR. A repeat-pass multibaseline interferometric configuration, also referred to as tomographic [66], is depicted on the right. The figure illustrates the three operational dimensions of a SAR sensor (range, azimuth and normal) moving along a linear flight path imaging in a stripmap mode. The spatial resolutions in range, azimuth and normal dimensions are denoted here with δr, δa and δn respectively.

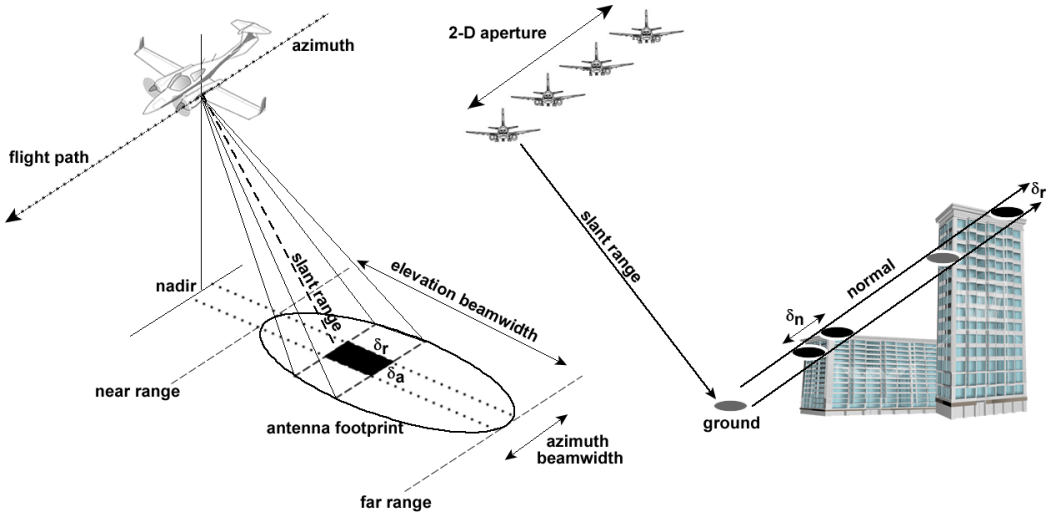

Fig. 1.2 SAR imaging geometry. (Left) Side-looking geometry of a single flight track. (Right) Repeat-pass tomographic configuration with a two-dimensional synthetic aperture.

Table 1.1 summarizes the properties of the pulse compression methods studied within this work. The methods can be divided into deterministic; i.e. the filter does not depend on the samples of the received signals, or adaptive; i.e. the filter is adapted to each individual input sample. Deterministic solutions, like the Matched Filter (MF), provide images with a high SNR and spatial resolution but introduce sidelobes that can mask nearby targets. The MF is the most common pulse compression method in SAR image processing. In contrast, adaptive processing is not common in the SAR image formation chain. However, these methods are relevant in this work because they can potentially provide images with better characteristics, such as resolution, SNR or lower sidelobes, than those focused with deterministic approaches. Deterministic and adaptive filters can be modified with weighting functions. Real-valued weightings, referred to

as windows or tappers [67], are typical solutions to reduce sidelobes at the cost of degrading resolution and SNR. Complex-valued weightings, referred to as mismatched filters [68, 69], can provide images with reduced sidelobes while preserving resolution and SNR.

TABLE 1.1
PULSE COMPRESSION METHODS

Input	**Pulse Compression**		**Output characteristics**		
Radar signals	**Type**	**Signal weighting**	**SNR**	**Resolution**	**Artifacts**
Slant range	Deterministic or adaptive	Real- or complex-valued	Sr	δ_r	ISLRr
Azimuth	Deterministic	Real-valued	Sa	δ_a	ISLRa
Normal	Adaptive	Real-valued	Sn	δ_n	ISLRn

Table 1.1 lists the nomenclature of the SNR, spatial resolution and strength of artifacts of the signals compressed in each individual dimension (range, azimuth and normal). The characteristics of a SAR image depend on the performance of the pulse compression methods applied to the signals recorded from all dimensions involved in the data acquisition. Table 1.2 presents the characteristics of a 2-D and a 3-D SAR image based on the nomenclature in Table 1.1. The SNR of a 2-D image is the result of applying pulse compression in the azimuth dimension to the range compressed signals with initial SNR equal to Sr. In Table 1.2 the symbol (*) indicates that the SNR of a 2-D image depends on a 2-D convolution. In the 2-D spatial domain, the resolution cell size is given by the product of the spatial resolution in range and azimuth, and the quantity and strength of artifacts accumulate with each additional dimension.

Since the accuracy of a change detector is constrained by the image formation method, it is important to first study the different pulse compression schemes based on the characteristics listed in Table 1.1. The performance of adaptive processing methods applied to SAR image formation is covered in the first research topic addressed in this thesis (chapter 2).

TABLE 1.2
2-D AND 3-D SAR IMAGE CHARACTERISTICS

Spatial domain	**SNR**	**Resolution**	**Artifacts**
2-D	Sr*Sa	$\delta_r \times \delta_a$	≈ (ISLRr+ISLRa)
3-D	Sr*Sa*Sn	$\delta_r \times \delta_a \times \delta_n$	≈ (ISLRr+ISLRa+ISLRn)

Diverse processing modes result when applying pulse compression combined with weightings to the signals recorded in the different dimensions. An *n*-dimensional single-look processing is performed by applying pulse compression with *n* weightings, one for each dimension. Single-look processing yields a single image with the highest attainable resolution and SNR. Multilook processing in range performs pulse compression with a set of weightings designed to filter different spectral components of the signals. This mode produces a set of images, referred to as looks, with the radar backscatter at slightly different frequencies. Sub-aperture processing in azimuth performs pulse compression with weightings preserving a reduced number of the received pulses, providing a set of images with the temporal response of the targets (static or moving object). Multisquint processing in azimuth performs pulse compression with weightings preserving only the samples of the signals acquired from a specific azimuth direction. It produces a set of images, referred to as squints, with the spatial behaviour of the targets (isotropic or anisotropic). Fig. 1.3 illustrates a set of SAR images focused with different pulse compression methods and processing modes. Fig. 1.3 (a) shows a single-look SAR image acquired over the *Allgäu* airport in *Memmingen* (Germany). Fig. 1.3 (b) depicts an RGB composite from three looks focused at different carrier frequencies: one can observe the frequency dependence of the range sidelobes. Fig. 1.3 (c) shows an RGB composite from three squints, highlighting diverse

image artifacts in colour. An RG(B=0) composite showing the sidelobe reduction efficiency of adaptive processing is depicted in Fig. 1.3 (d).

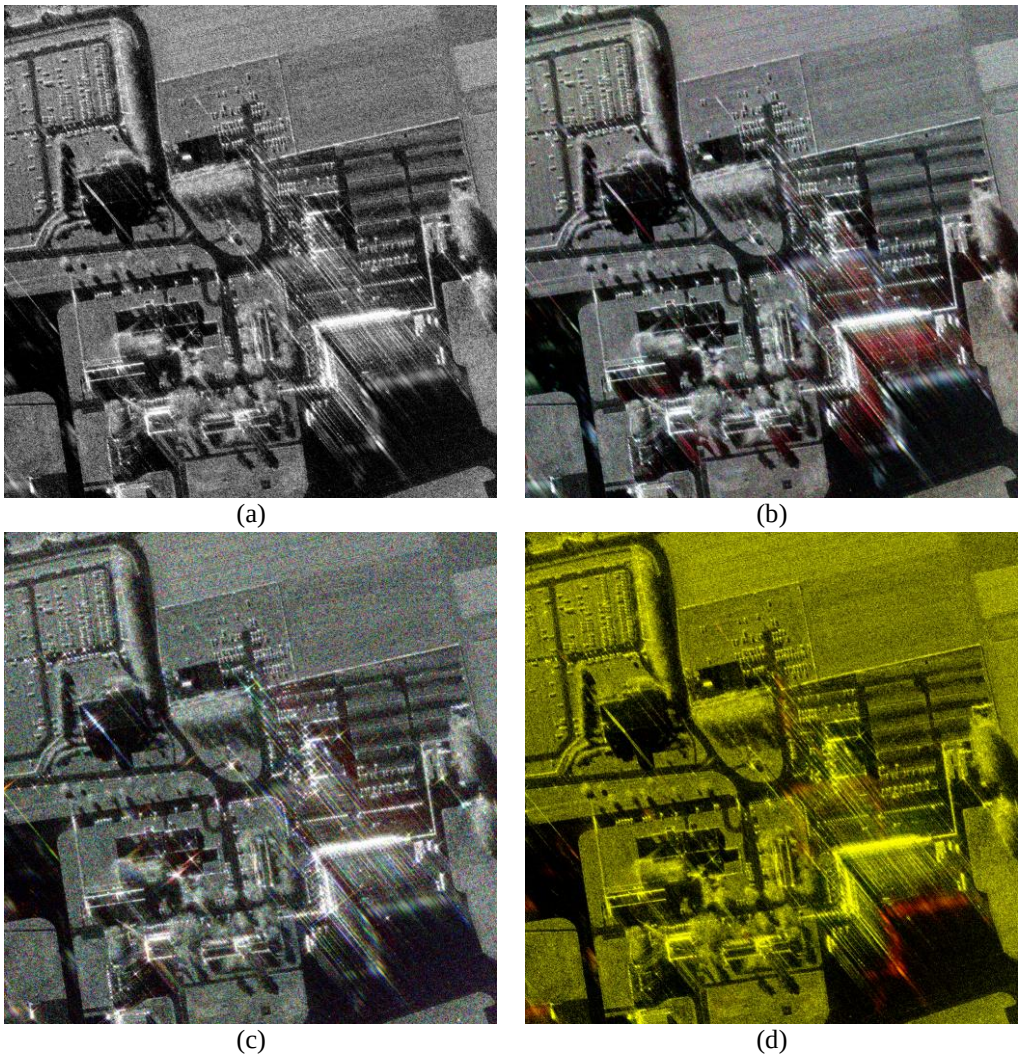

Fig. 1.3 SAR images processed with different pulse compression schemes. (a) Single-look image focused by applying a matched filter in range and azimuth. (b) RGB composite: R= look at a carrier frequency of 34.65 GHz, G= look at a carrier frequency of 34.95 GHz, and B= look at a carrier frequency of 35.25 GHz. (c) RGB composite: R= squinted sub-aperture focused with the signals acquired with an azimuth angle of arrival in the interval [-3°, -1.25°], G= squinted sub-aperture focused with the signals acquired with an azimuth angle of arrival in the interval [-1.25°, 1.25°], and B= squinted sub-aperture focused with the signals acquired with an azimuth angle of arrival in the interval [1.25°, 3°]. (d) RG(B=0) composite: R= single-look image focused by applying the matched filter in range and azimuth, and G= single-look image focused by applying adaptive processing in range and the matched filter in azimuth.

Current change detectors do not consider the presence of image artifacts or targets whose position or image sharpness varies during the illumination time. Moving objects like cars, trains, and trees fall inside this category. Oriented flat surfaces, such as roofs, can return a strong backscattering component within some sub-apertures. This effect manifests itself as azimuth glint [63]. These objects are a frequent source of error in SAR-CD, particularly in urban scenarios. Single look and multi-look processing are the most utilized processing modes for SAR-CD purposes. However, none of these modes allow early detection of moving targets or image artifacts. This motivates research into adapting current methods to account for additional infor-

mation collected from other processing modes to reduce errors caused by undesired objects. The design of a change detector, working at nominal resolution and exploiting spatial information to remove errors caused by artifacts is addressed in second place (chapter 3). With the aim of complementing the two previous research topics, the performance of the designed change detector is compared and evaluated when exploiting adaptive processing for SAR image formation (chapter 4).

A 3-D SAR image is focused after applying pulse compression in the normal dimension using the data acquired from a tomographic configuration. This processing step disambiguates layover and permits the detection of multiple scatterers within a resolution cell; i.e. super-resolution. In addition, it provides volumetric information of the targets in the scene. In this manner, tomographic SAR broadens the scope of change detection applications, particularly for urban studies, and forest monitoring. 3-D change detection is more robust against differences in illumination, and provides new levels of detail in comparison to traditional 2-D change detection. However, existing methods do not consider the specifics of the SAR data such as its associated error sources (amplitude and phase noise), nor the information retrieved (backscatter and height estimates). By extension, they neither take advantage of the characteristics of SAR image formation. This leads to the fourth research topic of this thesis, which focused on the design of a change detection method accounting for the specifics of SAR tomography and taking advantage of the pulse compression method applied in the normal dimension (chapter 5).

1.4 SAR image post-processing: denoising and classification

Incoherent addition of a set of looks focused via multilook processing yields an image with reduced noise in comparison to the corresponding single-look. In this manner, SAR-CD takes advantage of multilook processing for reducing errors caused by noise. In coherent change detection, denoising by means of multilook processing is a common practice. However, advanced image restoration methods are required to exploit the spatial resolution and SNR of the images focused via single-look processing. To some degree, this situation can also be extended when performing thresholding or classification in the last stages of the change detector. The image post-processing techniques embedded in the change detection methods utilized in this thesis are described in the following.

1.4.1 Image restoration with morphological diversity

A signal, considered as an N-length vector in a finite-dimensional subspace of $\mathbb{R}^N$, is strictly sparse if most of its entries are equal to zero; i.e. if its support is of cardinality $k \ll N$. A k-sparse signal is a signal for which exactly k samples have a non-zero value. In compressed sensing [26], if a signal is not sparse, it can be sparsified in an appropriate domain; e.g. a sine waveform is not sparse in its original domain, the time domain, but its Fourier domain representation is extremely sparse. The atoms of the Fourier dictionary are sine and cosines waves of infinite length. For image analysis, however, the Fourier domain introduces two main drawbacks: 1) its atoms have infinite support in the time domain, thus it is not possible to represent realistic signals, which have a finite support, and 2) sine shapes are rare features in natural scenes acquired from remote sensing systems.

Wavelets appeared to overcome the limitations of the Fourier domain. They are defined as a time-frequency analysis tool with atoms of finite length. In image processing, wavelets behave as band-pass filters. They *sparsify* data content, and are utilized in many applications, such as data compression, image analysis and restoration, deconvolution and inpainting (reconstruction of deteriorated parts of an image) [26, 70].

Curvelets are more recent transforms outperforming the sparsifying capability of wavelets at the edges of highly heterogeneous objects [26, 70-73]. They introduce directivity as a novel pa-

rameter in the time-frequency analysis. For this reason, they are a suitable tool to analyze objects with multiple edges and high-frequency components.

For image analysis and restoration purposes, wavelets are well-adapted for detection of isotropic features or uniform areas but fail to represent other types of image content such as lines or edges, where curvelets outperform wavelets. This sparsification failure introduces artifacts [26]. One can exploit multiple transforms that can compactly represent different image objects when used in combination. From the principle of the *morphological diversity* theory, a better denoised image can be obtained by taking advantage of the different domains, each sparsifying different image features. This decomposition problem can be solved using two approaches [26]: Basis Pursuit (BP) and Morphological Components Analysis (MCA). In this work, the Mean of Maximum (MOM) variant of the MCA method reported in [74] is utilized for image decomposition and denoising. Fig. 1.4 illustrates the performance of MCA-MOM using wavelets and curvelets. One can observe that the linear structures are attached to the curvelet component, while the homogenous areas are described by the wavelet component. The sum of the two components yields a denoised version of the original SAR image.

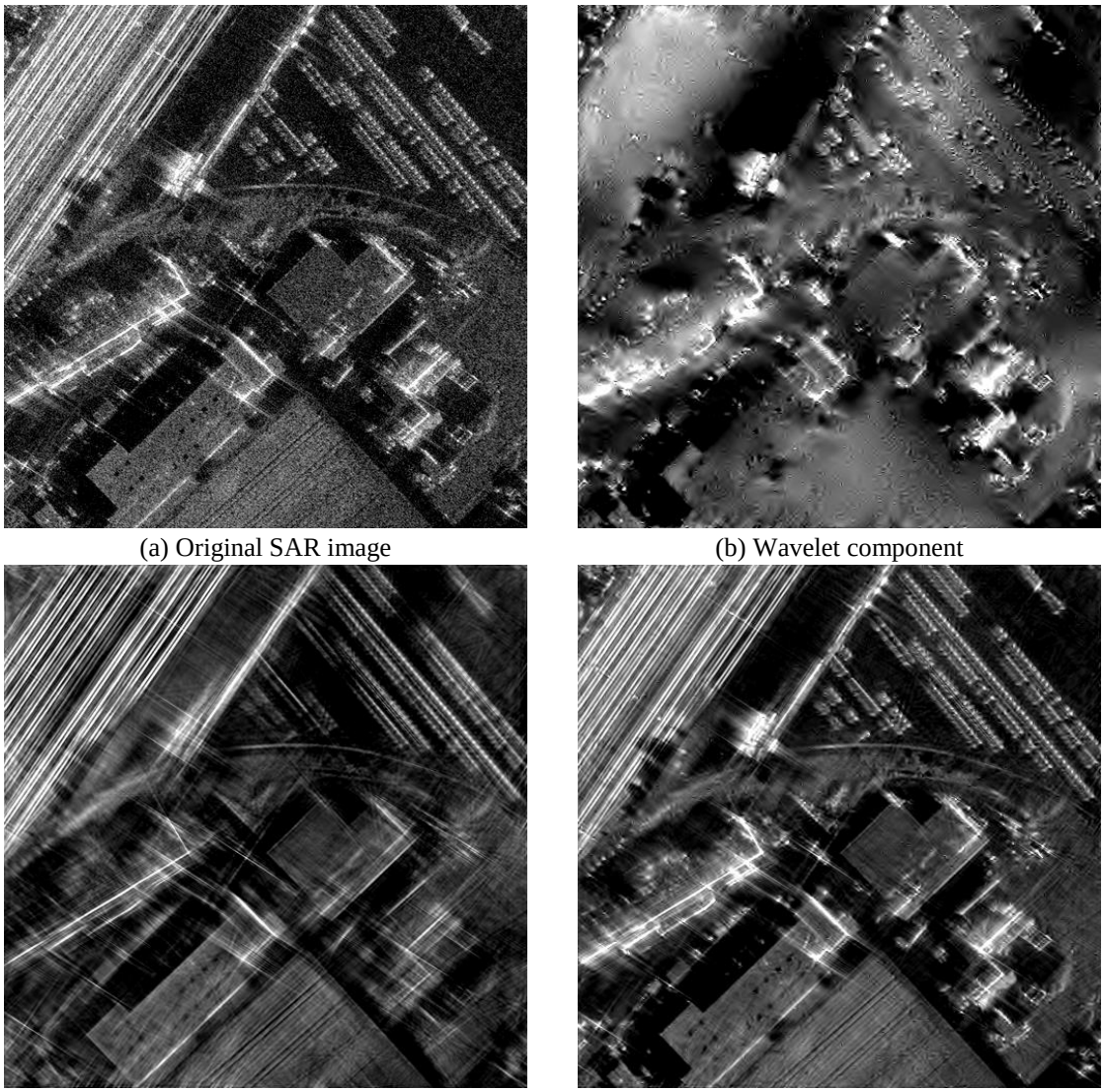

(a) Original SAR image

(b) Wavelet component

(c) Curvelet component

(d) Sum of the wavelet and curvelet components: denoised version of (a)

Fig. 1.4 Wavelet- and curvelet-based SAR image decomposition and restoration via MCA-MOM.

1.4.2 Image classification: Expectation Maximization (EM), Markov (MRF) and Conditional Random Fields (CRF)

Diverse methods have been proposed to perform thresholding or classification for SAR-CD purposes [3, 75, 76]. For mathematical simplicity, it is assumed that the change and unchanged classes follow a Gaussian distribution, leading to the so-called Gaussian mixture problem [3]; i.e. the methods assume that the probability density function of the image to be classified is modeled as a mixture density distribution consisting of as many components as classes. Solving this problem requires knowledge of the probabilities of the classes, which are unknown *a priori* unless ground truth is available. In unsupervised SAR-CD, automatic solutions are adopted. Automatic classification can be performed by means of the Expectation Maximization (EM) method. Under the hypothesis of interpixel independence and based on Bayes rule, EM assigns each pixel to the class maximizing the *a posteriori* conditional probability.

The EM method does not consider information of the pixel's neighbourhood. As a consequence, the method is sensitive to errors caused by noise. Statistical inference can be applied to refine results, using for example a Markov Random Field (MRF). A MRF assigns classes based on the probability density functions observed at each individual pixel and its spatial neighbourhood. The neighbourhood is defined using a metric, such as the Euclidean or city-block distance, and a scale parameter; i.e. the size of the neighbourhood. A MRF model consists of two terms, a so-called data term and an energy term. The former depends on the assumed probability density functions. The latter is user-defined, and is used to weight the potential class of a pixel given the classes of its neighbours. This weighting is typically performed by means of a so-called shape parameter. The shape parameter behaves as a smoothing factor in typical morphological filters. The MRF model can be extended by adding additional user-defined terms constraining the probabilities of certain classes. In those cases, the resulting MRF model is referred to as a Conditional Random Field (CRF).

1.5 Objective and research questions

Focusing on reducing errors caused by noise has led to a large number of change detectors that consider SAR images as noise-corrupted versions of those that could be recorded by other active or passive sensors neglecting SAR specific properties. This thesis focuses on taking advantage of the images focused with different pulse compression methods, described in section 1.3, to improve the performance of existing change detectors. In this manner, the processing chain collaborates in the detection of changes of interest or removal of false alarms to improve overall performance. The thesis aims to answer the following research questions.

Pulse compression in range

Current SAR sensors transmit linear frequency modulated (LFM) signals. Pulse compression of LFM signals by means of the matched filter method yields range profiles of high spatial resolution and SNR but increase sidelobes levels. The presence of image artifacts, such as sidelobes, has a negative impact in SAR-CD, increasing the false alarm and misdetection rate. The research evaluates the performance of deterministic and adaptive pulse compression methods, leading to the question:

1. For SAR image focusing, how does adaptive pulse compression perform when applied to the signals recorded in slant range in comparison to different deterministic approaches, such as the matched filter?

Pulse compression in azimuth

Similar to the range dimension, matched filtering is the most common pulse compression method applied to the signals in the azimuth dimension. Adaptive processing in azimuth can involve a very high computational complexity. Pulse compression in azimuth can be modified

by incorporating signal weightings to provide SAR images with different characteristics while not significantly increasing the computation time. The research aims at implementing a change detector taking advantage of different azimuth compression methods combined with real-valued weightings. This leads to the following research question:

2. How can SAR change detection take advantage of different pulse compression methods in azimuth, such as single-look and multisquint processing mode?

Pulse compression in range and azimuth

To broaden the scope of the two previous research questions, different pulse compression methods are combined and utilized for SAR image processing and change detection. The main goal is to evaluate the performance of adaptive processing in range for SAR-CD applications and compare the results with those obtained when using multisquint processing mode applied to the signals recorded in the azimuth dimension. The corresponding research question is:

3. How does SAR change detection benefit from combinations of different range and azimuth pulse compression methods?

Pulse compression in normal

SAR offers three dimensional imaging when multibaseline interferometric configurations are employed. A 3-D image is obtained after applying pulse compression to the signals recorded in the normal dimension. Since the signals in the normal dimension are typically sparse due to a usually very limited number of baselines, adaptive processing is applied to mitigate sidelobes and achieve super-resolution. The research focuses on evaluating and implementing a change detection method taking advantage of pulse compression in the normal dimension, leading to the following research question:

4. What are the implications of three dimensional SAR image focusing for change detection applications?

1.6 Structure of the dissertation

Chapter 1 familiarizes the reader with concepts and terminology utilized along this thesis. It compiles the state of the art in SAR image change detection, and describes the characteristics of SAR imagery and the different pulse compression techniques. It also covers a brief description of the image restoration and classification methods utilized in this work. The research questions studied in this thesis are presented at the end.

Chapter 2 is based on a first author, peer-reviewed article: E. M. Domínguez, C. Magnard, M. Frioud, D. Small, and E. Meier, "Adaptive Pulse Compression for Range Focusing in SAR Imagery," IEEE Transactions on Geoscience and Remote Sensing, vol. 55, no. 4, pp. 2262-2275, 2017. The work is related to research questions 1 and 3, and evaluates the performance of adaptive processing for SAR image formation purposes. The publication is self-contained in terms of structure and content.

Chapter 3 is based on a first author, peer-reviewed article: E. M. Domínguez, E. Meier, D. Small, M. E. Schaepman, L. Bruzzone, and D. Henke, "A Multisquint Framework for Change Detection in High-Resolution Multitemporal SAR Images," IEEE Transactions on Geoscience and Remote Sensing, vol. 56, no. 6, pp. 3611 - 3623, 2018. It is related to research questions 2 and 3. The work describes the proposed change detection method exploiting multisquint processing mode to reduce errors caused by image artifacts. The publication is self-contained in terms of structure and content.

Chapter 4 is based on a first author, peer-reviewed conference article: E. M. Dominguez, M. Frioud, D. Small, and D. Henke, "Range Adaptive Processing and Multisquint Processing Mode for SAR Image Change Detection," in 12th European Conference on Synthetic Aperture Radar

(EUSAR), Aachen, Germany, 2018, pp. 1-6: VDE. It is related to research question 3. The work demonstrates that adaptive processing and multisquint processing mode can improve the performance of traditional SAR change detection methods by reducing errors caused by image artifacts. The publication is self-contained in terms of structure and content.

Chapter 5 is based on a first author, peer-reviewed article: E. M. Domínguez, C. Magnard, E. Meier, D. Small, M. E. Schaepman, and D. Henke, "A Back-Projection Tomographic Framework for VHR SAR Image Change Detection," IEEE Transactions on Geoscience and Remote Sensing, 2018 (in revision). It includes the design of a change detection method taking advantage of SAR tomography to improve performance of methods based on 2-D images.

Chapter 6 collects the main findings from chapters 2 to 5 to address the research questions formulated in chapter 1. It closes with a set of conclusions and an outlook to future research directions.

2 ADAPTIVE PULSE COMPRESSION FOR RANGE FOCUSING IN SAR IMAGERY

This chapter has been published as: E. M. Domínguez, C. Magnard, M. Frioud, D. Small, and E. Meier, "Adaptive Pulse Compression for Range Focusing in SAR Imagery," *IEEE Transactions on Geoscience and Remote Sensing*, vol. 55, no. 4, pp. 2262-2275, 2017.

E.M.D., C.M., and E.M. designed the research. E.M.D. and C.M. processed the data and performed the analysis with advice of E.M. and M.F. E.M.D. wrote the manuscript and all coauthors reviewed and edited the manuscript.

Abstract

Synthetic Aperture Radar (SAR) images are focused via range and azimuth compression. Typically, a matched filter is used for range compression. However, its inherent operation introduces target masking due to sidelobes, reducing the recognition and interpretability of the underlying targets. To optimize the focusing quality, Adaptive Pulse Compression (APC) can be applied. In this work, APC is assessed for range processing in SAR image focusing. The performance of the method is evaluated with airborne SAR imagery and compared to traditional schemes. We show that by applying APC under single channel, interferometric and stepped frequency scenarios, the quality of the SAR images, the corresponding phase maps and interferometric coherence images can be significantly improved, and that APC provides both better amplitude and phase estimates of the range profiles. APC is shown to preserve the characteristics of the azimuth signals, and can be applied without restricting the azimuth compression scheme.

2.1 Introduction

Synthetic aperture radar can acquire images almost independent of weather and daylight conditions. The focusing quality of the images and to some extent the interpretability and recognition of the underlying targets depend on the accuracy of the reconstruction algorithms in use.

In general, SAR image formation is carried out using pulse compression techniques such as the well-known Matched Filter (MF) method. MF preserves Signal to Noise Ratio (SNR) for a solitary point target embedded in additive white Gaussian noise [64]. It has low computational complexity, but multiple drawbacks [64]: a) SAR data is characterized by range/azimuth profiles containing many point-like and distributed targets, thus the SNR of an individual target is reduced in comparison with a similar isolated target, b) it introduces sidelobes that can mask nearby targets and c) it is not robust against Radio Frequency Interference (RFI). To suppress sidelobes, some deterministic alternatives were proposed, divided into processing and post-processing techniques. The former prevent the presence of artifacts before image formation, whereas the latter reduce sidelobes after image focusing. Windowing [67] or Mismatched Filters (MMF) [69, 77, 78] are traditional processing techniques capable of reducing sidelobes without excessive computation requirements. These methods trade off resolution, sidelobe levels and SNR [64].

The post-processing techniques perform sidelobe reduction in the image domain. A popular approach, Spatially Variant Apodization (SVA), was reported in [79]. SVA preserves SNR and resolution and in combination with bandwidth extrapolation achieves super-resolution [80]. However, it introduces major disadvantages: a) it is required that the SAR images are acquired with small squint angles so that slant range and azimuth are nearly perpendicular [81], b) time domain azimuth compression methods, such as Fast Factorized Back-Projection [82], Back-Projection [65] and Correlation [83] cannot benefit from this technique, since the spectra of geocoded images do not relate to the spectra of the SAR data, and c) if time domain azimuth compression methods are not supported, SAR images acquired with non-linear trajectories cannot benefit from SVA [84].

Sidelobe reduction can also be performed with spectral estimation methods. Work reported in [85] exploits Capon's Minimum Variance Method (MVM) [86] and the Amplitude and Phase Estimation (APES) technique [87]. These methods preserve SNR and resolution, and can achieve super-resolution by applying diagonal loading and image resampling. These techniques introduce again multiple disadvantages: a) the estimation of the covariance matrices is computed with overlapping image chips (multi-looked), so the overlapping factor becomes a critical parameter to guarantee matrix inversion, and b) only frequency domain azimuth compression methods are supported. Similarly, the work described in [88], and referred to as High Definition Vector Imaging (HDVI), introduces the same advantages and disadvantages. Currently, MVM is used to super-resolve the third dimension in tomographic SAR [89, 90].

To preserve resolution and SNR while reducing sidelobes, APC [91] is applied to range focusing during SAR image formation. In contrast to the methods described in [85] and [88], APC exploits full rank covariance matrices computed with all available and different information possible, offering flexibility via an initialization stage, where the output of a spectral estimation can also be improved. APC is a processing technique and thus not limited to frequency domain azimuth compression methods, as we will demonstrate in this study. It can provide super-resolution [92], and compensate Doppler mismatched losses for moving targets [93]. Additionally, computation requirements can be alleviated by reducing dimensionality of the covariance matrices, referred to as Fast Adaptive Pulse Compression (FAPC) [94].

In recent literature, APC- and FAPC-based methods have not been applied to SAR image processing. In contrast to work reported in [91], SAR range profiles contain complex-valued radar returns from many point-like and distributed targets. Inherent range-azimuth coupling

constrains the range compression: characteristics of the azimuth signals (resolution, sidelobes levels) must be preserved without introducing artifacts. In this work, we evaluated the performance of range adaptive processing methods for SAR image focusing. For single channel SAR imagery, the analysis was carried out in terms of resolution, SNR, and achieved sidelobe levels. Additionally, interferometric and stepped-frequency data sets were used to investigate whether APC respects SAR range-azimuth coupling, and is capable of providing better amplitude estimates and phase estimates over the range profiles. The SAR images obtained with APC were compared with those focused using traditional methods such as matched filter, mismatched filters, and windowing.

The paper is organized as follows: Section 2.2 describes the sensor, data and test site. Section 2.3 elaborates the procedure to focus single channel and multichannel SAR imagery, also with frequency agility. Section 2.4 illustrates results obtained with SAR data, using single and multichannel data sets. Section 2.5 includes a discussion of the results, and Section 2.6 draws conclusions gathered throughout this study. A list of acronyms and simulation results of the signature of a corner reflector are provided in the Appendix.

2.2 Sensor, Data and Test Site

The data sets were acquired in 2013 with Fraunhofer FHR's MEMPHIS sensor [95] over the Allgäu airport in Memmingen, Germany, (N47.98°, E10.23°). MEMPHIS transmits 0.4 μs chirps each with a bandwidth and sampling frequency of 200 MHz. The SAR images used in this document were recorded in linear stripmap configuration at Ka-band using stepped-frequency chirps. MEMPHIS was equipped with four receiving antennas arranged vertically to enable multibaseline cross-track interferometry and TomoSAR [96]. In each channel, the sensor transmitted eight LFM signals of 200 MHz each. The bandwidth overlap between consecutive chirps was 100 MHz. After bandwidth synthesis, a LFM signal of 900 MHz bandwidth was obtained, improving the range resolution from 0.75 m to 0.167 m.

2.3 Method

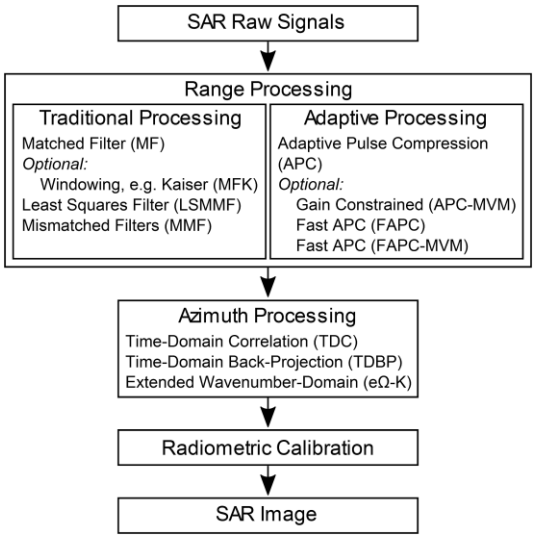

Fig. 2.1 Overview of the image processing chain for single channel SAR data sets. The algorithms used in this study are included in the corresponding boxes.

For pulsed sensors, SAR image focusing is performed by applying pulse compression to each dimension sequentially, range and azimuth (see Fig. 2.1). These two steps are required in-

dependent of the characteristics of the data sets. In the first subsection we describe diverse range compression schemes to focus single channel SAR data, with special emphasis on range adaptive processing. Fig. 2.1 shows the methods used in this document, distinguishing between traditional and adaptive methods for range processing. In the corresponding subsections, additional steps for image focusing of stepped-frequency and interferometric data sets are also included.

2.3.1 Single channel SAR image focusing

Using the MF method, the range profile estimate is obtained after convolving a received pulse with a complex conjugate time reversed-copy of the transmitted waveform (replica). The estimate of the r-th delay sample of a L-length range profile is expressed as [64, 91]:

$$x_{MF}(r) = \boldsymbol{s}^H \boldsymbol{y}(r) \tag{2.1}$$

where $\boldsymbol{s}_{N\times 1} = [s_0\ s_1\ \cdots s_{N-1}]$ is the N-length transmitted waveform, $\boldsymbol{y}(r)_{N\times 1} = [y(r)\ y(r+1)\cdots\ y(r+N-1)]$ is a vector of N contiguous samples of the complex received pulse, and $(\cdots)^H$ is the Hermitian operation. Each complex-valued sample of a received pulse is given by:

$$y(r) = \boldsymbol{x}^T(r)\boldsymbol{s} + v(r) \tag{2.2}$$

where $\boldsymbol{x}(r)_{N\times 1} = [x(r)\ x(r-1)\cdots\ x(r-N+1)]$ are N contiguous samples of the range profile impulse response (backscatter coefficient), $(\cdots)^T$ is the transpose, and $v(r)$ is assumed to be additive white Gaussian noise. Inserting (2.2) into (2.1) and rearranging terms, yields the well-known model of the MF in the time domain:

$$x_{MF}(r) = \boldsymbol{s}^H \boldsymbol{A}^T(r)\boldsymbol{s} + \boldsymbol{s}^H \boldsymbol{v}(r) \tag{2.3}$$

where $\boldsymbol{v}(r)_{N\times 1} = [v(r)\ v(r+1)\cdots\ v(r+N-1)]$ and

$$\boldsymbol{A}(r)_{N\times N} = \begin{bmatrix} x(r) & x(r+1) & \cdots & x(r+N-1) \\ x(r-1) & x(r) & \ddots & \vdots \\ \cdots & \ddots & \ddots & x(r+1) \\ x(r-N+1) & \cdots & x(r-1) & x(r) \end{bmatrix} \tag{2.4}$$

is a collection of N length-N sample-shift snapshots (in the columns) of the impulse response. As described in [91], if $x(r)$ is considered to be a solitary point target; i.e. the off-diagonal elements of the matrix $\boldsymbol{A}(r)$ are negligible, then $x_{MF}(r) = \boldsymbol{s}^H\boldsymbol{x}(r)\boldsymbol{s} + \boldsymbol{s}^H\boldsymbol{v}(r)$, and thus the detection of the target depends exclusively on the SNR. However, if the off-diagonal elements are large relative to $x(r)$, the MF masks its theoretical backscatter independently of its SNR.

Windowing or mismatched filters are simple solutions to alleviate target masking and reduce sidelobes [64, 67, 69, 77, 78]; however, at the cost of SNR loss and resolution degradation. In contrast to windowing, mismatched filters are complex-valued and their design is based on the transmitted waveform $\boldsymbol{s}$. In this study, we consider two mismatched filters. The first, referred to as simply MMF, is derived from work reported in [69]. In this work, the $(2N-1)\times(2N-1)$ weighting matrix was first initialized as the identity matrix. The central diagonal element(s) corresponding to the 3 dB main peak response of the ambiguity function of the transmitted signal $\boldsymbol{s}$ were then replaced by zeros. The second approach is the well-known Least Squares Mismatched Filter (LSMMF) described in [91].

A more effective solution is obtained by designing a complex-valued filter $\boldsymbol{w}_{N\times 1}$ adapted to each individual range bin [91]. Recovering the received signal from the model of the MF in (2.3), yields:

$$\boldsymbol{y}(r) = \boldsymbol{A}^T(r)\boldsymbol{s} + \boldsymbol{v}(r) \tag{2.5}$$

The combination of (2.1) and (2.5) permits to derive a cost function that minimizes the Mean Square Error (MMSE) of the estimate of a range bin as follows [91]:

$$J(r) = E[|x(r) - \boldsymbol{w}^H(r)\boldsymbol{y}(r)|^2] \tag{2.6}$$

being $\boldsymbol{w}$ the weighting function to be computed as a substitute of the MF; i.e. $\boldsymbol{s}^H$ in (2.1). By assuming that the impulse response $x(r)$ is stationary over N and uncorrelated with the noise, and that neighboring impulse response terms are also uncorrelated, the solution to (2.6) can be expressed as:

$$\boldsymbol{w}(r) = \rho(r)(\boldsymbol{C}(r) + \boldsymbol{R})^{-1}\boldsymbol{s} \tag{2.7}$$

where $\rho(r) = |x(r)|^2$, $\boldsymbol{R}_{N\times N}$ is the noise covariance matrix, unknown *a priori*, and $\boldsymbol{C}_{N\times N}(r)$ is the weighted covariance matrix of the transmitted waveform:

$$\boldsymbol{C}(r) = \sum_{n=-N+1}^{N-1} \rho(r+n)\,\boldsymbol{s}_n\boldsymbol{s}_n^H \tag{2.8}$$

where $\boldsymbol{s}_n$ is a *N*-length vector computed according to:

1) if $n>0$, $\boldsymbol{s}_n$ is obtained by concatenating n zeros and $[s_0\ s_1\ \cdots s_{N-n}]$,

2) if $n=0$, $\boldsymbol{s}_n = \boldsymbol{s}$, and

3) if $n<0$, $\boldsymbol{s}_n$ is computed by concatenating $[s_{|n|}\ s_{|n|-1}\ \cdots s_{N-1}]$ and n zeros.

The complex-valued vector $\boldsymbol{w}(r)$ requires a $N \times N$ matrix inversion per range bin; thus the computational complexity depends on the number of range bins per pulse and the length of the transmitted waveform $\boldsymbol{s}$. Once $\boldsymbol{w}(r)$ is obtained by solving (2.7), the range profile in the MMSE sense is estimated with:

$$x_{MMSE}(r) = \boldsymbol{w}^H\boldsymbol{y}(r) \tag{2.9}$$

As an alternative to (2.6), the MMSE cost function can be reformulated by imposing a unity gain constraint of the filter $\boldsymbol{w}$ as follows [97]:

$$\boldsymbol{w}^{\boldsymbol{H}}(r)\boldsymbol{s} = 1 \tag{2.10}$$

to yield:

$$J(r) = E[|x(r) - \boldsymbol{w}^H(r)\boldsymbol{y}(r)|^2] + Re\{\xi(\boldsymbol{w}^H(r)\boldsymbol{s} - 1)\} \tag{2.11}$$

where ξ is a Lagrange multiplier, and $Re\{\cdots\}$ is the real part of the argument. Solving (2.11) considering the linear constraint in (2.10) gives the solution of the MVM method [86, 97]:

$$\boldsymbol{w}_{MVM}(r)_{N\times 1} = \frac{\boldsymbol{C}^{-\mathbf{1}}(r)\boldsymbol{s}}{\boldsymbol{s}^H\boldsymbol{C}^{-1}(r)\boldsymbol{s}} \tag{2.12}$$

By inserting (2.12) into (2.1) one obtains a gain constrained estimate of a range bin based on the MMSE criterion, yielding:

$$x_{MMSE\_MVM}(r) = \boldsymbol{w}_{MVM}^H\boldsymbol{y}(r) \tag{2.13}$$

To compute (2.7) and (2.12), an estimation of the power of the surrounding range bins $\rho(r)$ is required. This can be obtained by applying an initialization stage, for example using the MF. With successive iterations based on the prior power estimates, a refined range profile is obtained. This iterative procedure is summarized in Table 2.1 and referred to as Adaptive Pulse Compression or Range Adaptive Processing [91, 98].

TABLE 2.1
ADAPTIVE PULSE COMPRESSION ALGORITHM

Algorithm 1 *M*-staged Iterative MMSE

Task: Adaptive Pulse Compression
Parameters: Transmitted signal $\boldsymbol{s}$, receiver signal $\boldsymbol{y}$, and number of stages *M*.
Initialization:
- k=0
- Estimate the range profile $\boldsymbol{x}_k$, i.e. using (2.1)
- Compute the power estimates $\boldsymbol{\rho} = |\boldsymbol{x}_k|^{\boldsymbol{2}}$

Main iteration:
for k=1 **to** *M*-1 **do**
- Compute $\boldsymbol{C}(r)$ with (2.8)
- Apply (2.7) or (2.12) to obtain $\boldsymbol{w}_k$
- Recover the spatial response using $\boldsymbol{x}_k = \boldsymbol{w}_k^{\boldsymbol{H}}\boldsymbol{y}$
- Compute the power estimates $\boldsymbol{\rho} = |\boldsymbol{x}_k|^{\boldsymbol{2}}$

if (*k*=*M*) **then** stop
Output: Estimate of the range profile $(\boldsymbol{x}_k)_{k=0\ldots M-1}$

Note: In (2.7), $\boldsymbol{R} = [0]_{N\times N}$, instead of $\boldsymbol{R} = \sigma_e[I]_{N\times N}$, assuming that the noise standard deviation σ_e cannot be computed.

Once the corresponding received signals are range compressed using one of the aforementioned techniques, azimuth compression and radiometric calibration are performed. In contrast to the range dimension, the azimuth samples are not aligned, and the signals are typically Linear Frequency Modulated (LFM) [65]. To reduce potential errors during azimuth compression, the Time Domain Correlation (TDC) [65, 83] was used. Radiometric calibration was performed as described in [28].

2.3.2 Single channel SAR image focusing with frequency agility

The procedure to focus SAR images acquired in stepped-frequency mode requires first synthetizing the bandwidth of the stepped LFM signals in range [99]. Two different frameworks can be used: a) synthesize the full bandwidth of the received signals and apply a range compression scheme; and b) apply a range compression method to each received pulse and synthesize the full bandwidth with the corresponding range compressed profiles. These options are schematized in Fig. 2.2 using a stepped-frequency data set with *Nsb* sub-bandwidths (for MEMPHIS, *Nsb*=8).

With APC, option a) implies an increase of dimensionality; it exploits the information provided with the entire synthesized bandwidth. For pulse radars without imaging capabilities, a) has shown better results than b) [94, 98]. However, the computational requirements increase dramatically due to the inversion of larger weighted covariance matrices. For this reason, we used the second solution, proceeding in a fashion similar to FAPC [94]. The performance of FAPC was evaluated as a side effect of applying APC separately to each sub-bandwidth of the stepped-frequency data set. The evaluation of FAPC when applied to a single sub-bandwidth was beyond the scope of this work.

The synthesis of the full bandwidth of the range profiles was performed with the method described in [99] and [100]. The Time Domain Back-Projection (TDBP) [65] was used for azimuth compression, and radiometric calibration was performed identically as for TDC.

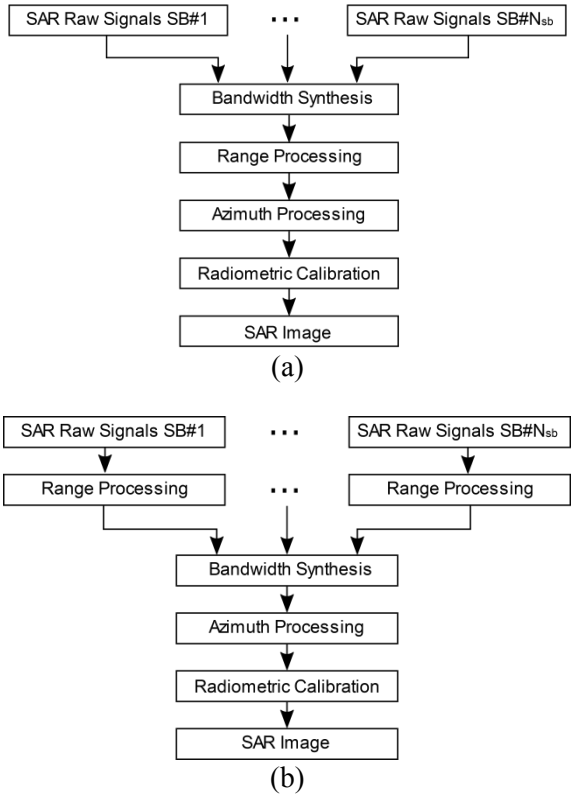

Fig. 2.2 Processing chain for stepped-frequency data sets. a) bandwidth synthesis before range processing. b) bandwidth synthesis after range processing.

2.3.3 Interferometric processing of multichannel SAR

The SAR images used to compute the Interferometric Coherence Images (ICIs) and the corresponding phase maps were obtained after applying one of the range compression techniques described in subsection 2.3.1 and the extended wavenumber domain azimuth compression method described in [100, 101]. The interferometric phase from the four receiving antennas was generated using a maximum likelihood phase estimation method [102]. The coherence value was calculated from the longest available baseline using the same range and azimuth looks as in the phase estimation.

2.3.4 Numerical evaluation

The data sets were first range compressed with the methods listed in Table 2.2. The Matched Filter (MF) was considered to be the reference pulse compression technique. After azimuth compression and radiometric calibration, both local and global quality indicators were computed from the focused intensity SAR images for image quality assessment.

Local indicators are obtained by extracting information about the backscatter from an isolated point target, and global indicators by extracting image-wide information [59-61]. The former were derived after averaging those extracted from the analysis of nine Point Spread Functions (PSFs) of three corner reflectors (trihedral) deployed in the area of interest. In this study, we used: 1) the slant range resolution δ_r and azimuth resolution δ_a derived from the 3dB width of the range and azimuth profiles of the PSF respectively; 2) the SNR, computed as the ratio of the main peak level of the PSF to the average level of a 128×128 sidelobe-free image patch of the airport runway, 3) the peak to sidelobe ratio in range PSLRr and azimuth PSLRa respectively, derived as the ratio between the main peak level to the averaged first sidelobe levels, and 4) the integrated sidelobe ratio in range ISLRr and azimuth ISLRa, defined as the inverse ratio of the total energy of the 3dB main peak response to the total energy of the rest of the range and azi-

muth profile respectively [61]. The profiles used to derive the ISLRr included the first two pairs of sidelobes, and one pair for ISLRa. Higher order sidelobes were below the dynamic range of the system. ΔSNR, ΔPSLRr, ΔPSLRa, ΔISLRr, and ΔISLRa were computed by subtracting the indicators derived from a patch of the corner reflector focused with a specific range compression method and the same indicators derived from the reference (MF), while $\delta_{\text{r-ratio}}$ and $\delta_{\text{a-ratio}}$ were derived by ratioing. Since the PSLRr accounts only for the first sidelobes, and the ISLRr depends on the number of available sidelobes, global quality indicators were used to evaluate the sidelobe reduction efficiency of a pulse compression method in comparison to that of the reference (MF).

TABLE 2.2
PULSE COMPRESSION METHODS – PARAMETERS

Method	**Nomenclature**	**Parameters**
Matched Filter	MF	-
Matched Filter with Kaiser window	MFK{β}	β: shape of the window for sidelobe attenuation
Mismatched Filter	MMF	-
Least Squares Mismatched Filter	LSMMF	-
APC	$\text{APC}_{\text{IS}}\{M\}$	IS: initialization stage, e.g. MF, MFK{β}, MMF or LSMMF *M*: number of stages
APC (MVM)	$\text{APC}_{\text{IS-MVM}}\{M\}$	Analog to APC
FAPC	$\text{FAPC}_{\text{IS}}\{M\}$	Analog to APC

A log-transformed intensity SAR image X can be expressed as the sum of an informative component (signal), white Gaussian noise, and an undesirable non-informative component due to artifacts ξ. Neglecting differences in the noise component and assuming that sidelobes are the main contribution in ξ, the energy difference ΔI between a SAR image X_i and the reference X_{MF} can be expressed as:

$$\Delta I_i = 10 \cdot log10(|X_i|^2) - 10 \cdot log10(|X_{MF}|^2) \approx \Delta SNR_i + \Delta\xi_i \tag{2.14}$$

where ΔSNR_i is the difference in SNR, $\Delta\xi_i$ the differences in energy due to sidelobes, and the subscript 'i' refers to the range compression method used to focus X (see nomenclature in Table II). By assuming that ΔSNR_i is constant for all image pixels and the SAR images have comparable spatial resolutions, $\Delta\xi_i$ can be derived from ΔI_i. Global indicators can be derived by thresholding $\Delta\xi_i$ at 0dB, comparable to change detection. The average energy reduction $\overline{\Delta\xi_{\text{red}}}$ and increase $\overline{\Delta\xi_{\text{inc}}}$ due to sidelobes are computed by integrating the values of the negative and positive class of $\Delta\xi$ respectively, and normalizing by the total number of pixels of X_{MF}. Ideally, $\overline{\Delta\xi_{\text{inc}}} = 0$ and $\overline{\Delta\xi_{\text{red}}} \ll 0$. Finally, the net energy difference per image pixel due to sidelobes $\overline{\Delta\xi_i}$ is computed with $\overline{\Delta\xi_i} = \overline{\Delta\xi_{\text{red}}} + \overline{\Delta\xi_{\text{inc}}}$. Images of $\Delta\xi_i$ were denoised with Block Matching 3-D (BM3D) described in [35].

Quality assessment of the interferometric phase is performed with the ICIs. High coherence between a pair of SAR images is correlated to reliable height information derived from the interferometric phase. Low coherence indicates noisy interferometric phase, which translates into unreliable height information or outliers [102, 103]. The quality of the phase estimates of an

interferometric set of SAR images focused with a pulse compression method in comparison to MF can be derived from the coherence difference ΔC_i via:

$$\Delta C_i = ICI_i - ICI_{MF} \tag{2.15}$$

where ICI_{MF} is the coherence of the interferometric set focused with the MF, and ICI_i is the coherence of the set being evaluated. ΔC_i is dimensionless and limited to the interval [-1, 1]. $\Delta C_i > 0$ indicates more reliable phase estimates, and $\Delta C_i < 0$ less reliable. An increase or decrease of coherence can have a positive impact depending on the underlying targets; e.g. a coherence increase can occur when targets are unmasked after sidelobe reduction, and a coherence decrease can occur in areas with inherent low coherence (shadows, asphalt, water...) obscured by sidelobes previous to unmasking. A pulse compression method provides reliable phase estimates when the corresponding ICIs deliver low coherence for highly de-correlating targets, and the opposite in coherent targets. A unique global indicator congesting the information embedded in ΔC_i could hardly assess quality of the phase estimates. To avoid such issues, ΔC_i was evaluated locally in patches where the coherence was affected by changes in sidelobes.

2.4 Results

2.4.1 Single channel SAR image focusing

The pulse compression techniques listed in Table 2.2 were applied for range compression of one channel of MEMPHIS data with 200 MHz bandwidth. The quality indicators were extracted after azimuth compression and radiometric calibration. The signatures of nine corner reflectors were used to extract the local quality indicators. Intensity SAR images of one of these corner reflectors focused with different range compression methods are shown in Fig. 2.3 (a-d). The differences between local indicators obtained with traditional compression schemes (see Fig. 2.1) versus the MF are listed in Table 2.3. Only the LSMMF method preserved spatial resolution with a marginal SNR loss.

For MFK{β} and MMF, ΔPSLRr and ΔISLRr are not provided, as the main lobe broadened to include the first sidelobes in these cases. Table 2.4 lists the corresponding differences between local quality indicators obtained with the APC variants, using different initialization stages and number of stages *M*. The adaptive processing methods provided slightly better resolution, similar to LSMMF, involving a maximum SNR loss of 0.17 dB. The first range sidelobes increased by approximately 2 dB in comparison to the MF as indicated by ΔPSLRr. Nonetheless, ΔISLRr computed with the first two sidelobes was on average 0.03 dB lower than that of X_{MF}. Fig. 2.3 (e) depicts the range profiles of the corner reflector obtained with different pulse compression schemes, showing that some sidelobes were reduced but others increased. This explains the disagreement between ΔPSLRr and ΔISLRr. With millimeter precision, the azimuth resolution δ_a was consistently measured as 0.1 m independently of the range compression method; similarly the values of ΔPSLRa and ΔISLRa were on average -0.13 dB, and -0.04 dB respectively, indicating that the APC-based methods respected the range-azimuth coupling in SAR.

TABLE 2.3
LOCAL QUALITY INDICATORS FOR TRADITIONAL TECHNIQUES

Range compression method	**ΔSNR (dB)**	**$\delta_{r\text{-}ratio}$**	**ΔPSLRr (dB)**	**ΔISLRr (dB)**	**ΔPSLRa (dB)**	**ΔISLRa (dB)**
MFK {β =10}	-3.54	1.92	N/A	N/A	0.05	-0.01
MMF	-0.49	1.44	N/A	N/A	-0.26	0.01
LSMMF	-0.16	0.96	1.82	0.05	-0.09	-0.03

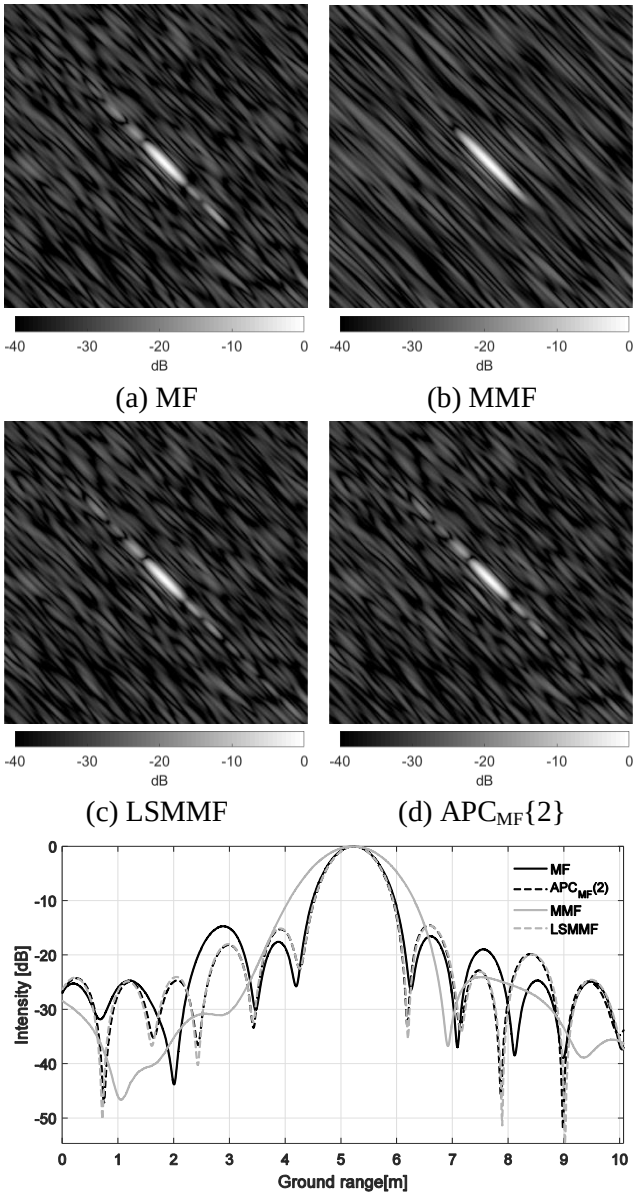

Fig. 2.3 Analysis of the PSF of a corner reflector. (a-d) Intensity SAR images focused with MF, MMF, LSMMF and $APC_{MF}\{2\}$. (e). Range profiles.

In global terms, the sidelobe reduction efficiency offered by the different methods was evaluated using $\Delta\xi$ described in section 2.3.4. Fig. 2.4 (a-b) illustrates the intensity images focused with the MF and $APC_{MF}\{2\}$ respectively. Fig. 2.4 (c-f) shows $\Delta\xi_{\text{APC-MF}\{2\}}$, $\Delta\xi_{\text{LSMMF}}$, $\Delta\xi_{\text{APC-MF-MVM}\{2\}}$ and $\Delta\xi_{\text{APC-MF-MVM}\{3\}}$. Blue pixels indicate a reduction of sidelobes, and red an increase. Fig. 2.5 depicts the histogram of $\Delta\xi_{\text{APC-MF}\{M\}}$ and $\Delta\xi_{\text{APC-MF-MVM}\{M\}}$, with M=2,3 and $\Delta\xi_{\text{LSMMF}}$. For techniques preserving spatial resolution, the indicators $\overline{\Delta\xi_{\text{red}}}$, $\overline{\Delta\xi_{\text{inc}}}$, and $\overline{\Delta\xi}$ are listed in Table 2.5. The histograms of the APC-based methods were slightly shifted towards the negative side of the x-axis, indicating that the energy of the corresponding SAR images was lower than that of the MF due to sidelobes. This was also confirmed by $\overline{\Delta\xi}$ listed in Table 2.5. Local and global quality indicators indicated that the sidelobe reduction efficiency of APC depended on the initialization stage and the number of stages M. Values of $\overline{\Delta\xi_{\text{red}}}$ indicated that if

the *M*-1 stage was derived by pulse compression methods providing moderate to high sidelobe levels, like MF and LSMMF, then sidelobes at stage *M* were slightly reduced for increasing *M*. However, the energy of some sidelobes increased with *M*, as indicated by $\overline{\Delta\xi_{inc}}$. In general, local and global indicators showed that the sidelobe reduction efficiency degraded with increasing *M*. This behavior was also confirmed by the histograms in Fig. 2.5 and simulation results given in the Appendix. Best results were obtained for *M*=2 using an initialization stage providing range profiles with reduced sidelobes, such as the MMF and the MFK{β}. In all cases, the SNR loss decreased with *M*.

TABLE 2.4
LOCAL QUALITY INDICATORS FOR ADAPTIVE PROCESSING

Range compression method	**ΔSNR (dB)**	**$\delta_{r\text{-}ratio}$**	**ΔPSLRr (dB)**	**ΔISLRr (dB)**
$APC_{MF}\{2\}$	-0.16	0.96	1.85	-0.02
$APC_{MF}\{3\}$	-0.08	0.95	1.87	-0.03
$APC_{MFK\{10\}}\{2\}$	-0.16	0.95	1.96	-0.03
$APC_{MFK\{10\}}\{3\}$	-0.08	0.95	1.75	-0.03
$APC_{MMF}\{2\}$	-0.16	0.95	1.93	-0.04
$APC_{MMF}\{3\}$	-0.08	0.95	1.73	-0.03
$APC_{LSMMF}\{2\}$	-0.17	0.95	1.90	-0.01
$APC_{LSMMF}\{3\}$	-0.09	0.95	1.97	-0.05
$APC_{MF\text{-}MVM}\{2\}$	-0.07	0.95	1.98	-0.07
$APC_{MF\text{-}MVM}\{3\}$	-0.03	0.95	2.15	-0.04
$APC_{MFK\{10\}\text{-}MVM}\{2\}$	-0.06	0.94	2.04	-0.07
$APC_{MFK\{10\}\text{-}MVM}\{3\}$	-0.02	0.94	2.15	-0.04
$APC_{MMF\text{-}MVM}\{2\}$	-0.07	0.95	2.02	-0.01
$APC_{MMF\text{-}MVM}\{3\}$	-0.02	0.95	2.01	-0.04
$APC_{LSMMF\text{-}MVM}\{2\}$	-0.07	0.95	2.03	-0.03
$APC_{LSMMF\text{-}MVM}\{3\}$	-0.02	0.94	2.05	-0.05

TABLE 2.5
GLOBAL QUALITY INDICATORS FOR PULSE COMPRESSION SCHEMES PRESERVING RESOLUTION

Range compression method	**$\overline{\Delta\xi_{red}}$ (dB/pix)**	**$\overline{\Delta\xi_{inc}}$ (dB/pix)**	**$\overline{\Delta\xi}$ (dB/pix)**
$APC_{MF}\{2\}$	-2.12	1.32	-0.80
$APC_{MF}\{3\}$	-2.15	1.45	-0.70
$APC_{MFK\{10\}}\{2\}$	-2.30	1.48	-0.82
$APC_{MFK\{10\}}\{3\}$	-2.26	1.55	-0.71
$APC_{MMF}\{2\}$	-2.30	1.48	-0.82
$APC_{MMF}\{3\}$	-2.25	1.51	-0.74
$APC_{LSMMF}\{2\}$	-2.02	1.37	-0.65
$APC_{LSMMF}\{3\}$	-2.12	1.46	-0.66
$APC_{MF\text{-}MVM}\{2\}$	-1.98	1.82	-0.16
$APC_{MF\text{-}MVM}\{3\}$	-1.97	1.52	-0.45
$APC_{MFK\{10\}\text{-}MVM}\{2\}$	-1.98	1.82	-0.16
$APC_{MFK\{10\}\text{-}MVM}\{3\}$	-2.01	1.56	-0.45
$APC_{MMF\text{-}MVM}\{2\}$	-2.01	1.64	-0.37
$APC_{MMF\text{-}MVM}\{3\}$	-2.02	1.54	-0.48
$APC_{LSMMF\text{-}MVM}\{2\}$	-1.86	1.52	-0.34
$APC_{LSMMF\text{-}MVM}\{3\}$	-1.96	1.52	-0.44
LSMMF	-1.52	1.21	-0.31

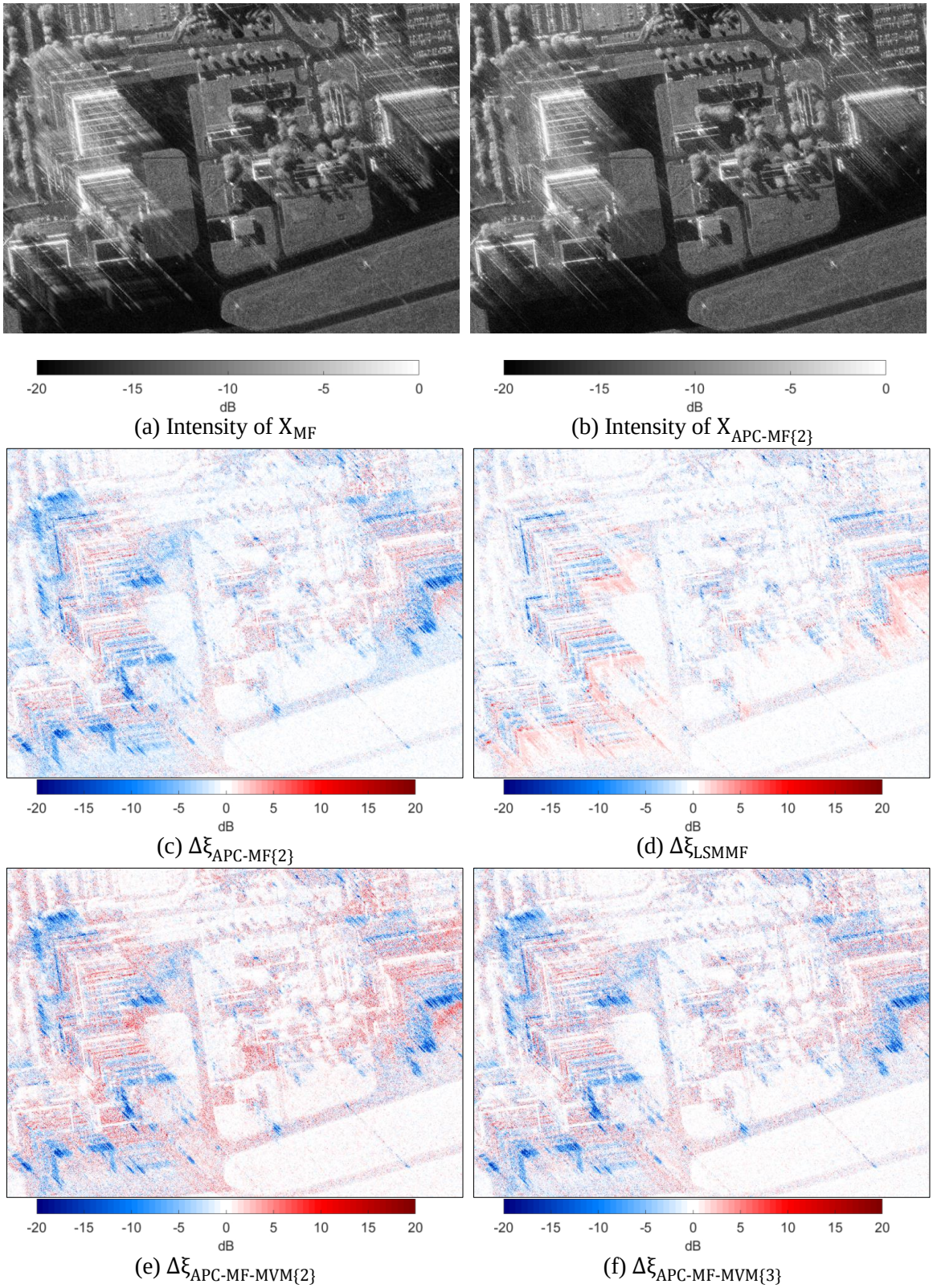

Fig. 2.4 Single-channel intensity SAR images and denoised $\Delta\xi$ obtained for different range focusing schemes. The SAR images were geocoded and georeferenced in the German Gauss-Krüger zone 4 coordinate system. Northing corresponds to the vertical axis, Easting corresponds to the horizontal axis. The extent of the area of interest is 512x370 m^2.

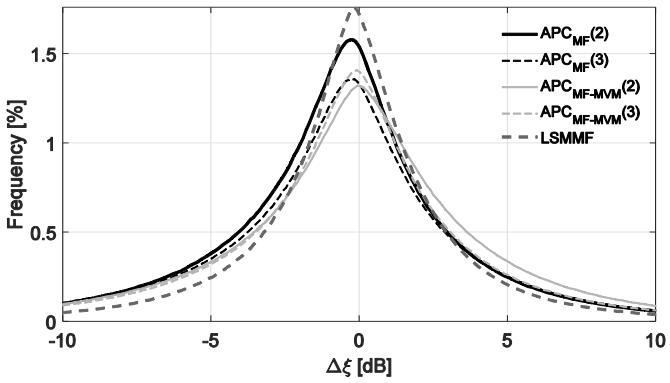

Fig. 2.5 Histograms of Δξ for APC, APC_{MVM} and LSMMF. Bin width=0.01dB.

The performance of APC_{MVM} depends also on the initialization stage and *M*. In general, based on the indicators $\overline{\Delta\xi_{inc}}$, increased sidelobes at stage *M*-1 decreased with *M*, except for $APC_{LSMMF\text{-}MVM}$. This behavior can be observed by comparing red areas of Fig. 2.4 (e) and Fig. 2.4 (f). The values of $\overline{\Delta\xi}$ indicated that APC_{MVM} required more stages to achieve a sidelobe reduction efficiency similar to APC{2}. Comparison of Fig. 2.4 (c-f) highlights this behavior. Similar to APC, the SNR loss was reduced with increasing number of stages.

LSMMF provided moderate sidelobe reduction efficiency in comparison to that of APC. The values of $\overline{\Delta\xi_{red}}$ and $\overline{\Delta\xi_{inc}}$ show moderate sidelobe reduction or increase. Comparison of Fig. 2.4 (c-d) shows the difference in sidelobe reduction efficiency.

2.4.2 Single channel SAR image focusing with frequency agility

Based on the previous results, we applied $APC_{MF}\{2\}$ to each stepped frequency sub-band (eight in total), proceeding as $FAPC_{MF}\{2\}$. After synthesizing the full bandwidth of the range profiles, azimuth compression and radiometric calibration were performed as described in section 2.3.2. The previous procedure was repeated with the MF method, as well as with the LSMMF range focusing scheme. Fig. 2.6 (a-b) show the SAR image of the area of interest, obtained by applying MF and $FAPC_{MF}\{2\}$. The local quality indicators calculated from the signatures of the corner reflectors were similar for all methods. $FAPC_{MF}\{2\}$ and LSMMF yielded a maximum SNR loss of 0.18 dB and 0.21 dB respectively. ΔPSLRr was 0.07 dB for LSMMF and 0.02 dB for $FAPC_{MF}\{2\}$. In all cases, the values of ΔISLRr were below -0.1 dB, and $\delta_{r\text{-}ratio}$ and $\delta_{a\text{-}ratio}$ were consistently measured as 0.99 and 1.00 respectively. The PSLRa and ISLRa were very similar for all methods, differing by less than 0.03 dB. Fig. 2.6 (c-d) show $\Delta\xi_{FAPC\text{-}MF\{2\}}$ and $\Delta\xi_{LSMMF}$ after denoising via BM3D. Blue pixels indicate areas with reduced sidelobes. Fig. 2.7 depicts the histograms of $\Delta\xi_{FAPC\text{-}MF\{2\}}$ and $\Delta\xi_{LSMMF}$. Both histograms were slightly shifted towards the negative side of the x-axis, indicating that the energy of the corresponding SAR images was lower than that of the MF due to sidelobe reduction. This was also confirmed by the global quality indicators listed in Table 2.6. Inter-comparison of $\overline{\Delta\xi}_{APC\text{-}MF\{2\}}$ in Table 2.5 and $\overline{\Delta\xi}_{FAPC\text{-}MF\{2\}}$ in Table 2.6 highlights the sidelobe reduction efficiency loss of FAPC. In contrast, the performance of LSMMF improved when applied to stepped-frequency data sets.

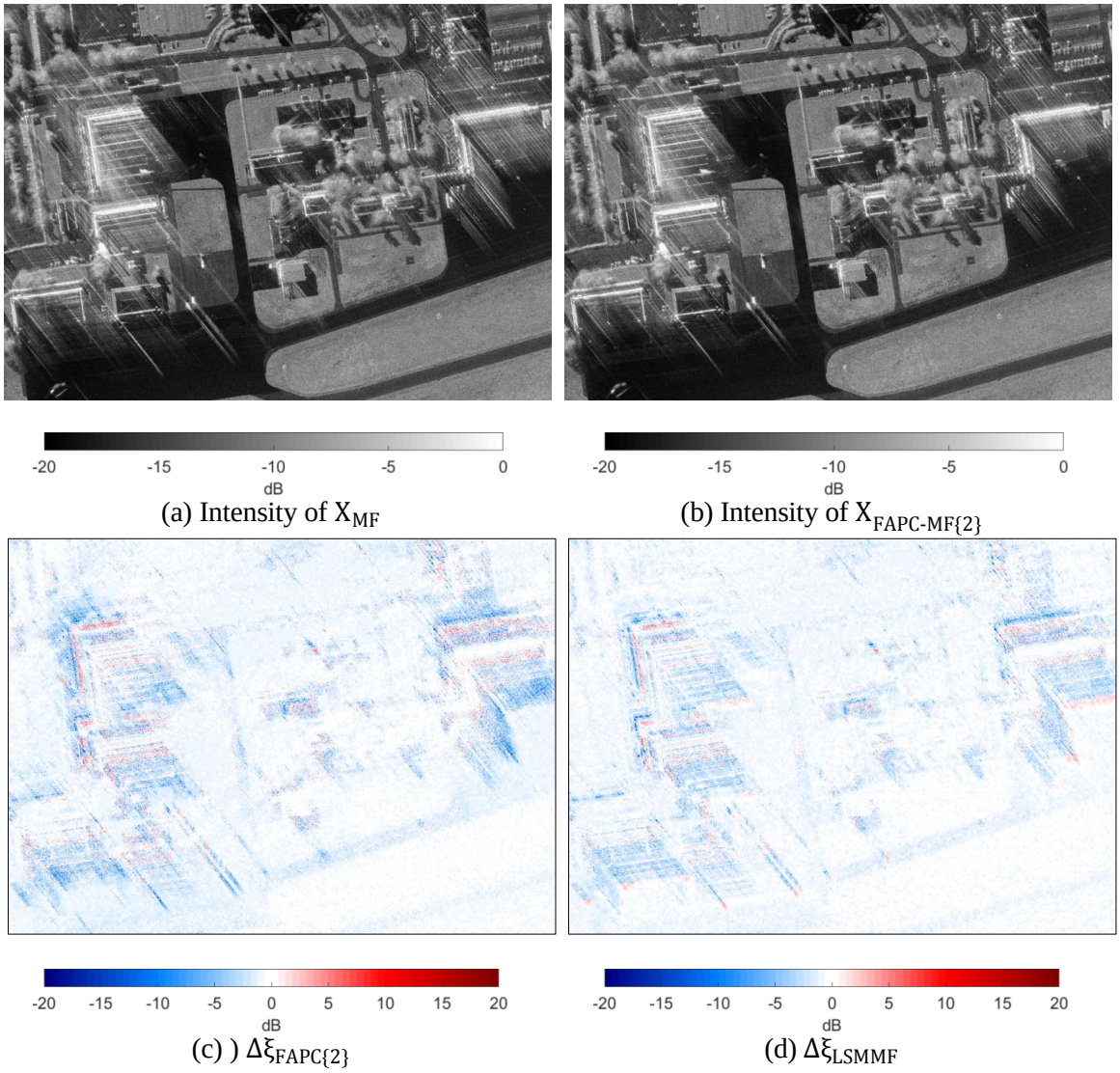

Fig. 2.6 Intensity SAR images and denoised Δξ obtained for different range focusing schemes after range bandwidth synthesis (stepped-frequency). The SAR images were geocoded and georeferenced in the German Gauss-Krüger zone 4 coordinate system. Northing corresponds to the vertical axis, Easting corresponds to the horizontal axis. The extent of the area of interest is 512x370 m^2.

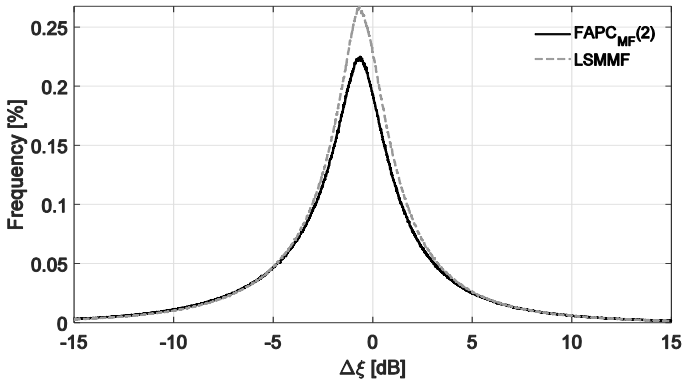

Fig. 2.7 Histograms of Δξ for FAPC and LSMMF. Bin width=0.01dB.

TABLE 2.6
GLOBAL QUALITY INDICATORS FOR FAPC AND LSMMF

Range compression method	$\overline{\Delta\xi_{red}}$ **(dB/pix)**	$\overline{\Delta\xi_{inc}}$ **(dB/pix)**	$\overline{\Delta\xi}$ **(dB/pix)**
$FAPC_{MF}\{2\}$	-1.76	1.19	-0.57
LSMMF	-1.54	1.15	-0.39

2.4.3 Interferometric processing of multichannel SAR

To evaluate the performance of APC for interferometric processing, we computed local quality indicators based on the ICIs. Fig. 2.8 (a) shows the SAR image of an interferometric channel without frequency agility. The image was focused using MF in range and extended wavenumber domain in azimuth [101]. $\Delta C_{APC\text{-}MF\{2\}}$ is shown in Fig. 2.8 (b).

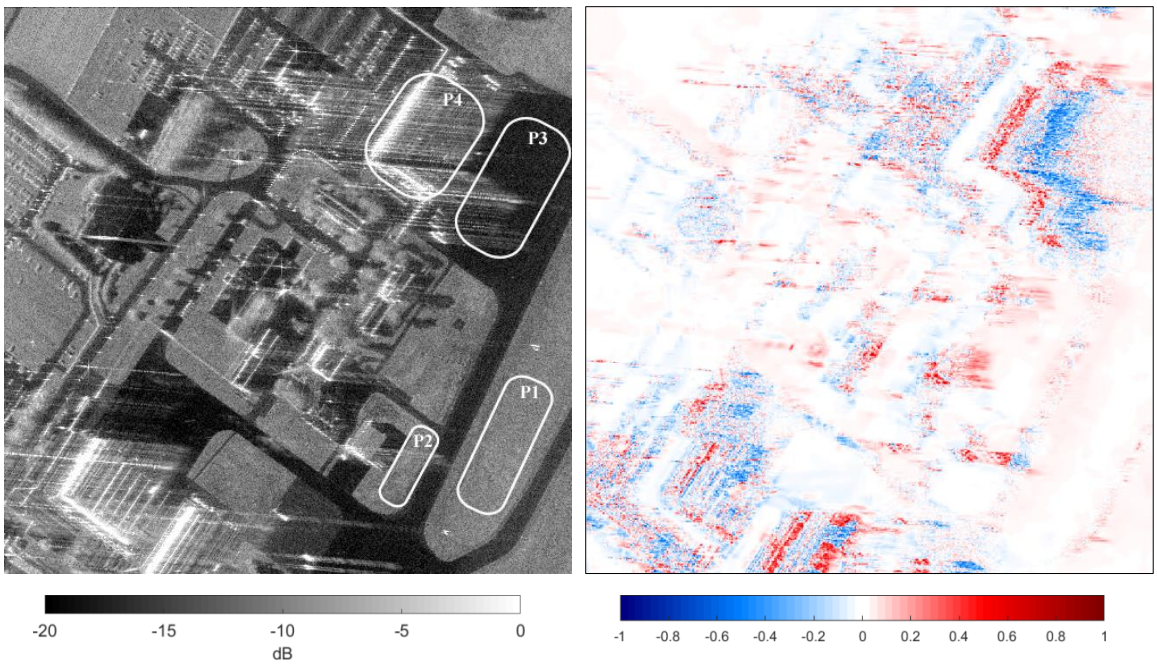

(a) Intensity of X_{MF} (b) $\Delta C_{APC\text{-}MF\{2\}}$

Fig. 2.8 Backscatter of the SAR image of the area of interest and $\Delta C_{APC\text{-}MF\{2\}}$. The images are shown in slant-range geometry, where azimuth corresponds to the vertical axis, and range corresponds to the horizontal axis.

Table 2.7 describes the patches shown in Fig. 2.8 (a), including the average coherence $\overline{ICI_i}$ and approximate area of each patch. Numerical evaluation of $\overline{ICI_i}$ for patch P1 shows that APC increased coherence in sidelobe-free areas with signal component, but FAPC offered slightly lower coherence. For P2, the corresponding values for unmasked targets with signal component delivered better coherence. On the contrary, numerical evaluation of patch P3 indicates that APC and FAPC reduced coherence of unmasked decorrelating targets. Numerical evaluation of P4 indicates that in overall terms both APC and FAPC reduced coherence in areas with presence of unmasked targets with signal component such as the terminal.

TABLE 2.7
COHERENCE-BASED QUALITY ASSESSMENT

Region of interest	**Area (m^2)**	**One sub-bandwidth**		**Stepped frequency**	
		$\overline{ICI_{MF}}$	$\overline{ICI_{APC}}$	$\overline{ICI_{MF}}$	$\overline{ICI_{FAPC}}$
P1, Grassland (sidelobe-free)	3400	0.889	0.896	0.917	0.914
P2, Grassland	1300	0.753	0.811	0.847	0.876
P3, Concrete airport apron	5300	0.347	0.321	0.275	0.262
P4, Airport terminal	5600	0.546	0.480	0.478	0.427

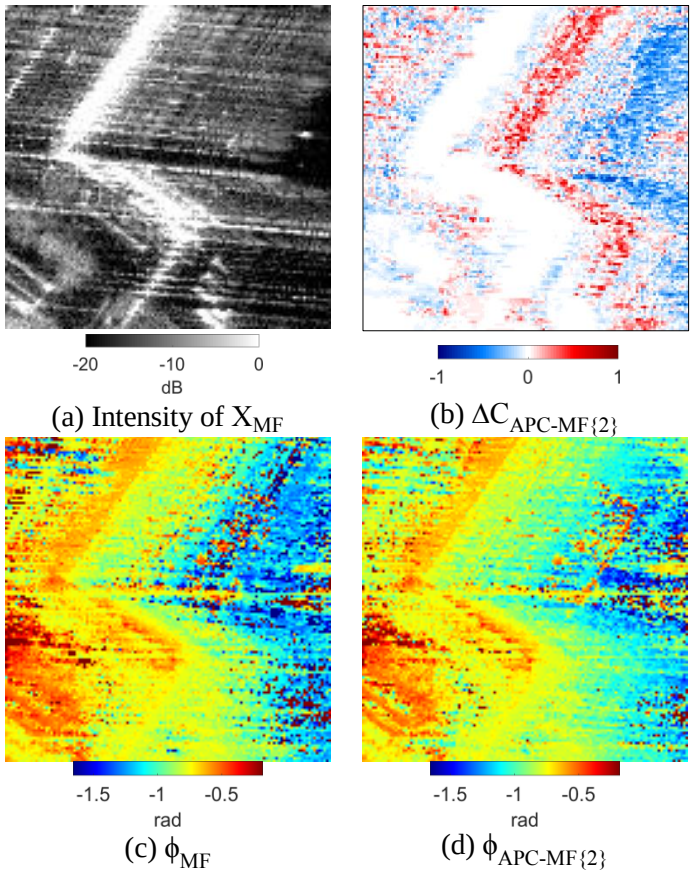

(a) Intensity of X_{MF} (b) $\Delta C_{APC\text{-}MF\{2\}}$

(c) ϕ_{MF} (d) $\phi_{APC\text{-}MF\{2\}}$

Fig. 2.9 Intensity SAR image, $\Delta C_{APC\text{-}MF\{2\}}$ and phase maps of the terminal of the airport. The images are shown in slant-range geometry, where azimuth corresponds to the vertical axis, and range corresponds to the horizontal axis.

Fig. 2.9 (a) shows the intensity SAR image of a patch of the terminal of the airport, very similar to P4. From numerical evaluation in Table 2.7, the coherence of the patch was lower when applying APC, but some areas of the patch experienced an increase of coherence as shown in red in Fig. 2.9 (b). The red areas were in principle undesirable as they correspond to an increase of coherence due to increased sidelobes which could introduce artifacts in the corresponding phase map. Comparison of the phase maps ϕ_{MF} and $\phi_{APC\text{-}MF\{2\}}$ in Fig. 2.9 (c-d) showed that the latter is more homogenous, and the areas experiencing a coherence increase did not introduce outliers. Additionally, the roof-edge of the terminal became visible in $\phi_{APC\text{-}MF\{2\}}$, indicating that APC was able to better preserve the phase information of the signals scattered by the roof-edge.

2.5 Discussion

2.5.1 Performance of APC for single channel SAR image focusing

With MF focusing, the SAR images were characterized by prominent range sidelobes, as seen in Fig. 2.4 (a) and Fig. 2.6 (a). Some sidelobes may also be introduced due to a mismatch of the recorded real replicas and the LFM signals of the received pulses [104]. Possible reasons of signal mismatch are: a) amplitude and phase imbalances at IQ demodulation stage [105, 106], and b) saturation and clipping in the receiver of the radar returns coming from targets characterized by a strong backscatter [107].

Based on the results listed in Table 2.4, APC-based methods yielded a maximum SNR loss of 0.17 dB. This can be considered negligible in comparison to those obtained by classical windowing, where the SNR loss is usually above 1 dB [67]. For simplicity, the SNR loss was evaluated locally using the backscatter from corner reflectors deployed far from potential targets with strong backscatter. It is reasonable to assume that MF is lossless from the SNR point of view considering the isolated point target scenario. However, this situation is exceptional in SAR imagery and thus it is not possible to assure that MF provides the lowest SNR loss in global terms with range profiles of multiple point-like and distributed targets.

Numerical evaluation listed in Table 2.4 and Table 2.5 indicates that for small M, both APC and APC_{MVM} introduce a trade-off between SNR loss and sidelobe reduction efficiency. However, for larger M, both local and global quality indicators suggest that the performance of APC degrades in terms of effective sidelobe reduction while the opposite occurs for APC_{MVM}. Graphical results in Fig. 2.4 and Fig. 2.5, and simulation results given in the Appendix also indicated such behavior.

When applying APC, the highest energy reduction was achieved in the second iteration, independently of the APC variant and the initialization stage. This suggests that two iterations of APC were sufficient to reduce sidelobes inherited by the initialization stage to the noise level. Such behavior was also reported in [91].

Fig. 2.4 (c) illustrates the sidelobe reduction efficiency of $\text{APC}_{\text{MF}}\{2\}$ in comparison to that of the MF, showing that higher order sidelobes were severely reduced. However, lower order sidelobes suffered a weaker reduction or even an increase (red areas in Fig. 2.4 and Fig. 2.6). This behavior could be due to a mismatch between the replica and received LFM signals. Simulation results reported in Table 2.9 in the Appendix demonstrate that the performance of the APC-based methods degrades under mismatch conditions, yielding an increase of some sidelobes and a higher SNR loss. Fig. 2.4 (d) shows that LSMMF also increased and reduced different sidelobes. If desired, complex dual apodization can be performed to further reduce sidelobes [79].

For pulse radar without imaging capabilities, the sidelobe reduction efficiency of the APC-based methods and mismatch filters has been found moderate when the transmitted waveform was an LFM signal [91]. Many mismatched filters can in general preserve resolution and SNR. This might not occur with LFM signals, even when the mismatched filter can be derived from this type of signal. The reason is that LFM signals can neither minimize crosstalk between frequencies nor be designed to obtain a thumbtack ambiguity function [64].

The performance of APC-based methods was evaluated using high resolution airborne SAR imagery. The potential improvements offered for lower resolution data sets may be less significant, depending on the properties of the transmitted waveform, electronic equipment and transmitted power. For lower spatial resolution, sidelobes introduced by the MF can be expected to be lower due to the properties of the ambiguity function (constant volume) of the transmitted waveform [64].

2.5.2 Performance of FAPC for single channel SAR image focusing with frequency agility

Similar to APC, FAPC preserves spatial resolution and yields a negligible SNR loss, while respecting the range-azimuth coupling of SAR. FAPC decreases dimensionality by exploiting a set of weighted covariance matrices computed with diverse spectral parts of the transmitted waveform, so the computation time reduces drastically in comparison to APC. However, FAPC yields modest improvements in terms of sidelobe level reduction, as shown in Fig. 2.6 in comparison to those in Fig. 2.4, and numerical evaluation in Table 2.5 and Table 2.6.

FAPC can introduce azimuth artifacts when applied to a single sub-band; however, both quality indicators and visual inspection did not reveal artifacts when applied to each stepped-frequency sub-band. The combination of FAPC with the SAR range-azimuth coupling, which increases dimensionality, introduces a wrinkle in adaptive processing vaguely explored. It is not clear how large or small the partition of the frequency components of the transmitted waveform should be to provide high quality SAR imagery. A more detailed analysis of the potential usage of FAPC as a range focusing scheme for SAR image formation is still required.

2.5.3 Performance of APC and FAPC for interferometric processing of multichannel SAR

Based on the ICIs computed from the interferometric data sets, the evaluation of the performance of the APC variants required careful analysis. An increase or decrease of the coherence can positively impact the final estimation of the interferogram via the phase noise, which is directly related to the coherence [102]; i.e. the higher the coherence, the lower the phase noise. When calculating height maps from interferograms, low-coherence areas are filtered out to reduce outliers. Therefore, a decrease of coherence in areas where its value is low (asphalt, water…) implies a reduction of outliers, and thus a flatter response, in the final height map. On the other hand, a coherence increase of correlating targets improves the accuracy of the height map. Numerical evaluation in Table 2.7 and results in Fig. 2.8 shows that APC provides increased coherence (implying more reliable phase estimates) for unmasked targets with significant backscatter. As expected, unmasked de-correlating targets experienced a coherence reduction. For sidelobe-free areas, APC showed similar coherence to that of MF. Image areas experiencing an increase of coherence due to an increase of sidelobes require further analysis; however, visual inspection revealed that this undesired effect was not transferred to the phase map given in Fig. 2.9 (d), and thus the corresponding height maps did not suffer from associated artifacts. In this study, some areas, such as P4, experienced coherence improvement due to increased sidelobes in the corresponding intensity SAR images. The P4 area was further evaluated via the phase maps. A more detailed evaluation could be performed by inter-comparing the Digital Surface Model (DSM) obtained from the interferometric data set with an up-to-date and accurate reference DSM. However, the available DSM of the area of interest does not provide the necessary resolution and accuracy to perform this evaluation.

The performance of FAPC regarding the reliability of the phase estimates was moderate. Quality assessment of the ICIs of the data set acquired in frequency agility mode showed this lower performance, as reported in Table 2.7.

2.6 Conclusions

A variety of adaptive processing techniques were applied to range compression in SAR image focusing and evaluated under real and ideal conditions. In contrast to traditional methods such as matched and mismatched filtering, APC was shown to preserve resolution and reduce sidelobes with only marginal SNR loss; and thus, improving the quality of the corresponding SAR images. Based on analysis of local and global quality indicators, APC was shown to pre-

serve the characteristics of the azimuth signals (resolution and sidelobes), and could be used independently of the azimuth compression method.

For frequency agile systems, APC was compared to FAPC using stepped-frequency data sets. FAPC yielded modest improvements, offering lower sidelobe reduction efficiency, but also lower computation times; however, the performance of FAPC requires further analysis. For stepped-frequency data sets, FAPC provided range profiles with lower sidelobe levels in comparison to those obtained by matched or mismatched filters.

APC brought significant improvements with interferometric data sets, providing more reliable phase estimates than the matched filter for unmasked targets with significant backscatter. This behavior confirmed that APC provides both better amplitude and phase estimates of the range profiles.

In future work, we plan to further evaluate the performance of FAPC, and introduce fast solutions to apply APC also to azimuth compression. Adaptations of APC to dechirp signals of Frequency Modulated Continuous Wave (FMCW) SAR systems are also a possibility.

Acknowledgments

The authors would like to acknowledge armasuisse W+T for financial and operational support. We also thank the Fraunhofer FHR team and in particular Thorsten Brehm, as well as the pilots and all institutions involved in the MEMPHIS data collection, and Christian Ackermann from the TU Munich for lending the IMU hardware. The authors would specifically like to thank the reviewers for their helpful contributions in improving this paper.

2.7 Appendix

2.7.1 List of Acronyms

TABLE 2.8
LIST OF ACRONYMS USED IN THE TEXT

APC	Adaptive Pulse Compression
APES	Amplitude and Phase Estimation
BM3D	Block Matching 3D
FAPC	Fast Adaptive Pulse Compression
FMCW	Frequency Modulated Continous Wave
HDVI	High Definition Vector Imaging
ICI	Interferometric Coherence Image
IS	Initialization Stage
LFM	Linear Frequency Modulation
LSMMF	Least Squares Mismatched Filter
MF	Matched Filter
MFK	Matched Filter with Kaiser window
MMF	Mismatched Filter
MMSE	Minimum Mean Square Error
MVM	Minimum Variance Method
PSF	Point Spread Function
RFI	Radio Frequency Interference
SAR	Synthetic Aperture Radar
SNR	Signal to Noise Ration
SVA	Spatially Variant Apodization
TDBP	Time Domain Back-Projection
TDC	Time Domain Correlation

2.7.2 Simulation results

The signature of a corner reflector was simulated using the signal properties (bandwidth, duration, frequency sampling, carrier frequency, and polarization) of a 200 MHz bandwidth chirp of MEMPHIS data. The simulated received signals were range compressed with MF, LSMMF, APC and APC_{MVM}. The APC variants were initialized with the range profiles provided by MF. Signal mismatch was simulated by using a real and a synthetic replica. Fig. 2.10 shows one side of the normalized range profiles extracted from the PSF of the corner reflector. The absence of mismatch, APC reduced all sidelobes in comparison to MF; however its performance degraded when the received signals and the replica did not perfectly match; e.g. the first, third and fourth sidelobes were higher than those provided by MF. The local quality indicators listed in Table 2.9 confirm lower sidelobe reduction efficiency and a higher SNR loss. The SNR was measured using the maximum peak response and a 128×128 image patch outside the PSF of the corner reflector. With an accuracy of one millimeter, the values of $\delta_{\text{a-ratio}}$ were 1.00 in all cases. The values of ΔPSLRa were below -0.12 dB for all investigated methods.

TABLE 2.9
LOCAL QUALITY INDICATORS FROM SIMULATED CORNER REFLECTOR

Signal Matching	**Range compression method**	**ΔSNR (dB)**	**$\delta_{r\text{-}ratio}$**	**ΔPSLRr (dB)**
Ideal	$APC_{MF}\{2\}$	-0.07	0.95	-0.75
	$APC_{MF}\{3\}$	-0.02	0.94	-0.63
	$APC_{MF\text{-}MVM}\{2\}$	-0.02	0.95	-0. 65
	$APC_{MF\text{-}MVM}\{3\}$	0.00	0.94	-0.72
	LSMMF	-0.11	0.95	-0.67
Real	$APC_{MF}\{2\}$	-0.11	0.95	1.74
	$APC_{MF}\{3\}$	-0.04	0.94	1.83
	$APC_{MF\text{-}MVM}\{2\}$	-0.05	0.95	1.76
	$APC_{MF\text{-}MVM}\{3\}$	0.00	0.94	1.84
	LSMMF	-0.16	0.95	1.73

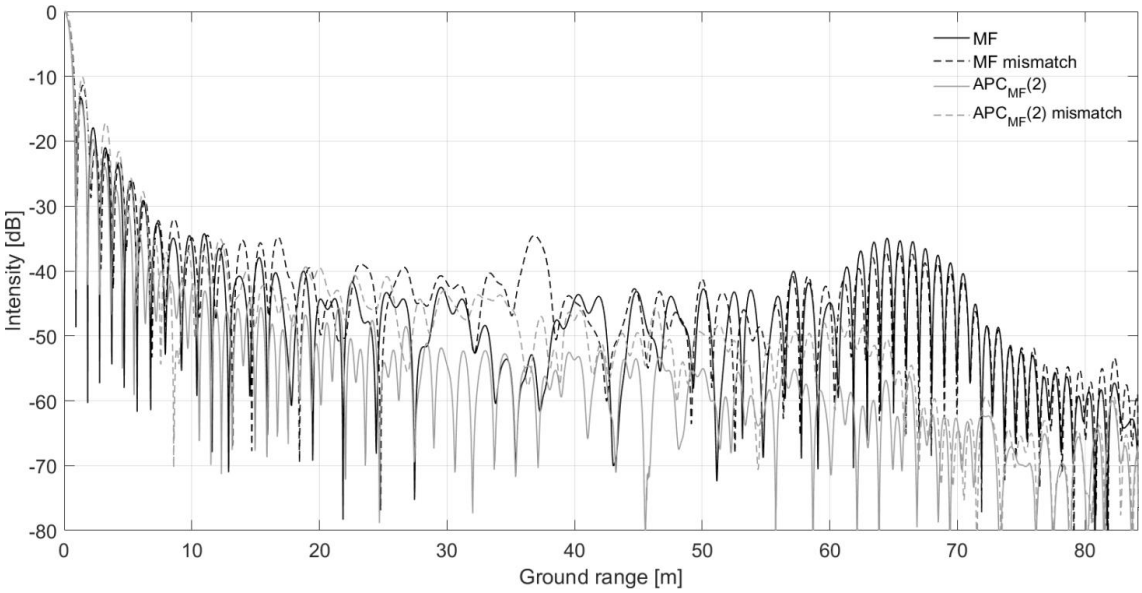

Fig. 2.10 Range profiles extracted from a simulated signature of a corner reflector with and without signal mismatch for MF (black) and $APC_{MF}\{2\}$ (gray).

3 A MULTISQUINT FRAMEWORK FOR CHANGE DETECTION IN HIGH-RESOLUTION MULTITEMPORAL SAR IMAGES

This chapter has been published as: E. M. Domínguez, E. Meier, D. Small, M. E. Schaepman, L. Bruzzone, and D. Henke, "A Multisquint Framework for Change Detection in High-Resolution Multitemporal SAR Images," *IEEE Transactions on Geoscience and Remote Sensing*, vol. 56, no. 6, pp. 3611-3623, 2018.

E.M.D. and E.M. designed the study. E.M.D. developed the methodology and analyzed the data with scientific advice of D.H., L.B. and M.E.S. All authors wrote the manuscript, with main contributions of E.M.D.

GLOSSARY OF NOTATION AND SYMBOLS OF THE MAIN VARIABLES IN THE TEXT

$x(E_0, N_0)$	Backscatter element of a single-look SAR image x at map coordinates (E_0, N_0)
$\ddot{x}(E_0, N_0, \Delta\theta)$	Backscatter element of a squint $\ddot{x}$ focused with an angular selectivity bandwidth of $\Delta\theta$ at map coordinates (E_0, N_0)
θ_a	Azimuth beamwidth of the antenna gain pattern
DI_{MCA}	Sum of the morphological components of the difference image derived from single-look processing
$W(\mathrm{m}, \mathrm{n})$	Beamforming function used for focusing the *n*th squint at the *m*th resolution scale
$\{\ddot{x}(\Delta\theta_\mathrm{m})\}$	Set of squints focused with an angular selectivity bandwidth of $\Delta\theta_\mathrm{m}$
$\{\ddot{x}(\Delta\theta)\}$	Set of squints focused with an angular selectivity bandwidth of $\Delta\theta$
$\{X_{MS}(m)\}$	Set of images derived by combining and filtering the squints at the *m*th resolution scale
$DI_{MS(m)-MCA}$	Sum of the morphological components of the difference image derived from multisquint processing
FCM_{pix}	Change map obtained after fusion at the pixel level
FCM_{obj}	Change map obtained after fusion at the object level
F_{ov}	Overlapping factor

Abstract

Change detection from multitemporal Synthetic Aperture Radar (SAR) images enables mapping applications for Earth environmental observation, human activity monitoring and urban studies. We expand the use of SAR data beyond single-look processing to include the spatial response of targets. This information is derived from a multisquint framework similar to beamforming. To preserve changes detected at nominal resolution, a three-stage change detector exploiting single-look and multisquint processing mode is proposed to mitigate false alarms caused by image artifacts typically found in high resolution SAR imagery and urban scenarios.

After applying the proposed method to multitemporal images, the false alarm rate was reduced by a factor 3, while preserving 95% of the detection rate offered by traditional schemes.

3.1 Introduction

Image change detection is an approach comparing two or more images of the same area acquired at different times. This procedure is particularly useful for urban studies [17-20], human activity monitoring [21], risk management [4, 6], and environmental observations [2]. Some of these applications require collecting data independently of weather and daylight conditions. For this reason, SAR offers a valuable alternative to optical sensors providing time series data with fine temporal and spatial resolutions. However, the complexity of SAR data imposes challenges that require careful consideration for change detection purposes: e.g. noise suppression, image mis-registration [57], calibration, and defocusing errors [14].

Typically, incoherent single-channel SAR image change detection is performed based on single-look images. Such products provide the highest attainable resolution and Signal to Noise Ratio (SNR). For this reason, the design of most change detectors has focused on mitigating errors caused by noise [13, 24, 44, 75]. Single-look images do not provide the full information content captured in the original raw data, such as spectral, spatial and short-term temporal responses of the targets. Neglecting this information has led to a large number of change detectors that consider SAR images as noise-corrupted versions of those that, for instance, could be recorded by optical sensors. Spectral information can be utilized to reduce noise via multi-look processing [108, 109], where multiple images are formed with different spectral components of the range and azimuth signals. This processing mode has been exploited in [14] for change detection purposes using single-channel SAR, and in [50, 52] using multichannel SAR data. Apart from noise-induced errors, the presence of image artifacts [63], such as side-lobes and azimuth ambiguities, increases the false alarm rate, degrading the interpretability of the change maps. Image artifacts and some of their properties are difficult to predict; however, their spatial response varies during the aperture time due to their non-permanent scattering regime and anisotropy. The spatial information provided by the SAR operation can be extracted with a multisquint processing mode [110], similar to digital beamforming [111]. This mode provides a set of images, or squints, where each individual squint is formed with a set of echoes backscattered from a certain direction of arrival. Since the squints do not have the highest resolution and are not artifact-free, single-looks are still required to compute changes at nominal resolution. We propose a three-stage change detector that combines the advantages of single-look and multisquint SAR processing modes to reduce false alarms caused by image artifacts while providing detection rates similar to those obtained when only exploiting single-look processing. The main idea is based on deriving a new pair of images where artifacts do not appear in the same image pixels as those of their corresponding single-looks. This permits the identification of associated false alarms and their removal *a posteriori* from the change map of the single-looks. The new pair of images is formed using a so-called MultiSquint Framework (MSF), where multiple squints are combined and filtered. The MSF is designed so that the azimuth resolution and SNR of the resulting pair are sufficient to still detect changes of interest. The proposed approach takes advantage of the SAR processing chain without significantly increasing computation time. It is modular and can include additional object features, such as shape information. It has lower sensitivity to errors caused by differences between acquisition geometries, and change detection in urban areas can benefit from the proposed method since sidelobes and moving targets are typically present in those scenarios. The approach was applied to detect changes caused by human activity at an airport, and evaluated using single channel SAR images.

The paper is organized as follows: Section 3.2 introduces the advantages and drawbacks offered by the different SAR processing modes, and their suitability for reducing errors caused by artifacts. We then describe the different stages of the proposed method, emphasizing the MSF and corresponding adaptions. Section 3.3 illustrates the results obtained using multitemporal

high resolution airborne SAR imagery acquired in typical urban scenarios. Finally, section 3.4 concludes with a discussion of the results and conclusions.

3.2 Method

The proposed change detector consists of three stages. In the first stage an Initial Change Map (ICM) is derived from single-looks so that changes are detected at the highest attainable resolution. In the second stage, we derive a new pair of images using a multisquint processing mode, where targets are filtered according to their spatial response. An additional change map CM_{MS} is computed from these new pair of images. Finally, we perform fusion of the change maps to remove false alarms caused by artifacts. Fig. 3.1 shows a simplified scheme of the method. In the following we describe in detail each corresponding stage, providing also insight into the SAR processing chain.

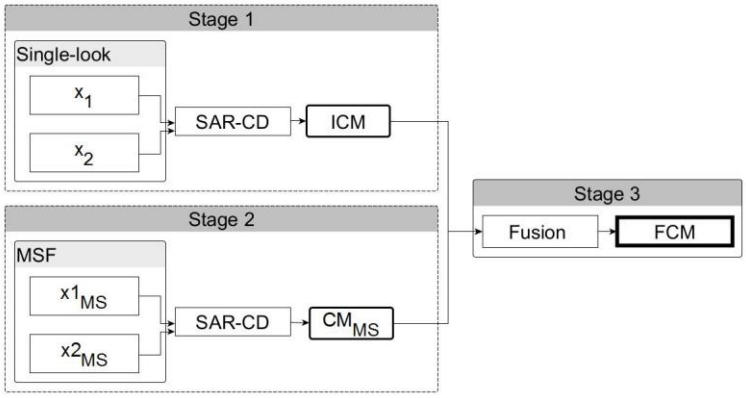

Fig. 3.1 Three-stage SAR image change detector.

The proposed change detector consists of three stages. In the first stage an Initial Change Map (ICM) is derived from single-looks so that changes are detected at the highest attainable resolution. In the second stage, we derive a new pair of images using a multisquint processing mode, where targets are filtered according to their spatial response. An additional change map CM_{MS} is computed from these new pair of images. Finally, we perform fusion of the change maps to remove false alarms caused by artifacts. Fig. 3.1 shows a simplified scheme of the method. In the following we describe in detail each corresponding stage, providing also insight into the SAR processing chain.

3.2.2 Change detection and processing chain

Typically, single-channel SAR image Change Detection (SAR-CD) is performed by applying a dissimilarity function f to a reference image x_1 and a test image x_2 [23]. For multichannel SAR, the dissimilarity function instead exploits data cubes or the corresponding covariance matrices [50-52]. To mitigate errors caused by noise, image restoration techniques, such as denoising, are applied to $f(x_1, x_2)$ [24, 25]. A change map is derived by thresholding or classifying the corresponding restored image [3].

In this work, we follow an approach similar to that described in [112], referred to as CD-MCA. This method includes three steps. First, the Difference Image (DI) is derived by subtracting the log-transformed data of the input image pair; i.e. $DI = x_2 - x_1$. Second, the DI is denoised and decomposed into two images describing shape features using wavelet- and curvelet-based Morphological Components Analysis (MCA) [26, 74]. The output of the MCA can be expressed as follows:

$$DI_{MCA} = DI_{WAV} + DI_{CURV} \tag{3.1}$$

where DI_{WAV} and DI_{CURV} are the denoised images attached to the wavelet and curvelet components respectively, and DI_{MCA} the denoised version of the DI. By using MCA, the DI is assumed to be a combination of smooth areas (fields, pastures, roads, water bodies…), point like targets, blob-like structures (cars, trucks…), and lines (walls, roof edges…). The curvelet domain is suitable for representing lines, while the rest of the shapes are better represented by the wavelet domain. Third, the change map is computed after thresholding DI_{MCA}. Unless the opposite is indicated, thresholding is performed automatically via Expectation Maximization (EM) assuming a Gaussian distribution as described in [3]. In this work, the change maps have three classes: no-change, backscatter decrease, and backscatter increase.

3.2.3 The multisquint mode

The previous sequence of steps neglected relevant sources of errors, for example those caused by image artifacts such as: a) range and azimuth side-lobes induced by matched filtering [63], b) moving targets, c) clutter, d) nadir, range, and azimuth ambiguities caused by system design constraints and image reconstruction errors [104, 113], and e) multipath ghosts [114]. Artifacts and some of their properties are difficult to predict, but many of them can be characterized by their non-permanent scattering regime; i.e. their spatial response varies during illumination.

Omitting calibration factors and signal weightings, a pixel or backscattering element of a geocoded single-look band-pass SAR image x is focused by means of the Time Domain Back-Projection method [65] with:

$$x(E_0, N_0) = \sum_{\tau=\tau_1}^{\tau_2} s\left(\frac{2R_s}{c}, \tau\right) \tag{3.2}$$

where $R_s = \sqrt{(X(\tau) - x_0)^2 + (Y(\tau) - y_0)^2 + (Z(\tau) - z_0)^2}$ is the slant range, and (E_0, N_0) the map coordinates of the element, which are transformed to the equivalent global Cartesian coordinates (x_0, y_0, z_0) using a Digital Elevation Model (DEM). $\big(X(\tau), Y(\tau), Z(\tau)\big)$ is the sensor position in global Cartesian coordinates at slow time τ, $L = \tau_2 - \tau_1$ the aperture length, ζ the base-band conversion factor, c the speed of light, and s the band-pass range compressed signals.

The expression in (3.2) does not provide spectral, temporal and spatial information of the targets that are, in other words, naturally collected by the SAR operation. Let us express (3.2) as follows:

$$\dot{x}(E_0, N_0, W(t, \tau)) = \sum_{\tau=\tau_1}^{\tau_2} s(t, \tau) \cdot W(t, \tau) \tag{3.3}$$

where W is a user-defined weighting function and $t = 2R_s/c$ is the fast time. If W is a weighting function in τ, $\dot{x}(E_0, N_0, \tau)$ provides both temporal and spatial information, because the illumination conditions at (E_0, N_0) vary with slow time τ. This relation implies that the azimuth resolution of an image $\dot{x}$ focused with a subset of pulses $W(\tau)$ varies with (E_0, N_0), and as an additional consequence, the image can suffer from border artifacts. A more suitable solution is obtained when W is a spatial filter or beamforming function [111]; i.e. the range bins of the different pulses are filtered depending on a specific direction of arrival. This processing mode, referred to as multisquint [110], is described by:

$$\ddot{x}(E_0, N_0, \Delta\theta) = \sum_{\tau=\tau_1}^{\tau_2} s(t, \tau) \cdot W(\Delta\theta) \tag{3.4}$$

where $\Delta\theta$ is a fraction of the azimuth beamwidth θ_a of the antenna pattern in reception, and the corresponding image $\ddot{x}$ is referred here to as a *squint*. The azimuth resolution of a squint $\ddot{x}$ de-

pends on $\Delta\theta$; i.e. information of the spatial response is retrieved at the cost of a degraded azimuth resolution. Moreover, sparsification of the signals $\ddot{x}$ caused by $W(\Delta\theta)$ increases the strength of the azimuth side-lobes in comparison to those of the single-look x.

The spatial response of artifacts can be collected with a set of squints $\{\ddot{x}(\Delta\theta)\}$ by using (3.4). This set is obtained by sampling the space of the azimuth angle θ with the beamforming function W. Sampling the θ domain can be performed by focusing a 2-dyadic M-stage resolution sequence of squints, using $\Delta\theta_{\mathrm{m}} = \Delta\theta_{\mathrm{m}-1}/2^{\mathrm{m}}$, and $\Delta\theta_0 = \theta_{\mathrm{a}}$ at scale m. The mth-scale is composed of $\mathrm{N} = \theta_{\mathrm{a}}/\Delta\theta_{\mathrm{m}} = 2^m$ squints. Here, W takes the form of a *rect* function in the region $[-\theta_a/2, \theta_a/2]$, assuming that the azimuth antenna gain pattern is symmetric with respect to its maximum. The nth-squint at the mth-resolution scale is focused via:

$$\ddot{x}(E_0, N_0, \mathrm{m}, \mathrm{n}) = \sum_{\tau} s(t, \tau) \cdot W(\mathrm{m}, n) \tag{3.5}$$

and

$$W(\mathrm{m}, \mathrm{n}) = \begin{cases} 1, & {}^{-\theta_a}/_2 + \Delta\theta_m \cdot (n-1) \le \theta \le {}^{-\theta_a}/_2 + \Delta\theta_m \cdot n \\ 0, & otherwise \end{cases} \tag{3.6}$$

where the azimuth angle θ is computed with the antenna pointing vector and the position of the backscattering element (E_0, N_0) at slow time τ. By applying (3.5) we obtain a preliminary set of squints $\{\ddot{x}(\Delta\theta_{\mathrm{m}})\}$ as shown in Fig. 3.2, where each $\ddot{x}_{mn}$ is a squint, $\ddot{x}_{01} = x$ is the single-look, and the size of each box is proportional to $\Delta\theta_m$. Since for a fixed m, $\sum_{n=1}^{N} \ddot{x}_{mn} = \ddot{x}_{01}$, the computational efficiency without memory constraints is identical to that of the single-look complex; i.e. one needs to focus the squints of the last scale $m = M$, because the squints of the previous scales can be obtained by complex-valued additions: e.g. $\ddot{x}_{21} \simeq \ddot{x}_{31} + \ddot{x}_{32}$. Notice that the squints at scale m do not overlap in the θ domain.

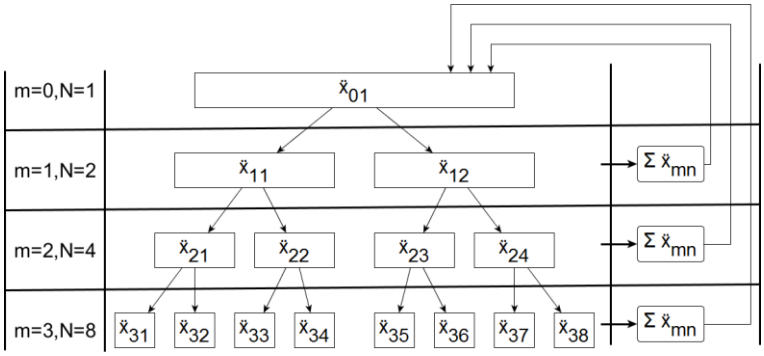

Fig. 3.2 Multisquint set $\{\ddot{x}(\Delta\theta_{\mathrm{m}})\}$ computed with M=4 resolution scales. Squints have different azimuth resolution and SNR losses.

The set $\{\ddot{x}(\Delta\theta)\}$ is formed by combining via complex-valued additions the squints in $\{\ddot{x}(\Delta\theta_{\mathrm{m}})\}$ at scale m to guarantee that the azimuth resolution and SNR loss is constant with m; i.e. $\Delta\theta_{m=1\ldots M} = \Delta\theta$, and ensure that the resulting images have enough resolution to detect the smallest changes of interest. In this study, the azimuth resolution of all images in the set $\{\ddot{x}(\Delta\theta)\}$ is $2\delta_a$, with δ_a being the azimuth resolution of a single-look. This procedure is shown in Fig. 3.3 for $\Delta\theta_{m=1..M} = \theta_a/2$, yielding $\binom{N}{2^{m-1}}$ images per scale. Finally, artifacts can be filtered by applying a *min* operator to the log-transformed and radiometric calibrated $\binom{N}{2^{m-1}}$ images in $\{\ddot{x}(\Delta\theta)\}$ at scale m, yielding one image X_{MS} per scale: $\{X_{MS}(m)\}_{m=1\ldots M}$. In this manner, the artifacts of the single-look do not completely overlap those of the images in $\{X_{MS}(m)\}_{m=1\ldots M}$.

In $\{X_{MS}(m)\}$, lower scales (i.e. small m) provide less information on the spatial behavior of the targets, since the sampling of the θ domain is coarser. On the contrary, higher scales contain repetitive information since $X_{MS}(m-1) \subset X_{MS}(m)$. This implies that to preserve high detection rates, information from higher scales is required; achieved however, at the cost of moderate false alarm rates. One selects the highest possible resolution scale m based on memory constraints and computational efficiency requirements. The computational complexity of single-look processing by means of a serial back-projection is proportional to $I_x \times I_y \times L$, being $I_x \times I_y$ the size of the image and L the number of pulses [82]. If the $N = 2^m$ squints at resolution scale m do not overlap in the θ domain, then the computational complexity of the corresponding multisquint processing is proportional to $(N/P) \times I_x \times I_y \times L$, with P being the number of squints that can be simultaneously allocated in memory.

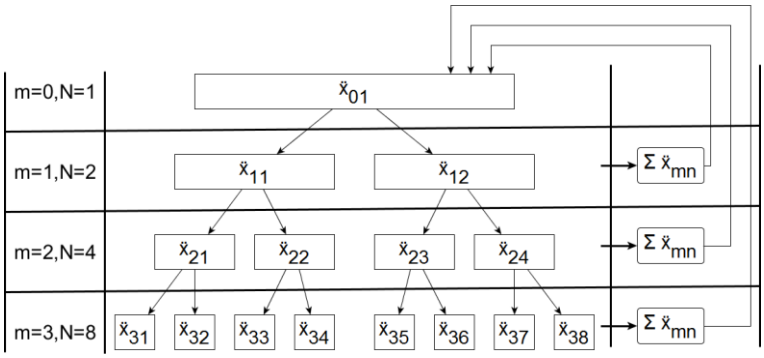

Fig. 3.3 Multisquint set $\{\ddot{x}(\Delta\theta)\}$ computed with M=4 resolution scales. All squints have identical azimuth resolution and SNR loss.

The key concept of the proposed multisquint framework is visualized in Fig. 3.4, where the spatial response of common artifacts and a static object (a single car) are illustrated using images from the set $\{\ddot{x}(\Delta\theta_m)\}$. A pair of single-look images is shown on the top. The RGB composites in the middle are obtained with the corresponding single-look image (blue) and the pair of associated squints $\ddot{x}_{31}$ (red) and $\ddot{x}_{38}$ (green). These images show degradation in resolution of the squints $\ddot{x}_{31}$ and $\ddot{x}_{38}$ and an increase of the azimuth side-lobes due to signal sparsification. The artifacts rotate throughout the multisquint set (ambiguities and side-lobes), or are only present in some sections of the θ domain (artifact 1 and 2). In contrast, the single car shows a permanent scattering regime. The RG(B=0) composites at the bottom, obtained with $R = x_{01}$, and $G = min(x_{31}, x_{38})$, show that the artifacts of the single-look and the squints do not overlap, but the targets with a permanent scattering regime do overlap.

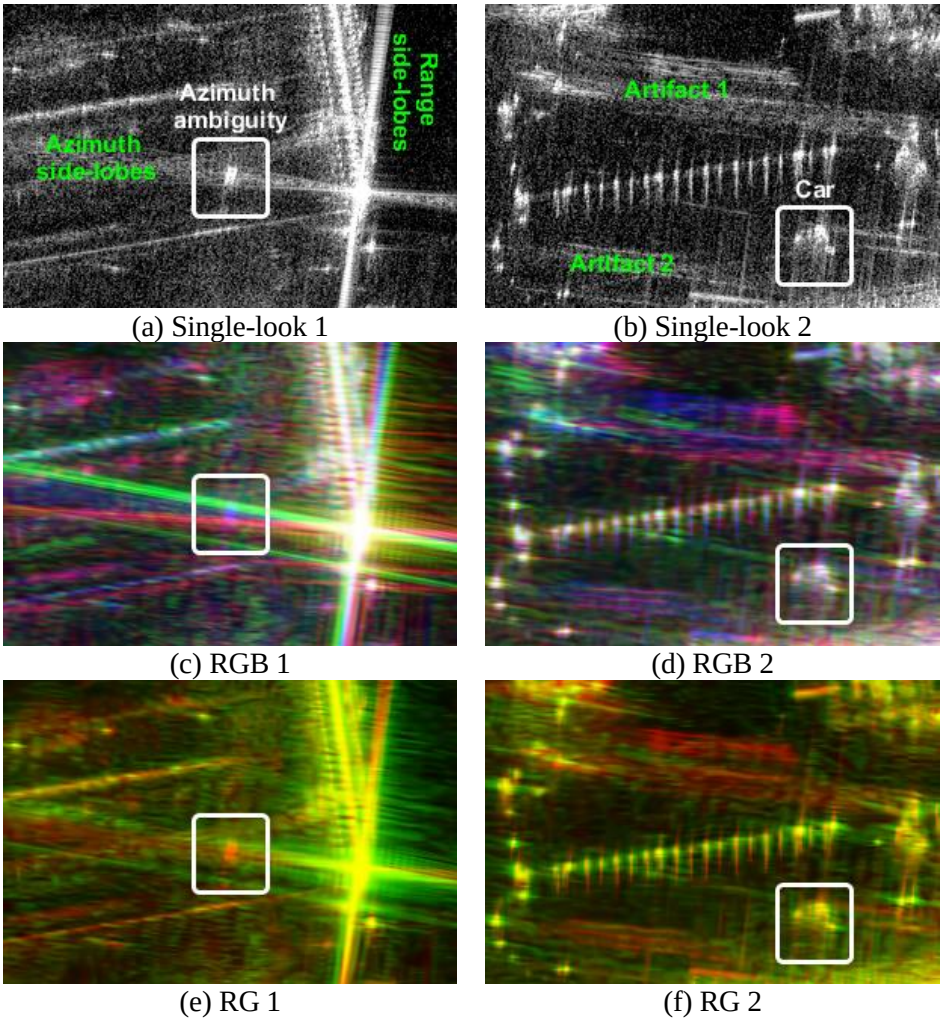

(a) Single-look 1 (b) Single-look 2

(c) RGB 1 (d) RGB 2

(e) RG 1 (f) RG 2

Fig. 3.4 Single-look and multisquint processing modes comparison. (a-b) patches of single look images x_{01}. (c-d) RGB composites $R = x_{31}, G = x_{38}, B = x_{01}$. (e-f) RG composite $R = x_{01}, G = min(x_{31}, x_{38}), B = 0$.

3.2.4 Multisquint framework for SAR-CD

The combination of advantages offered by single-look (high SNR and resolution) and multisquint processing (spatial behavior of the targets) modes for SAR-CD leads to a multi-stage approach; i.e. if only single-look images are used, the change map has false alarms due to artifacts, and if the reduced set $\{X_{MS}(m)\}_{m=1\ldots M}$ are exploited instead, changes are detected at a lower resolution scale.

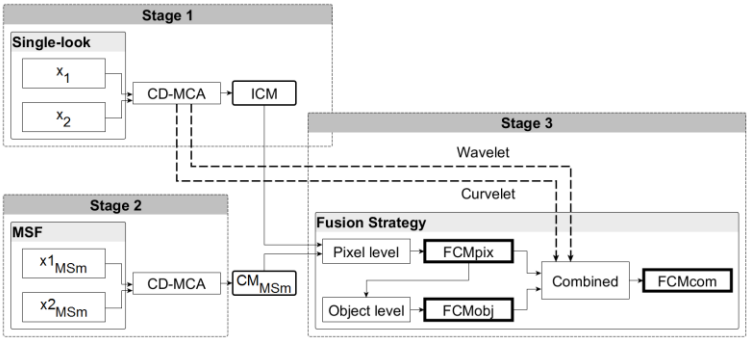

Fig. 3.5 Three-stage change detector approach.

The detailed architecture of the proposed three-stage method is shown in Fig. 3.5. The ICM is derived from the single-looks in the first stage by using CD-MCA. In the second stage, CD-MCA is applied to the pair $X_{1MS}(m)$ and $X_{2MS}(m)$ obtained by means of the MSF. The resulting change map is here referred to as $\mathrm{CM}_{\mathrm{MS\{m\}}}$, where m is the resolution scale in use. Notice that the *min* operator used to compute $X_{MS}(m)$ does not introduce additional parameters; i.e. the thresholding scheme used to derive the ICM can be re-utilized, since the dynamic range of DI_{MCA} is similar to that of $DI_{MS(m)-MCA}$, with $DI_{MS(m)-MCA}$ being the sum of the denoised morphological components of $\left(X_{2MS}(m) - X_{1MS}(m)\right)$. Furthermore, the *min* operator is computationally efficient.

Once the ICM and the $\mathrm{CM}_{\mathrm{MS\{m\}}}$ are derived, a Final Change Map (FCM) is computed by fusing the classes of the two previous change maps. The unchanged class is labelled with 0's while the backscatter increase and backscatter decrease classes use different labels. In order to consider the spatial information provided by $\mathrm{CM}_{\mathrm{MS\{m\}}}$ we can adopt three different fusion strategies: 1) fusion at the pixel level, 2) fusion at the object level, and 3) a combination of the two previous.

Fusion at the pixel level is performed for each change class via:

$$FCM_{pix}(i,j) = \begin{cases} ICM(i,j), & if\ ICM(i,j) = CM_{MS\{m\}}(i,j) \\ 0, & otherwise \end{cases} \tag{3.7}$$

where (i,j) denotes the pixel coordinate indices. This strategy preserves the classes of the pixels of the ICM that are identically labelled in $\mathrm{CM}_{\mathrm{MS\{m\}}}$, while reassigning the rest to the unchanged class (labelled here with 0's). It assumes that the pixels of the changes caused by artifacts have different labels in ICM and $\mathrm{CM}_{\mathrm{MS\{m\}}}$, and thus FCM_{pix} does not inherit the associated false alarms. This strategy is computationally efficient and does not require additional setting parameters. A drawback is that fusion at the pixel level can introduce undesired holes in the corresponding change objects: some pixels of the change objects could be reassigned to the unchanged class.

By defining a change object $\{c\}$ as an 8-connected set of pixels of a change class (backscatter increase, or backscatter decrease) with interior holes, fusion at the object level can be performed by examining each individual change object of the ICM as follows:

$$FCM_{obj}\{c\} = \begin{cases} \{c\}, & if \sum_{i,j} \left(ICM(i_c,j_c) = CM_{MS\{m\}}(i_c,j_c)\right)/n_c \geq F_{ov} \\ 0, & otherwise \end{cases} \tag{3.8}$$

where (i_c, j_c) denotes the pixels of the change object {c} and n_c the number of pixels in {c}. From (3.8), a change object {c} is preserved if a fraction F_{ov} of its pixels are identically labelled in $\mathrm{CM}_{\mathrm{MS\{m\}}}$, otherwise the change object is reassigned to the unchanged class (labelled with 0's). The overlapping factor F_{ov} takes values from 0 to 1. $F_{ov} = 0$ indicates that {c} is not present in $\mathrm{CM}_{\mathrm{MS\{m\}}}$, and $F_{ov} = 1$ that it is entirely present in $\mathrm{CM}_{\mathrm{MS\{m\}}}$. This strategy is based on the assumption that the change objects of the ICM caused by artifacts scarcely intersect with those of $\mathrm{CM}_{\mathrm{MS\{m\}}}$. Only the change objects of the ICM that are caused by targets with a permanent scattering regime will be transferred to FCM_{obj}. In contrast to the foregoing, fusion at the object level can cause a complete cancellation of changes, and is computationally less efficient. In addition, it utilizes the setting parameter F_{ov}, which in practice might be unknown a priori.

A trade-off between the two previous strategies requires additional assumptions or *a priori* knowledge about the potential changes. If a change object fulfills (3.8); i.e. it is retained, and has attached side-lobes, a combined strategy can be used. After fusing at the object level, a shape-driven pixel level fusion can be performed by assuming that side-lobes are better represented in the curvelet domain due to their linear shape. The pixels of a change object $\{c\}$ are labelled according to:

$$FCM_{com}\{c(i_c,j_c)\} = \begin{cases} c(i_c,j_c), & if\ DI_{WAV}(i_c,j_c) > DI_{CURV}(i_c,j_c) \\ 0, & otherwise \end{cases} \quad (3.9)$$

where (i_c, j_c) are the pixels of the change object {c} in FCM_{obj}, and DI_{WAV} and DI_{CURV} are the wavelet and curvelet components of the DI derived from (3.1). By using the combined strategy, we first discard change objects and then label the individual pixels of retained ones based on additional features, like shape information. This strategy can reduce the presence of holes in some change objects and also avoid complete cancellation of changes with a particular shape.

3.3 Experimental Results

3.3.1 Data and Test Sites

The data sets tested were acquired with DLR's F-SAR sensor [28] over the *Allgäu* airport in Memmingen (Germany). The SAR images were recorded at X-band in a linear stripmap configuration. The slant range resolution δ_r, azimuth resolution δ_a, incidence angle at mid-range θ_{inc}, and flight path heading ϕ of the data takes are listed in Table 3.1. The azimuth beamwidth θ_a of the antenna gain pattern was approximately 7.2°. All images were the result of the single-look focusing of the horizontal co-polarized channel after relative radiometric calibration. The images were focused with a Graphic Processor Unit-based Time Domain Back-Projection processor [115].

TABLE 3.1
DESCRIPTION OF THE USED F-SAR DATA SETS

Data	$\boldsymbol{\delta_r}$	$\boldsymbol{\delta_a}$	$\boldsymbol{\theta_{inc}}$	$\boldsymbol{\phi}$	**Date**	**Time**
MEM 1	0.22m	0.14m	52°	280°	17th/10/2013	12:13:09
MEM 2				282°	17th/10/2013	12:36:05
MEM 3				274°	25th/10/2013	12:48:32

The images from data sets MEM1 and MEM2 (see Table 3.1) were acquired under windy and rainy conditions, whereas the image from data set MEM 3 was acquired under more stable weather conditions.

3.3.2 Numerical Evaluation

Numerical evaluation was performed by labelling a ground truth based on aerial photos and ground information recorded simultaneously with the SAR data acquisitions. This information was available for the pair MEM1-MEM2, described in Table 3.1. The quality assessment was based on typical indicators used in change detection [116]: the overall classification error ε, the kappa coefficient κ, the false alarm rate FA, and the detection rate PD. The classification error represents the number of samples that were wrongly classified; it depends on the sum of the misdetection and false alarm rates. If the number of changes is small, optimization of this indicator tends to produce change maps with low detection rates; i.e. in some cases the best result is the null solution. To avoid this, κ is also computed. Its possible values range from 0 to 1, and the higher its value the better the classification result. In contrast to ε, κ depends on the false alarms and misdetections instead of their sum, avoiding potential convergence to the null solution.

The quality indicators were computed from the ICM and FCM using the reference ground truth. Performance was studied with the ratio of the indicators $\varepsilon_r = \varepsilon_{ICM}/\varepsilon_{FCM}$, $FA_r = FA_{ICM}/FA_{FCM}$, $PD_r = PD_{FCM}/PD_{ICM}$, and $\kappa_r = \kappa_{FCM}/\kappa_{ICM}$. The evaluation criterion was based on the improvements obtained with three out of the previous four indicators. In general, it

is expected that $\kappa_r > 1$, $\varepsilon_r > 1$, $FA_r > 1$, and $PD_r \approx 1$. As an additional evaluation criterion, we optimized the value of κ by deriving the change maps with an iterative thresholding approach using a pair of thresholds [T_1,T_2], and a step size of ±0.2 dB. The value of T_1 and T_2 provide the backscatter decrease class and the backscatter increase class, respectively. The threshold T_1 is always negative and T_2 positive.

For automatic thresholding, EM was iterated until convergence and initialized with a change map derived by thresholding the input with [-3,3] dB. The value of -3 and 3 dB provided a first estimate of the backscatter decrease class and backscatter increase class, respectively. The use of the initial [-3,3] dB thresholds was based on the idea that a point target causing a change is resolvable, assuming that the resolution of a point target corresponds to the -3 dB width of the main lobe of its point spread function.

If a fusion strategy requires additional parameters, the quality indicators are exploited to obtain optimal values. The optimal value of F_{ov} is derived by iteratively performing change detection and evaluating the quality indicators of the corresponding change maps. During this procedure, the values of F_{ov} range from 0.1 to 0.9 using a step size of 0.1. Notice that in practice and for unsupervised change detection it is required to assume or have *a priori* knowledge of F_{ov}.

For comparison purposes we analyzed the performance of diverse methods reported in the literature: 1) CD-LRT, it is based on the likelihood ratio test in [50], 2) CD-GKLD_{WAV}, it models the statistical properties of the wavelet coefficients of the SAR images [42-44]; we assume that the wavelet coefficients can be modelled with a Gaussian distribution, 3) CD-GLR, it was reported in [34], and is based on the guided image filtering method described in [117], and 4) the method based on principal component analysis described in [75], referred here to as CD-PCAk.

To isolate potential errors caused by automatic thresholding, we derive the change maps that provide the best κ coefficient by iterative thresholding and numerical evaluation of the generated maps. During this iterative procedure, the values of the thresholds were obtained by sweeping the dynamic range of the input image utilized for thresholding.

3.3.3 Results

The data sets listed in Table 3.1 were used to evaluate the performance of the proposed method. Fig. 3.6 shows in the center a patch of the area of interest using a denoised RG(B=0) composite with the pair of the shortest temporal baseline MEM1-MEM2. The patch illustrates the terminal of the airport, parking lots, nearby buildings and trees. The RG composite was formed with the reference image MEM1 in the red channel and the test image MEM2 in the green channel. The RG images were denoised with Color Block-Matching 3-D, described in [35], intended to give the viewer an indication of potential changes; i.e., the changes with a higher likelihood of occurrence are highlighted in red and green, whereas yellow indicates a low probability of change. In Fig. 3.6, changes indicated by white rectangles were identified based on aerial photos and ground information. Some examples of the photos are included to the side of the RG image, showing changes caused by static cars.

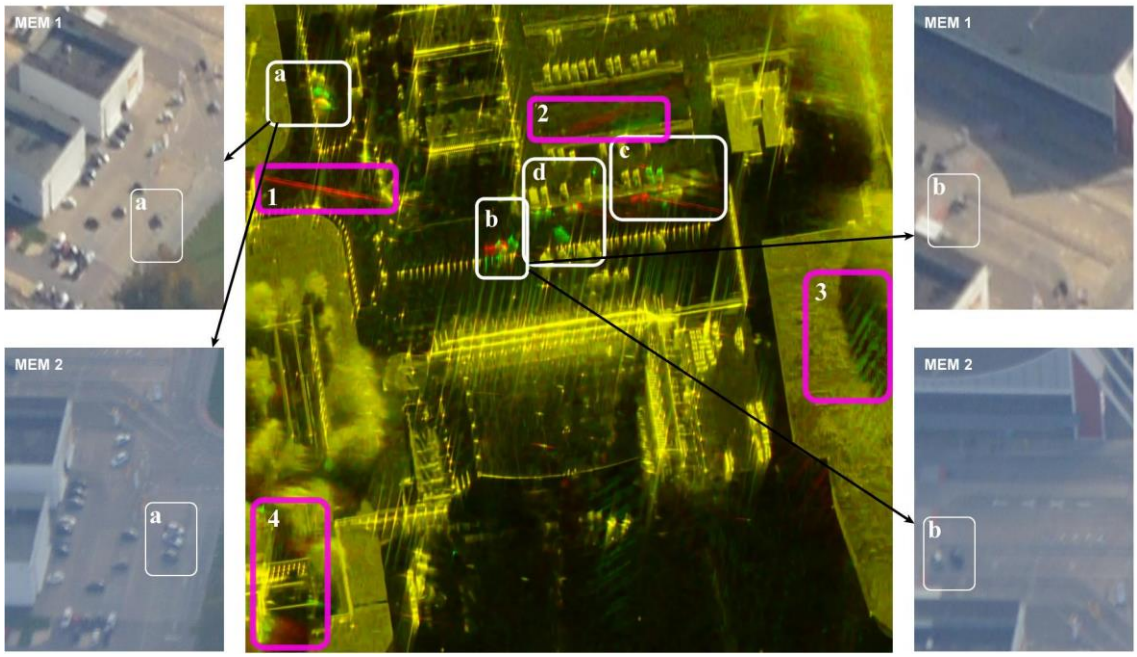

Fig. 3.6 Center: RG composite of the area of interest, computed from the image pair MEM1-MEM2. White rectangles: real changes. Magenta rectangles: areas with false alarms. Aerial photos on (Right and Left) show some of the corresponding changes labeled for the ground truth.

TABLE 3.2
PERFORMANCE METRICS FOR THE PAIR MEM1-MEM2 FOR DIFFERENT FUSION STRATEGIES

m	**Change Map**	F_{ov}	κ_r	PD_r	FA_r	ε_r
1	FCM_{pix}	N/A	2.3644	0.8775	5.8095	4.1161
	FCM_{obj}	0.4	2.6972	0.9448	7.4840	5.0248
	FCM_{com}	0.4	2.7023	0.9448	7.4341	5.0460
2	FCM_{pix}	N/A	2.3326	0.9512	4.7247	3.7008
	FCM_{obj}	0.2	2.6514	0.9311	7.2643	4.9084
	FCM_{com}	0.2	2.6551	0.9311	7.3000	4.9236
3	FCM_{pix}	N/A	2.2953	0.9688	4.3743	3.5244
	FCM_{obj}	0.2	2.6021	0.9504	6.4913	4.6184
	FCM_{com}	0.2	2.6033	0.9504	6.5007	4.6229
4	FCM_{pix}	N/A	2.1074	0.9848	3.4762	2.9692
	FCM_{obj}	0.2	2.5191	0.9920	5.3457	4.1339
	FCM_{com}	0.2	2.5202	0.9920	5.3522	4.1375

After applying the proposed method, ε_r, κ_r, PD_r, and FA_r were computed for the patch shown in Fig. 3.6. Table 3.2 lists the quality indicators of the change maps derived after applying automatic thresholding via EM and the different fusion strategies. The indicators κ_r, ε_r, and FA_r showed that the performance of the method degraded slightly by increasing *m*, with PD_r tending towards one. When applying fusion at the object level with the combined strategy, the value of the overlapping factor F_{ov} was optimized as described in section 3.2.4. In those cases, for increased *m*, better κ_r and ε_r were obtained with lower values of F_{ov}.

Table 3.3 presents the performance of the proposed method and the approaches utilized for comparison purposes. For CD-LRT we included the results derived when using single-look and multi-look.

TABLE 3.3
PERFORMANCE COMPARISON OF THE MSF WITH DIFFERENT CHANGE DETECTION METHODS FOR THE PAIR MEM1-MEM2

Method	κ	PD	FA	ε
Single-look + MSF fusion at pixel level	0.5971	56.3298	0.0577	0.1359
Single-look + MSF combined fusion strategy	0.6167	65.8511	0.0852	0.1463
CD-LRT single-look [50]	0.2388	23.1915	0.1256	0.2631
CD-LRT 81 looks [50]	0.4355	49.4149	0.1381	0.2286
CD-GKLD$_{WAV}$ [42-44]	0.3561	46.2766	0.2023	0.2982
CD-GLR [34]	0.2740	23.3511	0.0834	0.2207
CD-PCAk, block size 8×8 pixels [75]	0.4709	50.9043	0.1165	0.2043

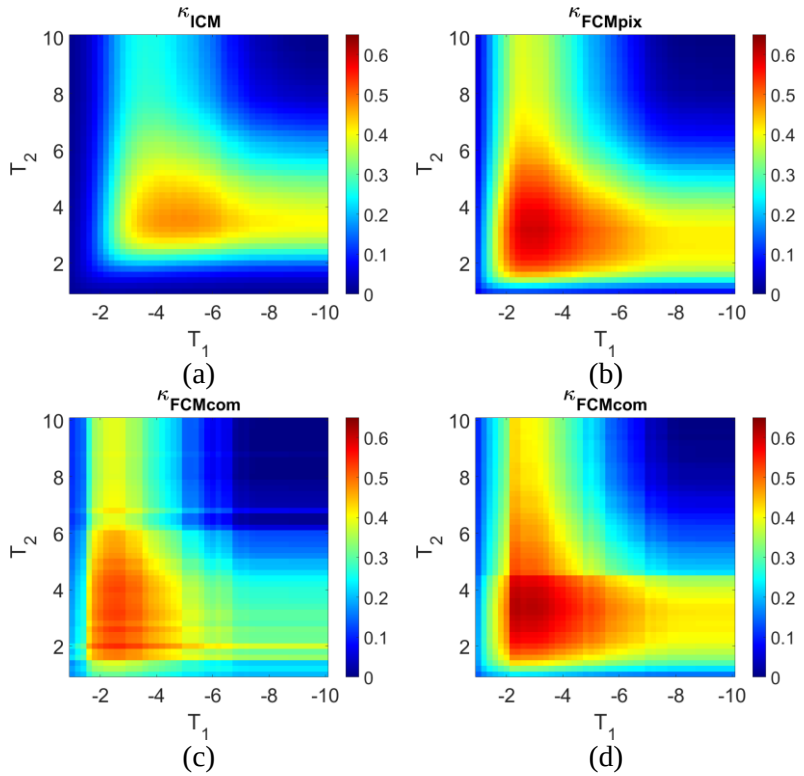

Fig. 3.7 Responses of κ computed from the image pair MEM1-MEM2 using iterative thresholding and m=2. (a) κ derived from the ICMs. (b) κ derived from the FCMs obtained using the fusion at pixel level strategy. (c-d) κ derived from the FCMs obtained using the combined fusion strategy and with F_{ov}=0.2 and F_{ov}=0.5 respectively.

Fig. 3.7 illustrates the kappa coefficient of the change maps derived by iteratively thresholding with sets [T_1,T_2]. The figure shows that the proposed method improved the value of κ when T_1 and T_2 were above -6 dB and below 6 dB respectively. Outside this interval, the value of κ degraded, as the detection rate decreased considerably. The best value of the overlapping factor F_{ov} was found to be 0.5 when performing iterative thresholding with the pair of thresholds [T_1,T_2].

Fig. 3.8 illustrates change maps obtained after applying the proposed method. The ICM have two classes: pixels marked in green/red indicate that targets entered or left the area of interest. The rest of the change maps have one additional class: pixels marked in blue indicate removed changes that were originally detected in the corresponding ICM. Fig. 3.8 (a) shows the overlaid ICM obtained from the image pair MEM1-MEM2, with real changes indicated by white rectangles and false alarms caused by artifacts or moving targets in magenta. The labels of the white rectangles correspond to those in Fig. 3.6. Fig. 3.8 (b) shows FCM_{com} overlaid on the reference image, computed with $F_{ov} = 0.2$, and $m = 2$ using automatic thresholding via EM. Comparison of the white rectangles shows the performance of the method. The removal of false alarms caused by artifacts (patches 1, 2 and 3) is indicated with magenta rectangles. Patch 4 contains some false alarms caused by the movement of the trees due to weather conditions. Note that the area indicated by rectangle *c* contains a side-lobe; its distortions were removed after applying the proposed method.

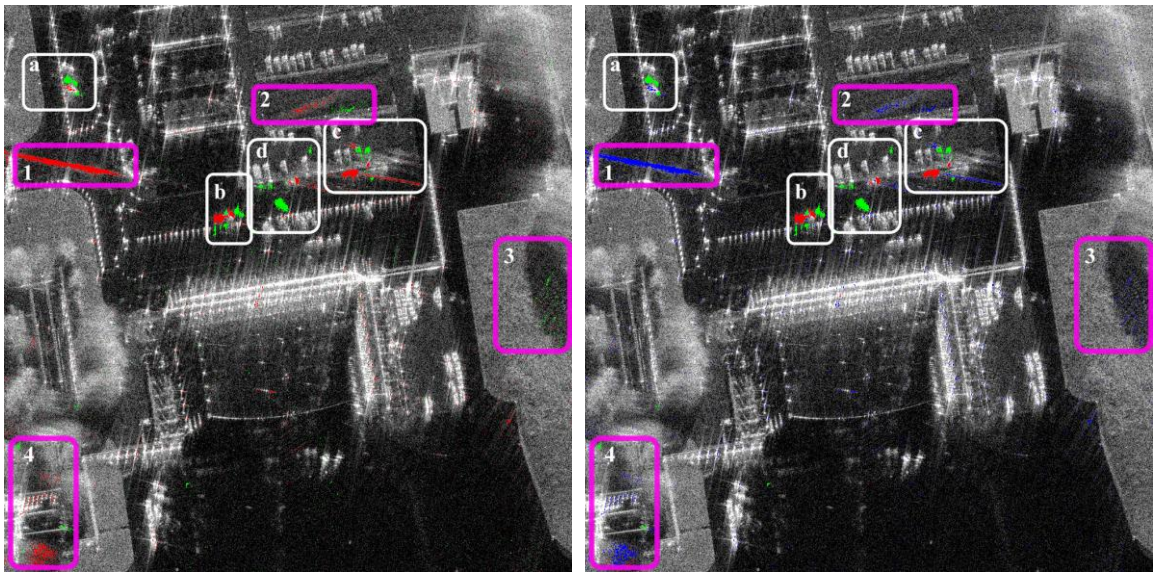

(a) (b)

Fig. 3.8 Change maps obtained with the pair MEM1-MEM2. Real changes are indicated by white rectangles, whereas false alarms by magenta. (a) ICM: pixels marked in green/red indicate that targets entered or left the area of interest. (b) FCM_{com}: pixels marked in blue indicate removed changes, originally detected in the ICM.

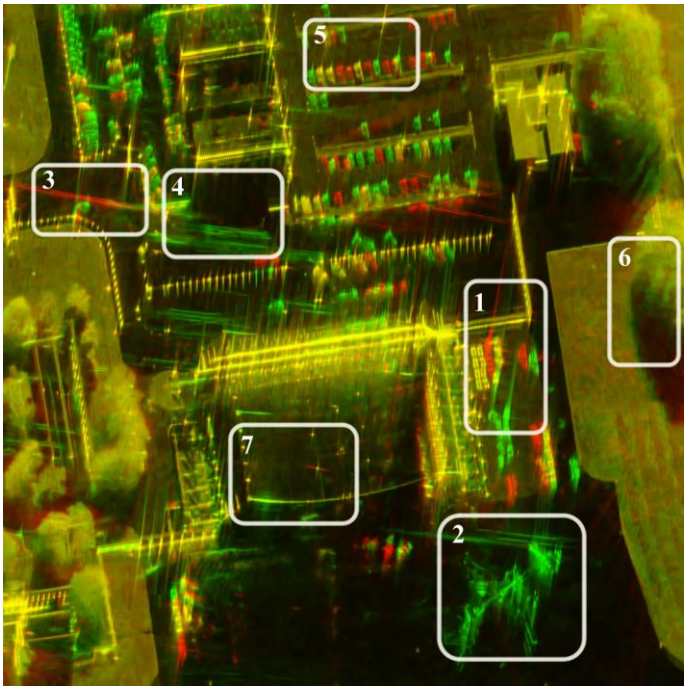

Fig. 3.9 RG composite of the area of interest, computed from the image pair MEM1-MEM3.

Results computed by using another combination of images are presented in the following. Fig. 3.9 shows the RG composite computed with the pair MEM1-MEM3. This pair provides a longer temporal baseline and thus contains many changes. Changes caused by luggage transporters and a civilian aircraft are marked in rectangles 1 and 2. Rectangles 3, 4 and 5 indicate changes caused by moving targets, some unidentified artifacts and static cars. Patches 6 and 7 contain changes caused by displacement of the shadowed areas induced by the slightly different acquisition geometries and the displacement of the point spread functions of the scatterers of the roof of the terminal respectively. Table 3.4 lists the quality indicators using automatic thresholding via EM and the different fusion strategies. Similar to the previous example, the responses of the quality indicators show that the performance of the method degraded with increasing m. For comparison purposes, Table 3.5 presents the performance of the different change detection methods.

TABLE 3.4
PERFORMANCE METRICS FOR THE PAIR MEM1-MEM3 FOR DIFFERENT FUSION STRATEGIES

m	**Change Map**	F_{ov}	κ_r	PD_r	FA_r	ε_r
1	FCM_{pix}	N/A	1.2198	0.8815	2.2015	1.6316
	FCM_{obj}	0.3	1.3030	0.9166	2.5219	1.8123
	FCM_{com}	0.3	1.3103	0.9065	2.6638	1.8549
2	FCM_{pix}	N/A	1.2363	0.9564	1.8757	1.5518
	FCM_{obj}	0.2	1.3143	0.9513	2.3477	1.7835
	FCM_{com}	0.2	1.3215	0.9472	2.4256	1.8134
3	FCM_{pix}	N/A	1.2286	0.9774	1.7482	1.5000
	FCM_{obj}	0.2	1.3034	0.9779	2.1158	1.7041
	FCM_{com}	0.2	1.3110	0.9758	2.1724	1.7305
4	FCM_{pix}	N/A	1.2197	0.9789	1.7044	1.4753
	FCM_{obj}	0.2	1.2916	0.9733	2.0755	1.6775
	FCM_{com}	0.2	1.2991	0.9714	2.1278	1.7023

TABLE 3.5
PERFORMANCE COMPARISON OF THE MSF WITH DIFFERENT CHANGE DETECTION METHODS FOR THE PAIR MEM1-MEM3

Method	κ	PD	FA	ε
Single-look + MSF fusion at pixel level	0.5770	63.9574	1.3787	2.2511
Single-look + MSF combined fusion strategy	0.5922	66.2195	1.3754	2.1910
CD-LRT single-look [50]	0.3702	36.3381	1.3528	2.921
CD-LRT 81 looks [50]	0.5374	60.8730	1.5600	2.5055
CD-GKLD$_{WAV}$ [42-44]	0.5194	66.2802	2.1178	2.9132
CD-GLR [34]	0.4342	49.4070	1.8150	3.0427
CD-PCAk, block size 8×8 pixels [75]	0.5370	60.6533	1.5494	2.5007

Fig. 3.10 illustrates the kappa coefficient as a function of [T_1,T_2], derived by iteratively evaluating the corresponding change maps. The value of κ improved when T_1 was above -5 dB and T_2 was below 5 dB approximately. The value of κ degraded outside this interval due to low detection rates.

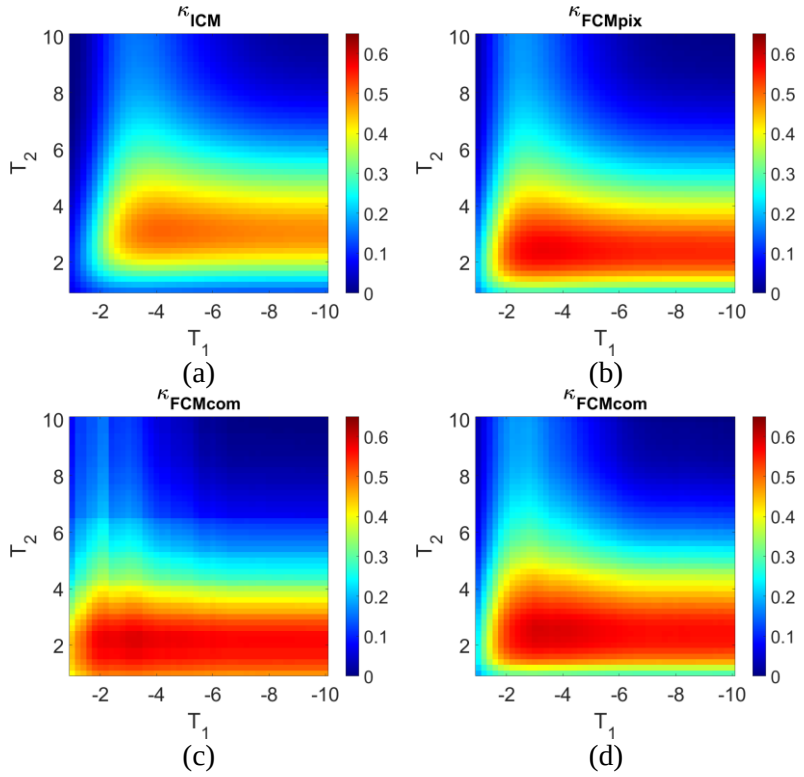

Fig. 3.10 Responses of κ computed from the image pair MEM1-MEM3 using iterative thresholding and m=2. (a) κ derived from the ICMs. (b) κ derived from the FCMs obtained using the fusion at pixel level strategy. (c-d) κ derived from the FCMs obtained using the combined fusion strategy and with F_{ov}=0.2 and F_{ov}=0.5 respectively.

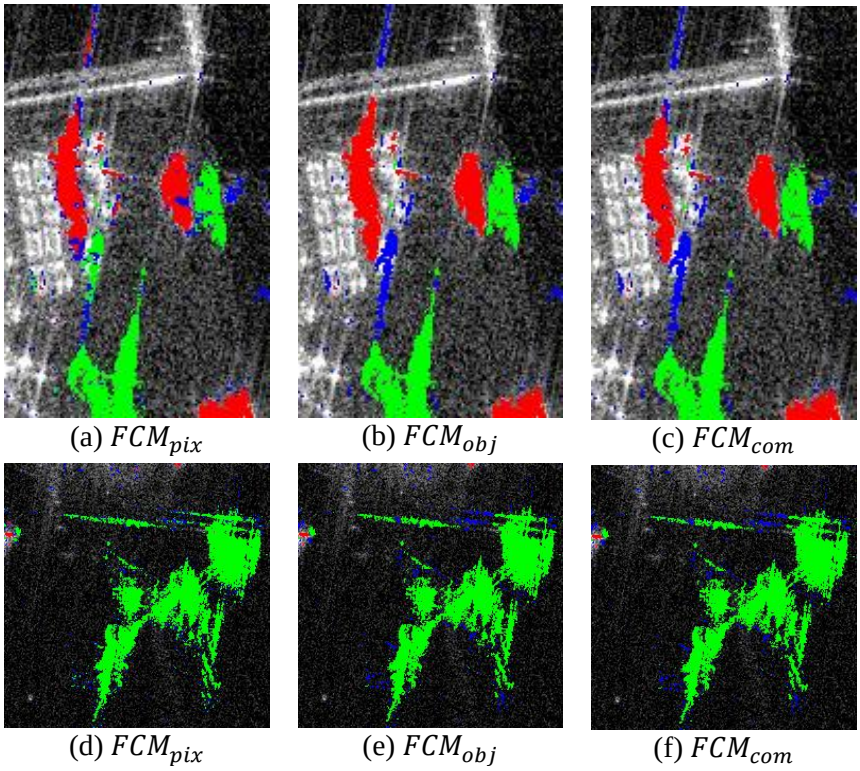

(a) FCM_{pix} (b) FCM_{obj} (c) FCM_{com}

(d) FCM_{pix} (e) FCM_{obj} (f) FCM_{com}

Fig. 3.11 Patches of change maps derived from the pair MEM1-MEM3 using different fusion strategies. (a-c) Change maps of the luggage transporters. (d-f) Change maps of the civilian aircraft.

Fig. 3.11 shows the change maps from patches 1 (luggage transporters) and 2 (aircraft) labelled in Fig. 3.9. The change maps were obtained with $m = 2$, and $F_{ov} = 0.2$ using automatic thresholding via EM. The performance achieved with each of the three different fusion strategies was observed when comparing the false alarms caused by the side-lobes and changes caused by the luggage transporters in patch 1. The change map FCM_{pix} had the highest number of remaining false alarms caused by side-lobes. The change map FCM_{obj} had false alarms caused by side-lobes attached to large targets, due to the constraint imposed by the overlapping factor F_{ov}. Depending on the complexity and shape of the change; the fusion strategy can play a minor role.

Fig. 3.12 shows the RG composites, ICMs and FCMs of patches 3 to 7 labelled in Fig. 3.9. Patch 3 shows the performance of the method to cancel false alarms caused by moving targets, and patch 4 when canceling false alarms caused by some unidentified artifacts. Patch 5 illustrates the performance of the method to detect changes caused by cars.

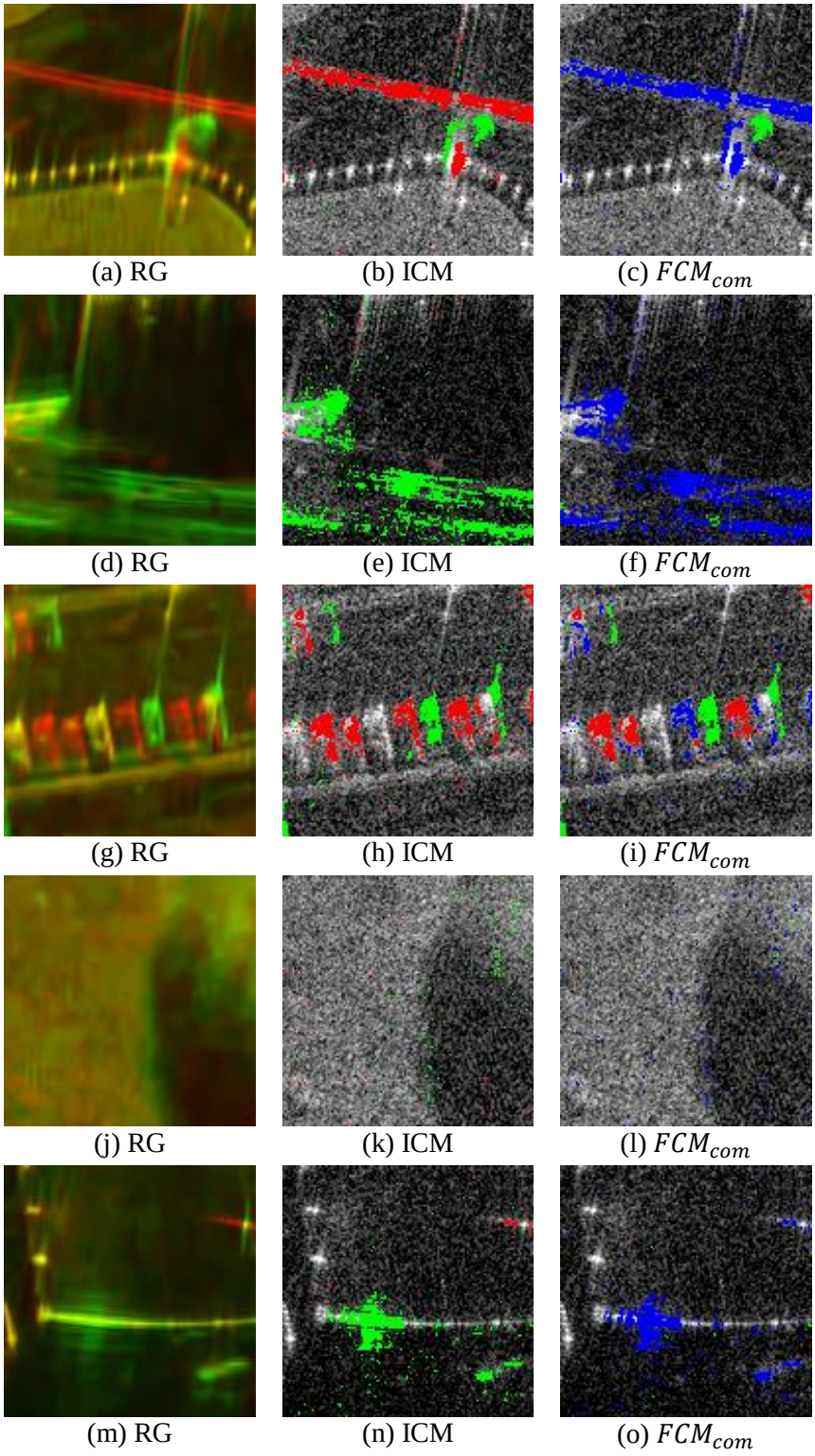

Fig. 3.12 RG composites and corresponding change maps derived from the pair MEM1-MEM3 under presence of image artifacts. (a-c) Patch 3. (d-f) Patch 4. (g-i) Patch 5. (j-l) Patch 6. (m-o) Patch 7.

For completeness, Fig. 3.13 shows the aerial photos, the corresponding RG composites and change maps from patches outside the area of interest. The performance of the method when removing false alarms caused by different types of artifacts is indicated. In Fig. 3.13 (b) one

observes a strong backscatter element causing large range sidelobes and azimuth ambiguities. Notice that the sidelobes did not overlap due to the slightly different acquisition geometries. Fig. 3.13 (e) shows the presence of a strong backscatter on the roof-edge of a building, causing also large range sidelobes, and azimuth ambiguities. Clutter was also present along the roof. Fig. 3.13 (h) shows glare artifacts on the roof of a building and includes some false alarms caused by the movement of the trees.

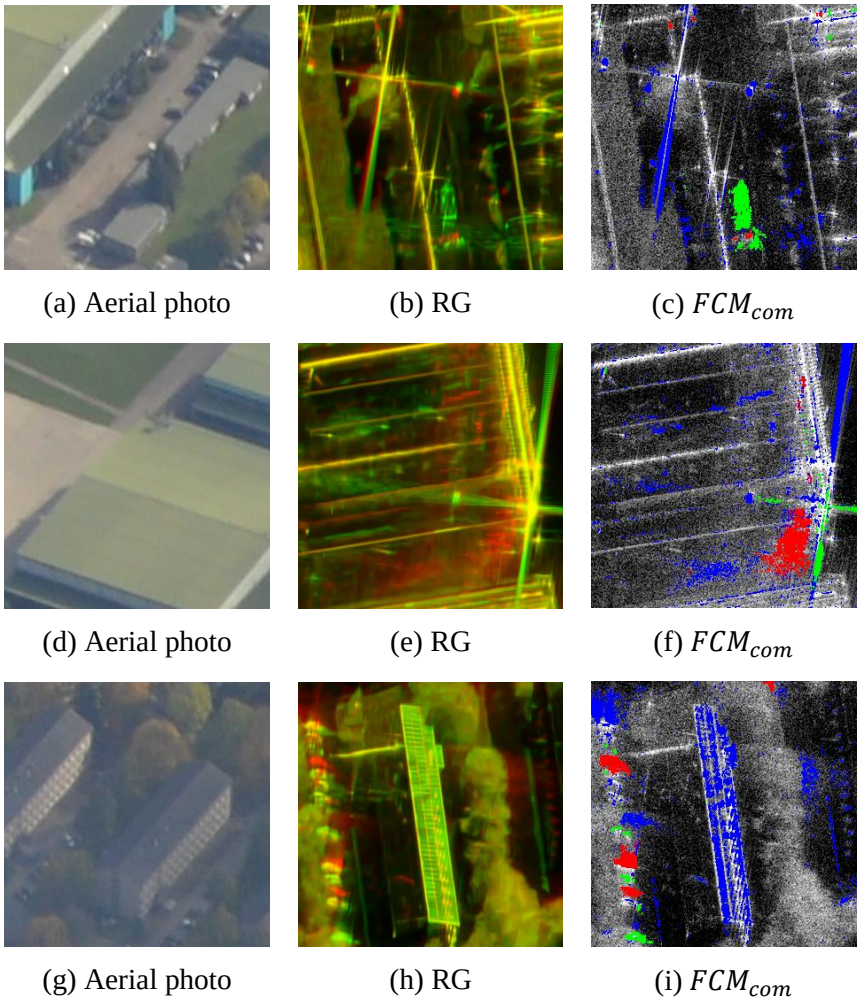

(a) Aerial photo (b) RG (c) FCM_{com}

(d) Aerial photo (e) RG (f) FCM_{com}

(g) Aerial photo (h) RG (i) FCM_{com}

Fig. 3.13 Aerial photos, RG composites and change maps derived from the pair MEM1-MEM3 under presence of diverse image artifacts. (a-c) Patch 1. (d-f) Patch 2. (g-i) Patch 3.

3.4 Discussion and Conclusions

3.4.1 Discussion

Based on the numerical results listed in Table 3.2, and Table 3.4, the performance of the method slightly degrades by increasing m while PD_r tended towards unity. This suggests that the method converges to the solution derived from the single-look complex images. This behavior can be explained by the finer sampling of the θ domain when m is increased, since changes caused by low to moderate anisotropic targets are less likely to be canceled. This has the benefit of providing better PD_r at the cost of modest improvements in the rest of the quality indicators. Lower scales were more permissive, cancelling changes caused by low anisotropic targets, thus reducing PD_r. The well-known trade-off between false alarm and detection rate remained pre-

sent. This compromise is given by the number of scales, which is directly related to the amount of anisotropy or scatter persistence being considered.

Table 3.3 and Table 3.5 compare the performance of the proposed method with existing change detectors. For CD-LRT and single-look processing we observed that it requires denoising due to the low detection rates achieved. Consequently, the performance of the method improves when using multi-looking; however, the resulting changes were no longer detected in the resolution space of the single-looks. Similar observations were made for CD-PCAk and CD-$GKLD_{WAV}$ due to the usage of sliding windows or blocks of pixels.

In this work, the MSF was processed using the minimum operator to ensure that the dynamic range of the images treated in the different stages was comparable, so that additional setting parameters were not required. The *min* operator is also responsible for the false alarm and detection rate trade-off, as the minimum value of each pixel at scale m can only be identical to or smaller than that at scale $m-1$. A different operator, such as the standard deviation, could lead to a different behavior of the method, at the cost of introducing additional setting parameters.

Quality indicators were derived assuming that the slight reduction of the detection rate was caused only by the MSF. However, the migration of the shadows along the aperture time, e.g. the shadow of the vehicles, can also be responsible for reducing the detection rate. The border of a mask indicating a change could be slightly reduced when exploiting the proposed method due to this shadow effect. This was not considered here when labelling the synthetic ground truth.

Fig. 3.12 (g-i) shows the removal of a change caused by a car. Possible reasons are: 1) the point spread functions of the car were anisotropic, 2) the SNR and resolution provided by the MSF were not sufficient to detect the change, and 3) the change was detected in the curvelet domain due to its quasi-linear shape. The corresponding solutions are: 1) exploit higher resolution scales so that changes caused by highly anisotropic targets can be retained, 2) for a given azimuth antenna beam-width, design the MSF using a different resolution sequence to provide better resolution and SNR, and 3) use of different morphological transforms that can better isolate changes of interest.

For inconsistent geometries, false alarms caused by migration of the shadowed areas, rotation of sidelobes, and displacement of the point spread functions of some scatterers of the buildings were cancelled as shown in patches Fig. 3.12 (j-o), and Fig. 3.13 (g-i).

The performance of the method depends to some extent on the fusion strategy in use. Quality indicators showed that fusion at the pixel level provided moderate results, but is computationally efficient. The combined strategy yielded best results; however, it is assumed that changes can be characterized by certain properties, like shape. This suggests that object-based change detection approaches can be more suitable for high resolution SAR imagery than pixel-based methods.

The value of κ was mapped by iteratively thresholding with a pair of thresholds $[T_1,T_2]$. With the presence of false alarms caused by image artifacts, Fig. 3.7 and Fig. 3.10 show that single-look based methods optimize κ by reducing the detection rate; i.e. by simultaneously decreasing T_1 and increasing T_2. Information on the spatial behavior of the targets enables further optimization of κ while retaining a large amount of the detection rate offered by traditional methods, even when using less restrictive thresholds. The fringes in Fig. 3.7 (c) located at T_2= 2 dB and 7 dB, and those in Fig. 3.7 (d) located at T_2= 4.2 dB were caused by the parameter F_{ov}. Setting parameters can abruptly modify the value of κ and thus a non-uniform response was observed. In contrast, the response of κ did not show fringes when using the fusion at the pixel level strategy because this strategy does not require additional parameters.

Patch 4 of Fig. 3.8 (a-b), and Fig. 3.13 (g-i) shows that false alarms caused by unfocused targets, such as trees under windy conditions, were mitigated. Change maps from the pair

MEM1-MEM3 shown in Fig. 3.12 and Fig. 3.13 provided an overview of the performance of the multisquint-based approach to remove false alarms caused by typical artifacts in high resolution SAR imagery.

If changes are caused by buildings, the SAR images can be better focused by using a Digital Surface Model of the area of interest. This can ensure that the spatial behavior of the point spread function of the scatterers does not vary along the synthetic aperture. Changes caused by natural distributed targets, such as meadows or agricultural fields require different dissimilarity functions [23] than those used here. However, detection of changes caused by these types of targets was beyond the scope of this work.

3.4.2 Conclusions

The proposed multisquint framework was applied to mitigate errors caused by artifacts common in SAR image change detection. Information on the spatial behavior of the targets was shown to provide better results than those obtained by only exploiting single-look complex images, as commonly done in traditional change detection. Moreover, the multisquint approach was shown to be less sensitive to errors caused by the difference of the acquisition geometries. The kappa coefficient, the false alarm rate and the classification error were improved on average by a factor 1.9, 3 and 2.9 respectively, while preserving 95% of the detection rate obtained with traditional change detection techniques.

Concerning the change map fusion strategies, fusion at the object level was found to be more suitable for high resolution SAR imagery than pixel-based approaches at the cost of assuming *a priori* knowledge, such as certain characteristics of the potential changes, or including additional setting parameters.

Adaptation of the multisquint framework to multichannel SAR data sets, with interferometric and polarimetric channels, is foreseen in future work.

Acknowledgments

The authors would like to thank Jens Fischer from the German Aerospace Center DLR for his support on geometric and radiometric calibration of the images provided by the F-SAR sensor. They would also like to acknowledge the pilots and all institutions involved in the F-SAR data collection during the Swiss campaign in 2013, and the reviewers for their helpful contributions in improving this paper.

4 RANGE ADAPTIVE PROCESSING AND MULTISQUINT PROCESSING MODE FOR SAR IMAGE CHANGE DETECTION

This chapter has been published as: E. M. Dominguez, M. Frioud, D. Small, and D. Henke, "Range Adaptive Processing and Multisquint Processing Mode for SAR Image Change Detection," to be presented at the 12th European Conference on Synthetic Aperture Radar (EUSAR), Aachen, Germany, 2018.

For clarity, the paper has been reformatted and the references are listed at the end of the thesis; otherwise, the content is the same as in the peer-reviewed conference article.

E.M.D. and D.H. designed the study. E.M.D. developed the method. E.M.D. and M.F. performed the analysis with advice of D.H. E.M.D. wrote the manuscript and all co-authors reviewed and edited the manuscript.

Abstract

Synthetic Aperture Radar (SAR) image change detection enables mapping for applications such as human activity monitoring and urban studies. In this work we analyze the use of adaptive range processing and multisquint processing for change detection purposes. Numerical evaluation showed that both processing methods can reduce errors caused by image artifacts while preserving detection rates similar to those offered by the corresponding matched filtering and single-look processing. When changes were caused by isotropic targets, best results were obtained when combining range adaptive and multisquint processing.

4.1 Introduction

Image change detection is a technique comparing images of the same area acquired at different times [2]. Applications are in human activity observation [118], risk management [4], urban studies [18] and environmental observation [2]. SAR sensors are well suited as data can be reliably collected over unfavourable weather and daylight conditions. However, SAR data introduces challenges that can complicate the processing, such as noise, focusing errors, and presence of image artifacts [14].

Many change detectors have been proposed to mitigate errors caused by noise [13, 75]. Apart from noise-induced errors, the presence of image artifacts [63], such as side-lobes, increases the false alarm rate, degrading the reliability of the change maps. Sidelobes are introduced by the well-known Matched Filter (MF) during SAR image formation [119]. On the other hand, the MF provides a high Signal to Noise Ratio (SNR) and spatial resolution while being computationally efficient [64]. In this manner, high-level detailed and subtle changes can be detected with the corresponding focused SAR images. To preserve these detection characteristics while reducing the false alarms caused by the presence of sidelobes, we can: 1) utilize pulse compression methods capable of providing images at the highest attainable resolution and SNR, similar to those of MF, but with lower sidelobe levels, or 2) identify and remove *a posteriori* the false alarms caused by the sidelobes introduced by the MF. Solutions based on 1) or 2) can be referred to as those working at the processing level (prevention) or post-processing level (mitigation) respectively.

Adaptive processing methods, such as Adaptive Pulse Compression (APC), are valid solutions working at the processing level. APC preserves resolution while providing a negligible SNR loss and reducing sidelobes [91]. However, it requires long computation times. For this reason, we only consider here analysis of APC applied to the range dimension.

Alternatively, at the post-processing level, mitigation of the presence of sidelobes can be performed by exploiting beamforming since the spatial response of sidelobes varies during the aperture time [120]. Spatial information can be gathered via multisquint processing [120, 121], where each squint is formed with a set of echoes scattered with a certain direction of arrival. Since the squints do not have the highest attainable resolution and are not artifact-free, the pair of single-looks is still required to detect changes at nominal resolution. By exploiting multisquint processing, one can derive a new pair of images where sidelobes do not appear in the same image samples as those of their corresponding single-looks. Errors caused by sidelobes can be identified due to their non-permanent scattering regime and removed *a posteriori* from the change map of the single-looks.

In this work, we analyze the performance offered by APC and multisquint processing to reduce errors caused by image artifacts in SAR change detection. Numerical evaluation showed that adaptive and multisquint processing can improve the kappa coefficient by at least a factor 1.22 when applied separately in comparison to that offered by the SAR images focused with the MF and single-look processing. This factor rose to 1.86 when exploiting combined range adaptive and multisquint processing. The paper is organised as follows: Section 4.2 describes range adaptive pulse compression and multisquint processing for SAR image formation. We then describe the change detectors and the numerical evaluation procedure. Section 4.3 illustrates the results obtained using real airborne SAR imagery. Finally, a discussion of the results is presented followed by conclusions.

4.2 Method

4.2.1 Sensor, Data and Test Site

The image pair was acquired in 2012 with Fraunhofer FHR's MEMPHIS sensor [122] over the *Allgäu* airport in *Memmingen*, Germany, (N47.98°, E10.23°). MEMPHIS uses Linear Frequency Modulated (LFM) signals of 0.4 μs and 200 MHz bandwidth. The SAR data was recorded in linear stripmap configuration at Ka-band. The temporal baseline was 1 hour and 10 minutes. During that time, changes were introduced by cars, luggage transporters and a civilian aircraft. The SAR data was focused in time domain using the approaches described in the following two subsections.

TABLE 4.1
DESCRIPTION OF THE USED MEMPHIS DATA SET

Data	δ_r	δ_a	θ_{inc}	ϕ	**Time**
MEM 1	0.75m	0.08m	50°	-130°	12:18:46
MEM 2				-129°	13:08:07

The slant range resolution δ_r, azimuth resolution δ_a, incidence angle at mid-range θ_{inc}, and flight path heading ϕ of the data takes are listed in Table 4.1. The azimuth beamwidth θ_a of the antenna gain pattern was approximately 3°.

4.2.2 Range Processing: deterministic and adaptive solutions

For pulsed sensors, SAR image focusing is performed by applying pulse compression methods to each dimension sequentially, range and azimuth [119]. In range, the r-th delay sample of a range profile can be computed from

$$x(r,t) = w(r,t) \cdot y(r,t) \tag{4.1}$$

where $w(r,t)_{N\times 1}$ is a filter and $y(r,t)_{N\times 1}$ is a vector of N contiguous samples of the received pulse at slow time t. The most often used pulse compression method is the MF. In that case, w does not depend on r and is computed as the complex conjugate time reversed-copy of the N-length transmitted waveform. In the following, we simplify notation by assuming that the transmitted waveform does not depend on t.

To reduce sidelobes while preserving resolution and SNR, we can apply a complex-valued filter w adapted to each individual range bin [91]:

$$w_i(r) = \rho_i(r)(C_i(r) + R)^{-1}s \tag{4.2}$$

where $\rho_i(r) = |x_i(r)|^2$ is the power estimates of the range bins of the profile x_i, $R_{N\times N}$ is the noise covariance matrix, and $C_i(r)$ is the $N \times N$ weighted covariance matrix of the transmitted waveform s. A range profile is derived by inserting (4.2) into (4.1). However, to compute (4.2) we first require an estimate of the power of the surrounding range bins $\rho_i(r)$. For this purpose, an initialization stage is applied, e.g. using the MF ($\rho_0 = |x_0(r)|^2, w_0 = s^H$), after successive L iterations, a refined range profile is obtained based on the prior power estimates. This iterative procedure is referred to as Adaptive Pulse Compression [91]. Since adaptive processing is not computationally efficient, we only evaluate the performance of APC when the initialization stage is the MF and L=2.

4.2.3 Azimuth Processing: single-look and multisquint solutions

In contrast to the range dimension, the azimuth samples are not aligned. We adopted pulse compression and signal alignment via the interpolated MF, also called Time Domain Back-

Projection (TDBP) [65]. Omitting calibration factors, a backscatter element of a geocoded bandpass SAR image *I* is focused via TDBP with:

$$I(E_0, N_0) = \sum_{t=t_1}^{t_2} \dot{x}\left(\frac{R_s}{c}, t\right) \tag{4.3}$$

where $R_s = \sqrt{(X(t) - x_0)^2 + (Y(t) - y_0)^2 + (Z(t) - z_0)^2}$ is the slant range, and (E_0, N_0) the map coordinates of the element, which are transformed to the equivalent global Cartesian coordinates (x_0, y_0, z_0) using a Digital Elevation Model (DEM). $\big(X(t), Y(t), Z(t)\big)$ is the sensor position in global Cartesian coordinates at slow time t, $L = t_2 - t_1$ the aperture length, c the speed of light, and $\dot{x}$ the range compressed signals derived from (4.1) after up-conversion. By using (4.3), we take advantage of the full theoretical bandwidth of the azimuth signals, yielding the well-known single-look [65]. However, single-looks do not provide spatial information of the targets. To do so, we introduce in (4.3) a beamformer W with an angular selectivity bandwidth of $\Delta\theta$. The sampling space of W is constrained inside the region $[-\theta_a/2, \theta_a/2]$, where θ_a is the azimuth beamwidth of the antenna pattern in reception. To collect the spatial response of the targets, we first generate a 2-dyadic *M*-stage resolution sequence of squints (the *m*th-scale is composed of 2^m squints) with $\Delta\theta_{\mathrm{m}} = \Delta\theta_{\mathrm{m}-1}/2^m$, and $\Delta\theta_0 = \theta_{\mathrm{a}}$. The beamformer $\mathrm{W}(\Delta\theta_{\mathrm{m}})$ is a *rect* function in θ. The azimuth angle θ is computed with the antenna pointing vector and the position of the backscattering element (E_0, N_0) at slow time t. The *n*th-squint at the *m*th-scale is focused via:

$$\ddot{I}(E_0, N_0, \mathrm{m}, \mathrm{n}) = \sum_{\tau} \dot{x}\left(\frac{R_s}{c}, t\right) \cdot W(\mathrm{m}, n) \tag{4.4}$$

with

$$W(\mathrm{m}, \mathrm{n}) = \begin{cases} 1, & {}^{-\theta_a}/_2 + \Delta\theta_m \cdot (n-1) \le \theta \le {}^{-\theta_a}/_2 + \Delta\theta_m \cdot n \\ 0, & otherwise \end{cases} \tag{4.5}$$

The azimuth resolution of a squint depends on $\Delta\theta$; and thus, information of the spatial response of the targets is retrieved at the cost of a degraded azimuth resolution and stronger azimuth side-lobes [120].

A set $\{\ddot{I}(\Delta\theta)\}$ is formed by combining via complex-valued additions the 2^m squints at scale m in (4.4) to guarantee that the azimuth resolution is constant with m and enough to detect the smallest changes of interest; i.e. $\Delta\theta_{m=1..M} = \Delta\theta$. In this work, the azimuth resolution of the images in $\{\ddot{I}(\Delta\theta)\}$ is $2\delta_a$, being δ_a the azimuth resolution of the corresponding single-look. We restrict the resolution sequence to the cases $M = 1,2$, being *M* the lowest resolution scale. Finally, we derive a new set of images after filtering artifacts. This is performed by applying a *min* operator to the log-transformed and radiometric calibrated images in $\{\ddot{I}(\Delta\theta)\}$ at scale m, yielding one image I_{MS} per scale: $\{I_{MS}(m)\}_{m=1\ldots M}$.

4.2.4 Change Detection

To extract changes at nominal resolution, we calculate a Difference Image (DI) by subtracting the log-transformed single-looks I_1 and I_2 [3] from the MF- and the APC-based processed images. Subsequently, we denoise the DI via Block Matching 3D [35]. Finally, the denoised DI is thresholded to derive a tertiary change map where the backscatter increase(decrease) class is labelled with +1's(-1's) respectively, and the unchanged class is labelled with 0's. Thresholding is performed using a set of thresholds $[T_1, T_2]$, with $T_1 < 0\ dB$ and $T_2 > 0\ dB$. We denote the change map derived from the single look images as the $\mathrm{ICM_{MF}}$ or $\mathrm{ICM_{APC}}$, where the subscript denotes the range compression method used to focus I_1 and I_2.

At a post-processing stage, errors caused by sidelobes can be reduced by utilizing $\{I_{MS}(m)\}_{m=1\ldots M}$ via a three-staged change detector [120]. First, we compute the ICM using the single-looks. Second, we derive a second map using the same change detector as in the previous step using the pair $I_{1MS}(m)$ and $I_{2MS}(m)$. A final change map is obtained after fusing these at the pixel level with a logical AND operator. Bearing in mind the labels of the change and unchanged classes, this operator permits the retention of common changes, while cancelling the others. In this manner, most changes caused by artifacts are not transferred to the fused change map, referred here to as FCM. In the following, we denote the change maps derived from the three-staged change detector as $\text{FCM}_{m\text{MF}}$ or $\text{FCM}_{m\text{APC}}$ depending on the range compression method used for image formation, and scale m.

4.2.5 Numerical Evaluation

After manually labelling a synthetic reference, we derive the detection rate PD, the false alarm rate FA, the classification error ε and the kappa coefficient κ [116]. These indicators were computed from the ICM_{MF}, ICM_{APC}, $\text{FCM}_{m\text{MF}}$, and $\text{FCM}_{m\text{APC}}$ as a function of $[T_1, T_2]$ and scale m. Performance was also studied with the ratio of the indicators: $\varepsilon_{r-i} = \varepsilon_i / \varepsilon_{ICM_{MF}}$ and $\kappa_{r-i} = \kappa_{ICM_{MF}} / \kappa_i$, being $\varepsilon_{ICM_{MF}}$ and $\kappa_{ICM_{MF}}$ the classification error and kappa coefficient derived from ICM_{MF}. ε_i and κ_i are the classification error and kappa coefficient obtained from the change maps under evaluation (ICM_{APC}, $\text{FCM}_{m\text{MF}}$ and $\text{FCM}_{m\text{APC}}$), identified with the subscript i.

4.3 Results

The image pair listed in Table 4.1 was used to evaluate the performance of the different change detectors and corresponding processing schemes. The RG(B=0) composite of the area of interest is shown in Fig. 4.1. The RG image was formed with the reference SAR image in the red channel and the test image in the green channel. It is intended to give the viewer an indication of potential changes; i.e., the changes with a higher likelihood of occurrence are highlighted in red and green, whereas yellow indicates a low probability of change. Changes were mainly caused by cars (indicated by blue rectangles), a civilian aircraft (dashed blue rectangle), and luggage transporters (blue circles).

Fig. 4.2 and Fig. 4.3 illustrate the response of ε_r and κ_r respectively as a function of the thresholds $[T_1, T_2]$, scale m, and processing method. We omit the graphical results derived from $\text{FCM}_{1\text{APC}}$ since they are moderate in comparison to those obtained from $\text{FCM}_{2\text{APC}}$. The ratio of the classification error ε_{r-i} showed that best performance was obtained when combining APC and multisquint processing. Poorest performance was seen when applying only APC. Comparison of the indicators $\varepsilon_{r-FCM_{1MF}}$ and $\varepsilon_{r-FCM_{2MF}}$ in Fig. 4.2 (b) and (c) showed that better results were obtained for larger m. This was observed independently of the range processing method. Similar behaviour was confirmed when evaluating the ratio of the kappa coefficients shown in Figure 3. Note that the backscatter increase class is dominant in comparison to the backscatter decrease class, and thus the ratio of the indicators did not show a symmetric response.

Table 4.2 lists the performance of the methods when thresholding with the set [-5, 5] dB. These thresholds were chosen based on iterative thresholding and visual inspection of the corresponding change maps. In terms of the ratio of the kappa coefficient κ_r, we observed that $\text{FCM}_{2\text{APC}}$ yielded the best performance. Poorest performance was seen when applying only range adaptive processing. The value of κ of the change maps obtained when only utilizing multisquint processing increased slightly with m. In terms of the detection rate, we observed that ICM_{APC} yielded second best performance, while the poorest performance was seen with combined range adaptive and multisquint processing. The detection rate of the change maps obtained when exploiting multisquint processing decreases with m.

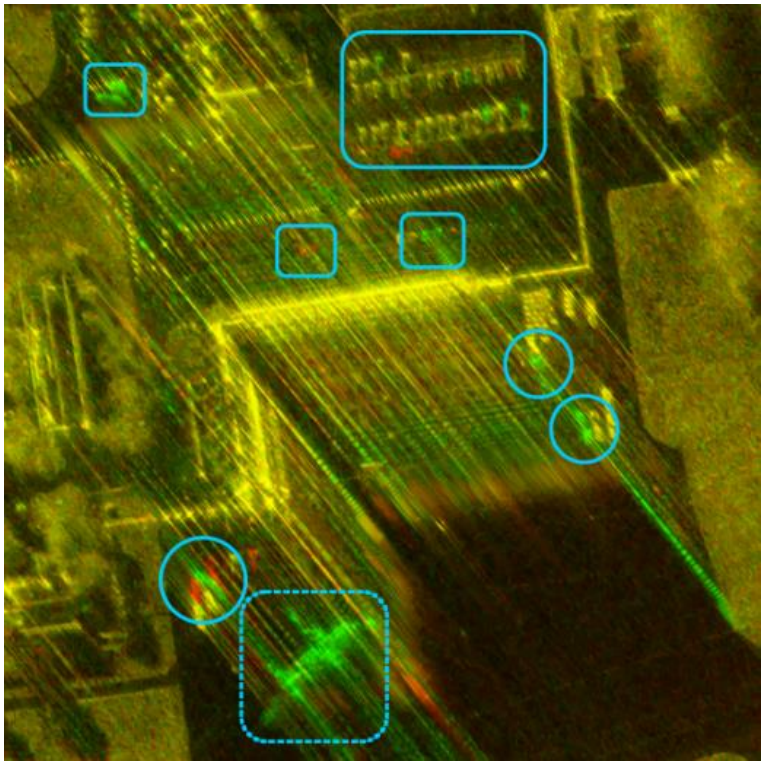

Fig. 4.1 RGB composite of the area of interest (R= reference SAR image, G=test SAR image, and B=0).

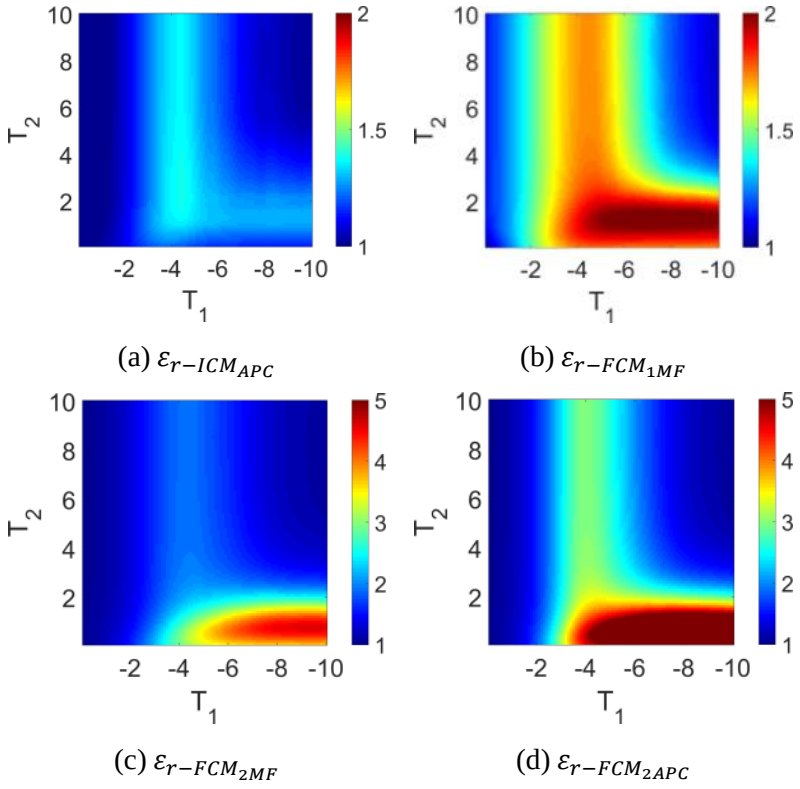

(a) $\varepsilon_{r-ICM_{APC}}$ (b) $\varepsilon_{r-FCM_{1MF}}$

(c) $\varepsilon_{r-FCM_{2MF}}$ (d) $\varepsilon_{r-FCM_{2APC}}$

Fig. 4.2 Ratio of the classification error ε_{r-i} as a function of T_1, T_2, scale m and processing method.

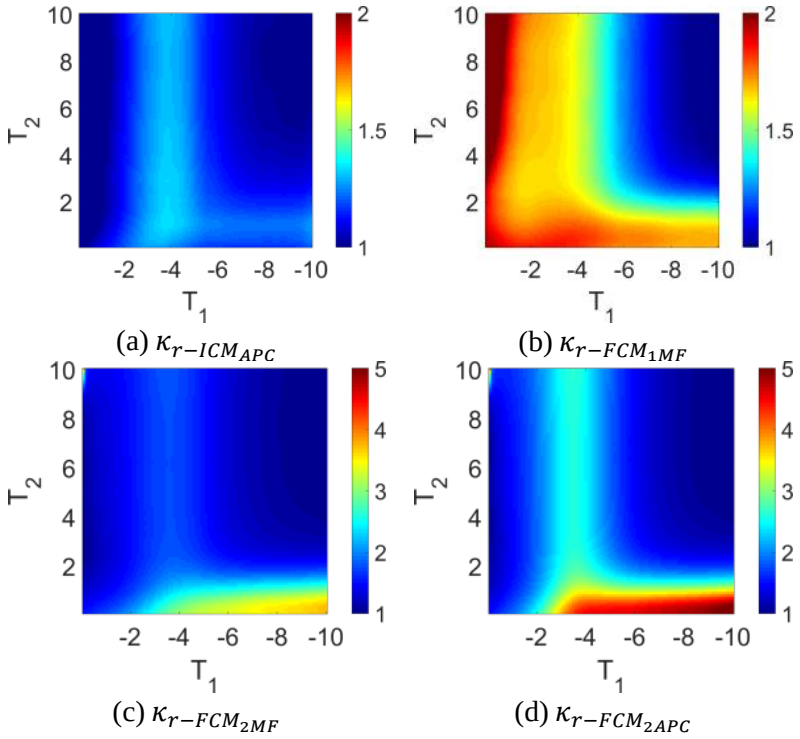

(a) $\kappa_{r-ICM_{APC}}$ (b) $\kappa_{r-FCM_{1MF}}$

(c) $\kappa_{r-FCM_{2MF}}$ (d) $\kappa_{r-FCM_{2APC}}$

Fig. 4.3 Ratio of the kappa coefficient κ_{r-i} as a function of T_1, T_2, scale m and processing method.

TABLE 4.2
NUMERICAL EVALUATION OF THE METHODS AS A FUNCTION OF THE SCALE *M* AND PROCESSING METHOD WHEN $|T_1| = T_2 = 5$ DB

Method	ε **(%)**	κ	**PD (%)**	**FA (%)**	κ_r
ICM_{MF}	3.3230	0.2509	78.3693	3.1855	-
ICM_{APC}	2.5115	0.3062	77.2598	2.3595	1.2204
FCM_{2MF}	1.9399	0.3587	75.0568	1.7671	1.4297
FCM_{4MF}	1.7896	0.3813	76.1407	1.6238	1.5197
FCM_{2APC}	1.3743	0.4402	74.2062	1.1908	1.7545
FCM_{4APC}	1.2531	0.4671	75.2710	1.0767	1.8617

Fig. 4.4 shows the ICM_{MF} overlaid on the reference SAR image. The ICM_{MF} was obtained after thresholding with the set [-5, 5] dB. False alarms caused by prominent sidelobes can be recognized by visual inspection. Fig. 4.5 illustrates the FCM_{2APC} overlaid on the reference image. The additional class, marked in blue, indicates changes that were detected in ICM_{MF} but removed when utilizing combined adaptive and multisquint processing modes. One observes that most changes, indicated by light blue rectangles and circles were preserved, while errors caused by sidelobes were partially removed.

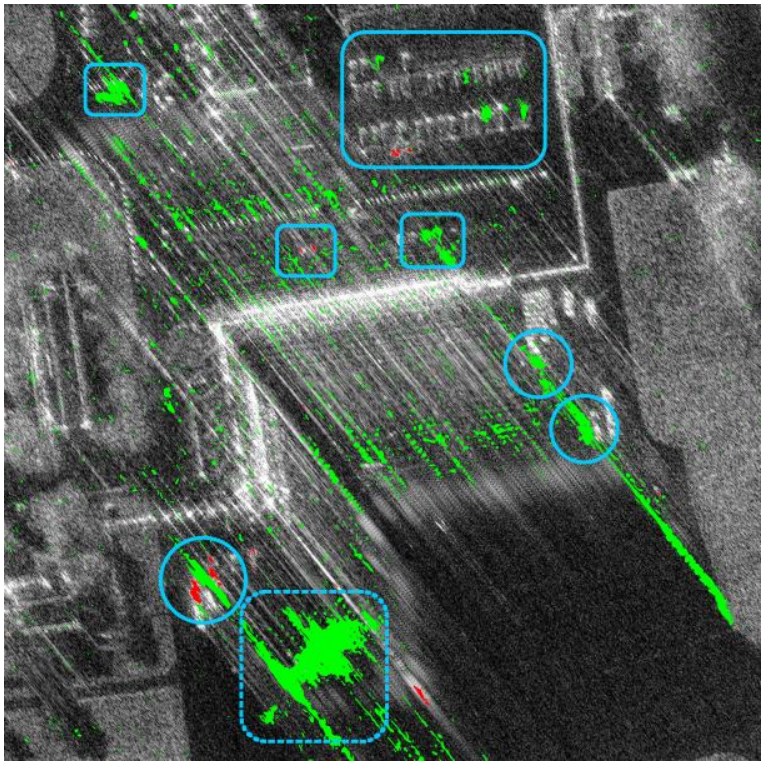

Fig. 4.4 Change map ICM_{MF} overlaid on the reference image. Pixels marked in green and red indicate targets that entered (green) or left (red) the area of interest.

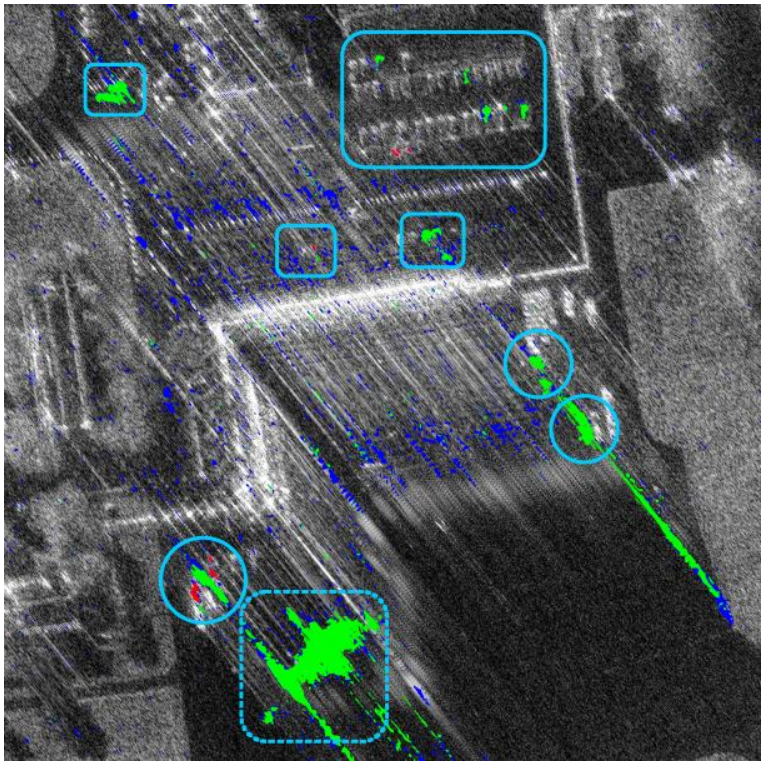

Fig. 4.5 Change map FCM_{2APC} overlaid on the reference image. Pixels marked in green and red indicate that targets entered (green) or left (red) the area of interest. Pixels marked in blue indicate removed changes, originally detected in ICM_{MF}.

4.4 Discussion

The numerical evaluation illustrated in Fig. 4.2 and Fig. 4.3 shows that modest results were obtained when applying only adaptive processing. As reported in [119], the main reasons were: 1) APC provides moderate sidelobe reduction efficiency when the transmit waveform is an LFM signal, and 2) the performance of APC degrades when the transmitted signal and the received signals do not perfectly match. The performance of APC also depends on the initialization stage and the number of iterations used.

Both the classification error ε and the kappa coefficient κ obtained when exploiting multisquint processing improved with *m*. This suggests that better performance can be achieved by utilizing higher values of *m*. Nonetheless, as described in [120], the detection rate, and thus the rest of the indicators, tends towards that of the ICM_{MF} once the optimal value of *m* is exceeded. From Table 4.2, the detection rate was slightly lower than that of the ICM_{MF}. If removal of desired changes occurs, then one can apply the following solutions: 1) exploit higher resolution scales so that changes caused by highly anisotropic targets are retained, and 2) for a given azimuth antenna beamwidth, derive $\{I_{MS}(m)\}_{m=1\ldots M}$ using a different resolution sequence to provide better resolution and SNR.

The change maps in Fig. 4.4 and Fig. 4.5 show the performance of the combined adaptive and multisquint-based processing approach in comparison to that offered by MF and single-look processing. Most false alarms caused by sidelobes were removed while preserving a large proportion of the changes.

Comparison of the results obtained by applying APC only or multisquint processing suggests the following: 1) if changes are caused by isotropic targets then exploiting spatial information is more effective than adaptive processing only, 2) the detection rate of ICM_{APC} is very similar to that of ICM_{MF} without assuming a permanent scattering regime, 3) if sidelobes mask areas with changes, then adaptive processing can be more suitable because the change detector is more likely to preserve the underlying change, and 4) combination of both processing modes can yield best results when changes are caused by isotropic targets.

4.5 Conclusions

In this work, we examined the advantages and drawbacks offered by adaptive and multisquint processing for change detection purposes. We showed that both processing modes can effectively provide better results than those obtained by using a conventional Matched Filter combined with single-look processing, but at the cost of high computation time or assuming that changes are caused by isotropic targets. Results obtained by utilizing beamforming can be further improved when combined with adaptive processing. Extension of adaptive and multisquint processing to multichannel SAR is planned in future work.

Acknowledgments

This work was funded by *armasuisse*. We are grateful to all collaborators of the involved institutions for their contribution during the measurement campaign.

5 A BACK-PROJECTION TOMOGRAPHIC FRAMEWORK FOR VHR SAR IMAGE CHANGE DETECTION

This chapter has been submitted to IEEE-TGRS as: E. M. Domínguez, C. Magnard, E. Meier, D. Small, M. E. Schaepman, and D. Henke, "A Back-Projection Tomographic Framework for VHR SAR Image Change Detection," *IEEE Transactions on Geoscience and Remote Sensing*, 2018.

For clarity, the paper has been reformatted and the references are listed at the end of the thesis; otherwise, the content is the same as in the journal article.

E.M.D., E.M., and D.H. designed the research. E.M.D. and C.M. processed the data and developed the methodology with scientific advice of M.E.S. and D.H. All authors wrote the manuscript, with main contributions of E.M.D.

Abstract

Information on 3-D structure expands the scope of change detection applications, for example in urban studies, human activity and forest monitoring. Current change detection methods do not fully consider the specifics of SAR data or the properties of the corresponding image focusing techniques. We propose a three-stage method complementing the properties of 2-D and 3-D very high resolution (VHR) SAR imagery to improve the performance of 2-D only approaches. The method takes advantage of back-projection tomography to ease translation of the 2-D location of the targets into their corresponding 3-D location and vice versa. Detection of changes caused by objects with a small vertical extent is based on the corresponding backscatter difference, while changes caused by objects with a large vertical extent are detected with both backscatter and height difference information combined in a conditional random field. Using multitemporal images, the kappa coefficient improved by a factor of two in comparison to traditional schemes.

LIST OF ACRONYMS USED IN THE TEXT

AIC	Akaike Information Criterion
BM3D	Block Matching 3-D
BM4D	Block Matching 4-D
CRF	Conditional Random Field
CD-DI_{3D}	Change Detection, 3-D Difference Image
CD-HD	Change Detection, Hausdorff Distance
CD-MSQ	Change Detection, Multisquint
DEM	Digital Elevation Model
DI	Difference Image
DSM	Digital Surface Model
DTM	Digital Terrain Model
EDC	Efficient Detection Criterion
EM	Expectation Maximization
ICM	Initial Change Map
InSAR	Interferometric SAR
LiDAR	Light Detection and Ranging
MDL	Minimum Description Length
MSF	Multisquint Framework
PSI	Persistent Scatterer Interferometry
SAR	Synthetic Aperture Radar
SNR	Signal to Noise Ratio
TDBP	Time Domain Back-Projection
TomoSAR	Tomographic SAR
VHR	Very High Resolution

5.1 Introduction

Change detection from remote sensing images provides mapping applications for diverse tasks such as urban studies [18, 19], human activity monitoring [21, 120] and risk management [4, 6]. The availability of systems delivering 3-D information has broadened the scope of change detection applications, particularly for urban studies [123, 124], and forest monitoring [125, 126]. Additionally, 3-D change detection is more robust against differences in illumination, and can provide a new level of detail, overcoming traditional 2-D change detection methods [127, 128].

Typically, 3-D change detection is performed using LiDAR data or a set of optical images after photogrammetric processing [127, 128]. Main focus has been in addressing accurate data co-registration [128, 129], or developing dissimilarity functions suitable for changes of interest [130, 131]. Current methods do not account for 3-D SAR imagery. Related work reported in [132] takes advantage of persistent scatterer interferometry (PSI) to retrieve the height of buildings for time series analysis and change detection. However, height information was utilized in a two-dimensional spatial domain. Disregarding the 2½-D structure of the data acquired from an interferometric SAR (InSAR) configuration led to the absence of layover correction [133], and thus, the method is sensitive to errors caused by differences in illumination.

SAR sensors provide three dimensional imaging by extension of the synthetic aperture in elevation [66]. This configuration, known as tomographic SAR (TomoSAR), permits to resolve layover and detect multiple scatterers within the resolution cell [134]. The performance of VHR TomoSAR has not been studied for change detection purposes due to the limited availability of data. Existing methods do not account for the specifics of the SAR data such as its associated sources of error (amplitude and phase noise), nor the information retrieved (backscatter and height estimates). They also fail to take advantage of the characteristics of the SAR image formation method. A high-performing tomographic processor can provide co-registered 3-D images, circumventing the need for data co-registration methods like the well-known Iterative Closest Point [135], enabling the subtraction of the backscatter at the voxel level without a need for regridding, as in the case of LiDAR or optical data.

In this work, we propose a three-stage TomoSAR change detection approach where 2-D and 3-D methods are combined to overcome their respective weaknesses and take advantage of their strengths. The change detector exploits: 1) a back-projection tomographic SAR focusing method, similar to that reported in [89], providing automatically co-registered geocoded 3-D images, 2) the normal dimension of the acquisition geometry, utilized as a ground-height proxy enabling 2-D to 3-D image conversion and vice versa, and 3) information of the backscatter and height differences.

First, we detect changes caused by targets with a small vertical extent (short targets) using a traditional 2-D image change detector. Second, we take advantage of the information offered by SAR tomography for changes caused by targets with a large vertical extent (tall targets). A 3-D change map is derived after merging the results from the two previous stages. Numerical evaluation showed that the combined method outperformed traditional 2-D SAR image change detection and approaches developed for LiDAR point clouds, improving the kappa coefficient by a factor two. This work provides first references demonstrating the performance of SAR tomography for change detection applications.

The paper is organized as follows: Section 5.2 introduces the back-projection framework utilized here for TomoSAR processing. Subsequently, we describe the three stages of the proposed change detector, emphasizing the combination of backscatter and height features by means of a conditional random field (CRF) model. Section 5.3 illustrates the results with high resolution airborne TomoSAR imagery acquired in medium density urban scenarios. Finally, section 5.4 concludes with a discussion of the results and conclusions.

5.2 Method

The combined method consists of three stages. First, we utilized a 2-D approach to detect changes at the ground level, assumed to be caused by short targets. Then, changes caused by tall targets were detected in the second stage using a 3-D method. There, backscatter and height difference information were combined by means of a CRF to alleviate errors caused by amplitude and phase noise. Third, the 2-D change map from the first stage was transformed into a 3-D map using the normal dimension of the tomographic configuration. Finally, we computed a 3-D map by fusing the 3-D converted map and the 3-D map with the changes caused by tall targets. Fig. 5.1 shows the general scheme of the proposed method.

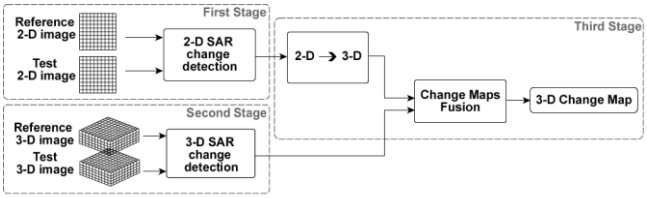

Fig. 5.1 Architecture of the combined change detector.

5.2.2 Tomographic Processing and Data Format

From [136], a TomoSAR data set acquired with $K > 2$ tracks (multipass) or receivers (single-pass) can be focused using time domain Back-Projection (TDBP). Omitting calibration factors and signal weightings, the backscatter γ_0 of an element acquired from channel k is focused at height h_i above a digital elevation model (DEM) via:

$$\gamma_0^{k,i}(e,n,h_i) = \left[\sum_{\tau=\tau_1}^{\tau_2} s\left(\frac{2R_s}{c},\tau\right)\cdot W(\theta)\right]\cdot e^{-j\zeta_1} \tag{5.1}$$

where (e,n,h_i) are the map coordinates of the voxel, $L = \tau_2 - \tau_1$ the aperture length, s the bandpass range compressed signals, R_s the slant range, c the speed of light, and τ the slow time. ζ_1 is the phase term for baseband, and $W(\theta)$ is here a spatial filter defined as a function of the azimuth angle θ for multisquint processing mode [120]. A 3-D image cube γ_0^k was derived from (5.1) with $h_i = h_0 + i\Delta h, i = 0,\dots,i_{amb}$ where h_0 is the height of the ground, Δh the height sampling spacing and $h_0 + i_{amb}\Delta h$ a height smaller than the ambiguity height h_{amb}, defined as the maximum height of the imaged volume that can be reconstructed unambiguously [137]. $\gamma_0^{k,0}$ is the 2-D single-look image from channel k focused on the ground. Subsequently, we reduce sidelobes in the normal direction with $\gamma_0^{k=1,\dots,K}$ using multi-look processing combined with maximum likelihood [102]. Block-Matching 4-D (BM4D) [37] is applied to the resulting 3-D image to further reduce errors caused by phase noise. This yielded a 3-D image cube γ_0^{3D} with the backscatter estimates obtained via maximum likelihood. We computed the number of scatterers $0 \le p(e,n) \le (K-1)$ per ground resolution cell (e,n) with the efficient detection criterion (EDC) in [138] with:

$$p(e,n) = \arg\min_{m\in[0;K-1]}\left[(N_{looks}-k)\cdot m\cdot \ln\left(\frac{\sqrt[K-m]{\prod_{i=m+1}^{K}\lambda_i(e,n)}}{(1/(K-m))\sum_{i=m+1}^{K}\lambda_i(e,n)}\right) + m \cdot (2K-m)\sqrt{N_{looks}\cdot \log N_{looks}}\right] \tag{5.2}$$

where N_{looks} is the number of looks utilized to compute the $K \times K$ sample covariance matrix of the resolution cells, and $\lambda_{i=1,\dots,K}(e,n)$ are the corresponding eigenvalues in descending order after denoising with Block Matching 3-D (BM3D) [35] to further reduce errors caused by phase noise. The model in (5.2) provides globally the best-performance, overcoming the Akaike information criterion (AIC) and the minimum description length (MDL) methods [138].

Assuming stripmap mode with a linear trajectory and negligible squint angle, the vector with the coordinates of a normal line (vector normal to the slant range-azimuth plane) $\boldsymbol{n}$ of γ_0^{3D} with origin at ground cell (e,n) can be approximated using

$$\boldsymbol{n}(e,n) = \left((e+\Delta e_i, n+\Delta n_i, h_i)\right)_{i=0,\dots,i_{amb}} \tag{5.3}$$

where Δe_i and Δn_i are the offsets in pixels of the 2-D displacement field, computed by cross-correlation between images $\gamma_0^{k,i}$ and $\gamma_0^{k,0}$ geocoded at heights $h_i = h_0 + i\Delta h$ and h_0 respectively, with $\Delta e_0 = \Delta n_0 = 0$.

The 3-D image, obtained by retaining the $p(e,n)$ strongest scatterers per normal line $\boldsymbol{n}$, takes the form:

$$I_{3D}(v) = \begin{cases} null, & O(v) = 0 \\ \gamma_0^{3D}(v), & otherwise \end{cases} \tag{5.4}$$

where v is a voxel at coordinates (e,n,h), γ_0^{3D} the backscatter obtained by means of maximum likelihood, and O is a 3-D matrix, referred to here as the binary occupancy matrix, whose elements take the value 0 or 1 indicating absence or presence of a scatterer respectively. $O(v)$ equals 1 if and only if the backscatter of the voxel $v \in \boldsymbol{n}(e,n)$ is one of the $p(e,n)$ strongest. Notice that $\sum_i O\big(\boldsymbol{n}(e,n)\big) = p(e,n)$.

Fig. 5.2 shows an example of a 2-D p matrix indicating the number of scatterers of a ground cell, and its possible occupancy matrix. Fig. 5.2 (c-d) illustrates the backscatter and the height of a real 3-D SAR image.

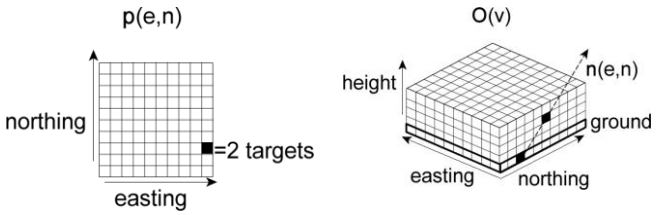

(a) Number of scatterers

(b) Occupancy matrix

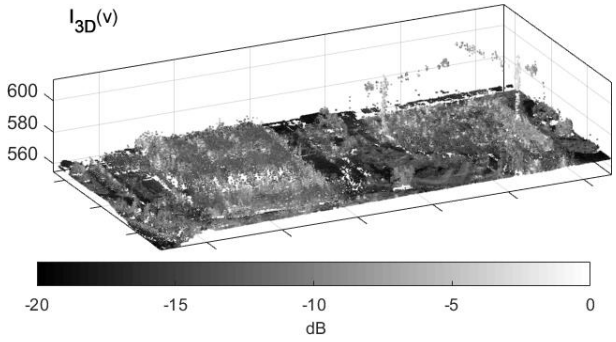

(c) Backscatter image

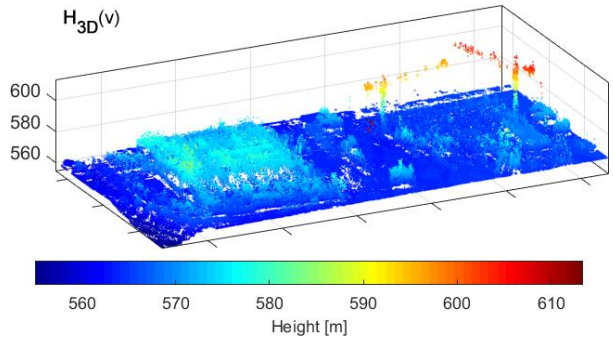

(d) Height image

Fig. 5.2 Tomographic SARimage processing. (a) Number of scatterers p. (b) 3-D occupancy matrix O. (c) Backscatter of a real 3-D SAR image. (d) Height of the SAR image in (c).

5.2.3 2-D and 3-D Combined SAR Change Detection

Typically, change detection is performed by applying a dissimilarity function to a reference and a test SAR image [23], followed by denoising [24, 25]. A change map is obtained after thresholding [3]. This map permits identifying changes and here contains three classes: no-change c_0, backscatter increase c_+, and backscatter decrease c_-. Here, we adapt this general framework for 3-D change detection applications. The proposed method consists of three stages described in the following (see Fig. 5.1).

5.2.3.1 First Stage: 2-D Change Detection for short targets

For short targets, a standard 2-D change detector is more reliable than a 3-D method as: 1) short objects introduce minimal layover and foreshortening, 2) TomoSAR single-look processing might be challenging with a small number of baselines [134, 136], 3) the 3-D image focusing chain is affected by additional sources of error, such as phase noise and decorrelation [139], and 4) the backscatter estimates of short targets degrades less in comparison to those of their 3-D image [136]. Note that for repeat-pass TomoSAR configurations, the number of tracks K is limited due to temporal and baseline decorrelation [140]. For single-pass configurations, limitations are caused by the design of the SAR system receiving chain [139].

In this work, we make use of the CD_MSQ method [120]. It exploits spatial information acquired by multisquint processing to reduce errors caused by image artifacts, such as sidelobes and ambiguities, and consists of three stages. First, an initial change map (ICM) is derived after denoising and thresholding the difference image (DI), obtained by subtracting the log-transformed data of the input single-look image pair. The DI is sensitive to noise, and performs poorly at detecting changes in distributed targets, such as trees or meadows; however, it performs well at detecting sharp changes common in urban environments [3], and enables detection of changes in the resolution space of the input SAR images. Moreover, in the log transform domain, the nature of the noise can be assumed to be Gaussian and additive. This property provides mathematical consistency with common denoising and thresholding schemes [3, 141, 142]. In contrast to [120], denoising is performed here by multi-looking using ensemble averaging with a sliding window. Thresholding is performed automatically via expectation maximization (EM) assuming a Gaussian distribution. In the second stage, we derive a new pair of images whose artifacts do not appear in the same image pixels as those of their respective single-looks using a multisquint framework (MSF). The MSF is configured so that the azimuth resolution and SNR of the resulting pair are sufficient to still detect changes of interest. An additional change map is computed from the new pair of images by repeating the operations of the first stage. Finally, a change map CM_{2D} is calculated after fusing the map from the second stage and the ICM.

5.2.3.2 Second Stage: 3-D Change Detection for tall targets

For tall objects, the tomographic processing disambiguates layover and provides significant information on their 3-D structure [134, 143]. The backscatter of tall targets is not degraded in comparison to that of the 2-D images, as targets are focused at their real 3-D position [136]. To detect changes, we utilized the 3-D difference image defined as follows:

$$DI_{3D}(v) = \begin{cases} -I_{3D}^{ref}(v), & O_{ref}(v) = 1, O_{test}(v) = 0 \\ I_{3D}^{test}(v), & O_{ref}(v) = 0, O_{test}(v) = 1 \\ I_{3D}^{test}(v) - I_{3D}^{ref}(v), & O_{ref}(v) = 1, O_{test}(v) = 1 \\ null, & otherwise \end{cases} \tag{5.5}$$

where I_{3D}^{ref} and I_{3D}^{test} are γ_0 of the reference and test 3-D SAR images taking their form from (5.3). From (5.4) one observes that DI_{3D} is sensitive to the occupancy of the voxels, which depends on phase and amplitude noise, among other factors [144]. The phase noise can alter the 3-

D position of the target and the amplitude noise its backscatter. The first two conditions in (5.4) indicate that the detection of changes caused by appearing or disappearing targets depends only on the backscatter of the target itself; i.e. change detection reduces to target detection. This can lead to misdetections of tall targets with dark backscatter. Information on height difference was considered to reinforce the performance of the DI_{3D}. In a similar fashion as with a LiDAR point cloud, we used the Hausdorff distance [145], employing a cylindrical neighborhood instead of a spherical one to emphasize changes along the vertical axis. Let us define the 3-D matrices H_{3D}^{ref} and H_{3D}^{test} as the reference and test height images of the form

$$H_{3D}(v) = \begin{cases} null, & O(v) = 0 \\ h = h_0 + i\Delta h, & otherwise \end{cases} \tag{5.6}$$

The Hausdorff distance d_{ref} of the reference 3-D image was computed with the following procedure:

1. $\forall\, v = (e, n, h) \in H_{3D}^{ref}$:
2. $S = \left\{ v^* = (e^*, n^*, h^*) \in H_{3D}^{test} : \sqrt{(e - e^*)^2 + (n - n^*)^2} \leq \rho_{max} \right\}$
3. $\left(S \neq \emptyset \rightarrow \mathrm{d}_{ref}(v) = \max_{v^* \in S}(h - h^*)\right) \wedge \left(S = \emptyset \rightarrow \mathrm{d}_{ref}(v) = 0\right)$

where, v and v^* are voxels at coordinates (e, n, h) and (e^*, n^*, h^*) of the reference and test 3-D images defined in (5.5) respectively, and ρ_{max} the maximum radius of the cylinder defining the neighborhood. Since the Hausdorff distance is not symmetric, $\mathrm{d}_{test}(v)$ was computed by exchanging the role of the reference and test height images in the previous procedure. The height difference can then be calculated with

$$\Delta H_{3D}(v) = \begin{cases} -\mathrm{d}_{ref}(v), & O_{ref}(v) = 1, O_{test}(v) = 0 \\ \mathrm{d}_{test}(v), & O_{ref}(v) = 0, O_{test}(v) = 1 \\ \left(\mathrm{d}_{test}(v) - \mathrm{d}_{ref}(v)\right)/2, & O_{ref}(v) = 1, O_{test}(v) = 1 \\ null, & otherwise \end{cases} \tag{5.7}$$

Note that the occupancy of ΔH_{3D}, is identical to that of DI_{3D} defined in (5.4), unless $S \neq \emptyset$ in step 2 of the Hausdorff distance procedure for a voxel v.

We simplify the image in (5.4) by discarding the bottom layers; i.e. $DI_{3D}^{tall}(e, n, h_i) = DI_{3D}(e, n, h_i), i = i_{short} + 1, \ldots, i_{amb}$, being $h_0 + (i_{short} + 1) \cdot \Delta h = h_{short} + \Delta h$ the minimum height for tall targets. ΔH_{3D}^{tall} is calculated in similar fashion with the image in (5.6). This step eases selection of the size of a neighborhood, referred to as the scale parameter [146], required for further processing.

Information in DI_{3D}^{tall} and ΔH_{3D}^{tall} is combined with a CRF. Here, we adopt the Markov random field model in [3], and modify it to account for a 3-D spherical neighborhood based on the Euclidean distance and the additional potential associated to ΔH_{3D}^{tall}. The probability of assigning a voxel of DI_{3D}^{tall} to a class $cl = \{c_0, c_+, c_-\}$ given the classes in a neighborhood $\mathcal{N}$ can be calculated by minimizing the energy function of the CRF model:

$$\begin{aligned} U\left(DI_{3D}^{tall}, \Delta H_{3D}^{tall}, cl\right) \\ = \sum_{i=1}^{\xi_t} \Big[& U_{data}\left(DI_{3D}^{tall}(v_i) | cl(v_i)\right) + U_{\mathcal{N}}\left(cl(v_i) | \{cl(v_j), v_j \in \mathcal{N}(v_i)\}\right) \\ & + U_{\mathcal{N}\Delta H}\left(cl(v_i) | \{cl_{\Delta H}(v_j), v_j \in \mathcal{N}(v_i)\}\right) \Big] \end{aligned} \tag{5.8}$$

where v_i denotes the *i*-th non-null voxel of DI_{3D}^{tall}, $\mathcal{N}(v_i)$ is a set of $\xi_i = card(\mathcal{N}(v_i))$ voxels in the neighborhood of v_i, U_{data} the clique potential accounting for the statistics of the DI_{3D}^{tall} assuming conditional independence [3], $U_{\mathcal{N}}$ the clique describing the inter-voxel class dependence, $U_{\mathcal{N}\Delta H}$ the clique accounting for the inter-voxel class dependence conditioned to ΔH_{3D}^{tall}, and ξ_t the number of non-null voxels in DI_{3D}^{tall}. To reduce the impact of arbitrary parameterizations and to avoid introducing *a priori* knowledge of the scenes, we assumed that the density distribution of the DI_{3D}^{tall} follows a Gaussian distribution. In that case U_{data} can be derived from:

$$U_{data}\left(DI_{3D}^{tall}(v)|cl(v)\right) = \frac{1}{2} ln\left|2\pi\sigma_{cl(v)}^2\right| + \frac{1}{2\sigma_{cl(v)}^2}\left(DI_{3D}^{tall}(v) - \mu_{cl(v)}\right)^2 \tag{5.9}$$

with $\sigma_{cl(v)} \in \{\sigma_{c_0}, \sigma_{c_+}, \sigma_{c_-}\}$ and $\mu_{cl(v)} \in \{\mu_{c_0}, \mu_{c_+}, \mu_{c_-}\}$ being the estimates of the standard deviation and mean of the no-change c_0, positive change c_+ and negative change c_- classes. Initial estimates of σ_{cl} and μ_{cl} in (5.9) can be computed from the denoised DI and the change map CM_{2D} derived in the first stage of the proposed method using:

$$\mu_{cl} = \frac{\sum_{i=1}^{M}\left[DI(m_i)\cdot\delta\left(CM_{2D}\left(cl(m_i)\right), cl\right)\right]}{\sum_{i=1}^{M}\left[\delta\left(CM_{2D}\left(cl(m_i)\right), cl\right)\right]} \tag{5.10}$$

and

$$\sigma_{cl} = \sqrt{\frac{\sum_{i=1}^{M}\left(DI(m_i)\cdot\delta\left(CM_{2D}\left(cl(m_i)\right), cl\right) - \mu_{cl}\cdot\delta\left(CM_{2D}\left(cl(m_i)\right), cl\right)\right)^2}{\sum_{i=1}^{M}\left[\delta\left(CM_{2D}\left(cl(m_i)\right), cl\right)\right] - 1}} \tag{5.11}$$

where *M* is the total number of pixels, m_i the *i*-th pixel of the denoised DI, and $cl \in \{c_0, c_+, c_-\}$. These parameters depend on the scene and characteristics of the SAR images provided by the sensor involved. Initial estimates of σ_{cl} and μ_{cl} can also be obtained by applying EM to the DI_{3D}.

The potential of the inter-voxel class dependence is given by:

$$U_{\mathcal{N}}\left(cl(v_i)|\left\{cl\left(v_j\right), v_j \in \mathcal{N}(v_i)\right\}\right) = -\sum_{j=1}^{\xi_i}\beta_1\cdot\delta\left(cl(v_i), cl(v_j)\right) \tag{5.12}$$

with being β_1 the shape parameter controlling the influence of the classes of the neighbors, and

$$\delta(cl(v), cl(v^*)) = \begin{cases} 1, & cl(v) = cl(v^*) \\ 0, & otherwise \end{cases} \tag{5.13}$$

Finally, we define the potential conditioned to changes given by ΔH_{3D}^{tall} as:

$$U_{\mathcal{N}\Delta H}\left(cl(v_i)|\left\{cl_{\Delta H}\left(v_j\right), v_j \in \mathcal{N}(v_i)\right\}\right) = -\sum_{j=1}^{\xi_i}\beta_2\cdot\delta\left(cl(v_i), cl_{\Delta H}(v_j)\right) \tag{5.14}$$

where β_2 is the shape parameter tuning the influence of ΔH_{3D}^{tall}, and $cl_{\Delta H}(v^*)$ the class assigned to the voxel v_i^* according to ΔH_{3D}^{tall}. The term $\delta\left(cl(v_i), cl_{\Delta H}(v_j)\right)$ is obtained with (5.10), and $cl_{\Delta H}(v)$ with:

$$cl_{\Delta H}\left(v_j\right) = \begin{cases} c_+, & \left|\sigma_{\Delta H_{3D}}\right| \le \Delta H_{3D}^{tall}(v_j) \\ c_-, & \Delta H_{3D}^{tall}(v_j) \le -\left|\sigma_{\Delta H_{3D}}\right| \\ c_0, & otherwise \end{cases} \tag{5.15}$$

where $\sigma_{\Delta H_{3D}}$ is the standard deviation of all non-null elements of ΔH_{3D} in (5.6). Notice that if $\beta_2 = 0$ then the CRF model in (5.7) reduces to a Markov random field [147]. Finally, (5.7) is solved by means of the iterated conditional modes algorithm in [148], yielding a 3-D change map CM_{3D}^{tall}.

5.2.3.3 Third Stage: Fusion and post-processing

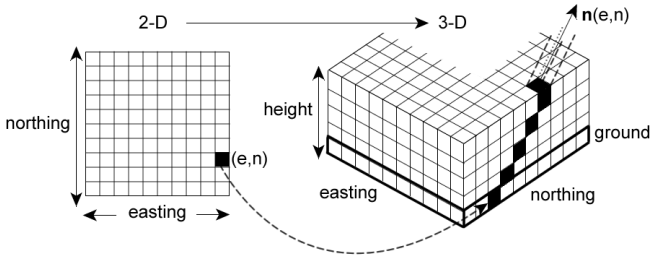

Fig. 5.3 Ground-height proxy: 2-D to 3-D image conversion.

The change map CM_{2D} calculated in the first stage is transformed into a 3-D map with the ground-height proxy given by $\boldsymbol{n}(e,n)$ in (5.2):

$$CM_{3D}^{short}(e+\Delta e_i, n+\Delta n_i, h_0+i\Delta h) = CM_{2D}(e,n,h_0), i=0,\dots,i_{short} \tag{5.16}$$

A scheme of the 2-D to 3-D image conversion system used in this work is depicted in Fig. 5.3. We remove false alarms with

$$CM_{3D}^{short}(v) = \begin{cases} c_0, & \left(O_{ref}(v)=0\right) \wedge \left(O_{test}(v)=0\right) \\ CM_{3D}^{short}(v), & otherwise \end{cases} \tag{5.17}$$

By applying (5.14) we ensure that voxels that are null in the 3-D image pair are classified as no-change. A change map CM_{3D} is computed after merging CM_{3D}^{short} and CM_{3D}^{tall} as follows:

$$CM_{3D}(e,n,h_i) = \begin{cases} CM_{3D}^{short}(e,n,h_0+i\Delta h), & i \le 0,\dots,i_{short} \\ CM_{3D}^{tall}(e,n,h_0+i\Delta h), & i > i_{short} \end{cases} \tag{5.18}$$

Finally, for each normal line $\boldsymbol{n}$ of the change map CM_{3D} in (5.15) we remove false alarms assumed to be caused by a failure in the inversion of the TomoSAR processing method when a ground scatterer is resolved in only one of the images, using:

$$\left(\left(\left(O_{ref}(v_0)+O_{test}(v_0)\right)=1\right) \wedge \left(\sum_{i=0}^{i_{amb}} O_{ref}(\boldsymbol{n}) \ge 1\right) \wedge \left(\sum_{i=0}^{i_{amb}} O_{test}(\boldsymbol{n}) \ge 1\right), v_i \in \boldsymbol{n}\right) \rightarrow \left(CM_{3D}(\{v_i \in \boldsymbol{n},\ i=0,\dots,i_{min}\}) = c_0\right) \tag{5.19}$$

with

$$i_{min} = \begin{cases} \min_{i,i=1,\dots,i_{amb}}\left(O_{ref}(v_i)=1\right)-1, & O_{ref}(v_0)=0 \\ \min_{i,i=1,\dots,i_{amb}}\left(O_{test}(v_i)=1\right)-1, & otherwise \end{cases} \tag{5.20}$$

being v_0 and v_i the voxels at coordinates (e,n,h_0) and (e,n,h_i) of the line $\boldsymbol{n}$. Fig. 5.4 shows a voxel on the ground of a slice of the test SAR image causing a potential false alarm.

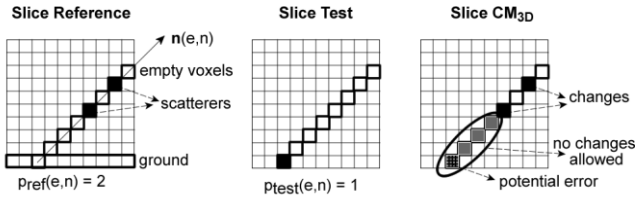

Fig. 5.4 Removal of false alarms caused by potential differences in the information contained in the reference and test 3-D SAR images.

5.3 Experimental Results

5.3.1 Sensor, Data and Test Site

TABLE 5.1
DESCRIPTION OF THE USED MEMPHIS DATA SET

Carrier frequency	35 GHz (Ka-band)
Bandwidth	900 MHz (frequency agile)
PRF	1500 Hz
Average airplane velocity	77 m/s
Airplane altitude a.g.l.	300-1000 m
Antenna tilt angle	20°-35°
Slant range resolution, δ_r	0.167 m
Azimuth resolution, δ_a	0.082 m
Baselines	0.0055 m , 0.165 m, 0.275 m
Mid-Range	1547 m
Depression angle	30°

The images were acquired with Fraunhofer FHR's MEMPHIS sensor [95] over Hinwil (Switzerland) and Memmingen (Germany). The sensor was equipped with four receiving antennas, enabling single-pass multibaseline cross-track interferometry. Table 5.1 lists the main system parameters. The Rayleigh normal resolution δ_n was computed using the largest slant range of the corresponding image patch, assuming that the normal aperture length is given by the largest baseline listed in Table 5.1. The data was focused with a Graphic Processor Unit-based TDBP processor [115]. Analysis of the signatures of corner reflectors deployed in the area of interest showed geolocation errors of a few centimeters [149]. Radiometric calibration was performed with the procedure reported in [28]. Table 5.2 summarizes some characteristics of the image pairs utilized in this work. The incident angle is given as the average incident angle of the image patch shown. The value of the ambiguity height h_{amb} was computed with the largest slant range of the image patch and its corresponding incident angle. Images in Pairs 1 and 2 belong to different areas of the same data set. They were recorded in a medium density urban area with construction cranes present and short term changes related to human activity. Pair 3 was recorded near a civilian airport with long-term construction works present.

TABLE 5.2
DESCRIPTION OF OF THE IMAGE PAIRS

Image		Heading Angle	Mean Incident Angle	Slant Range Extent	Maximum Ambiguity Height	Minimum Rayleigh Normal Resolution	Date	Time
Pair1	HIN1a	92°	67°	260 m	278.17 m	30.05 m	17/06/2009	12:42:02
	HIN2a	92°	66°	280 m	272.23 m	29.63 m	17/06/2009	12:57:17
Pair2	HIN1b	92°	67°	280 m	274.25 m	29.72 m	17/06/2009	12:42:02
	HIN2b	92°	66°	280 m	267.42 m	29.07 m	17/06/2009	12:57:17
Pair3	MEM1	244°	59°	230 m	219.09 m	24.85 m	11/05/2011	13:21:54
	MEM2	231°	56°	250 m	224.81 m	23.71 m	07/11/2012	13:08:07

5.3.2 Description of the experiments

The 3-D images were focused after tomographic processing of the signals recorded with the four receiving antennas in single-pass mode; i.e. K = 4. With this configuration, we assumed absence of temporal and baseline decorrelation. For 3-D image focusing, we set $W(\theta) = 1$ in (5.1). In this work, the tomographic reconstruction involved multi-look processing, performed by ensemble averaging the covariance matrices within a sliding window of size $N_{looks} = 5 \times 5$ pixels, yielding a pixel spacing of 0.5 m in northing and easting. Adaptive covariance matrices estimation methods reported in [150] and [151] were not used because of computational considerations; however, we applied BM4D to reduce errors caused by phase noise. We did not applied diagonal loading of the covariance matrices in any step of the tomographic processing chain. The height sampling spacing $\Delta h < \delta_n$ was set to 0.5 m, trading off the precision of the geolocation of the scatterers and the computation time of the 3-D image focusing chain. Notice that by using spectral estimation methods, one can achieve better normal resolution δ_n than that listed in Table 5.2. Here, $\delta_n \approx 3$ m was chosen based on simulations of maximum likelihood processing of MEMPHIS data [152].

If the height of the tallest target of the imaged volume $h_{tallest}$ fulfills $h_{tallest} < h_{amb}$, then the computation time required for (5.1) is reduced using $h_{amb} = h_{tallest} + \Delta h$. The value of $h_{tallest}$ can be obtained based on *a priori* knowledge of the scene or from a digital surface model (DSM). Here, $h_{amb} = 50$ m, based on the value of $h_{tallest}$ computed from a DSM of the area of interest. Note that the theoretical value of h_{amb} of the tomographic configuration should be large enough so that changes caused by targets with a comparable height can be detected. The number of layers in height of each 3-D image was then given by $i_{amb} = h_{amb}/\Delta h + 1$.

For CD-MSQ, the input 2-D images, $\gamma_0^{1,0}$ from (5.1), were obtained using the data from the master channel ($k = 1$). In contrast to [120], the input images represent the *gamma nought* γ_0 backscatter instead of the radar brightness or *beta nought* β_0 backscatter because γ_0 is less sensitive to the acquisition geometry [153]. Note that $\gamma_0 = \beta_0 \cdot tan\theta_e$, where the radar brightness β_0 is defined as the ratio between the scattered and incident power at ground level per resolution cell, and θ_e is the incident angle. The MSF in CD-MSQ was configured to yield images with an azimuth resolution of $2\delta_a$, with δ_a being the azimuth resolution of the single-look. The spatial filter $W(\theta)$ in (5.1) has an angular selectivity bandwidth $\Delta\theta = 0.25\theta_a$, with θ_a being the azimuth beamwidth of the antenna pattern in reception. The focused image squints did not overlap in the azimuth angle domain, and thus summing the resulting four bandpass squints yield the single-look. The value of $2\delta_a$ was chosen such that the changes caused by the smallest targets of interest, here considered to be vehicles, could still be detected with the corresponding 2-D images. For image denoising purposes, CD-MSQ employs here a 2-D moving average filter of size $N_{looks} = 5 \times 5$ pixels, similar to multi-look processing. As a result, the 2-D SAR images and corresponding change maps have a pixel spacing of 0.5 m in northing and easting. In the third stage of CD-MSQ, we performed fusion at the pixel level to obtain the final change map [120].

The 3-D images represent the backscatter γ_0^1 obtained by back-projection of the data from the master channel ($k = 1$) using (5.1). CD-MSQ utilizes as input the images $\gamma_0^{1,0}$. This permits direct comparison between 2-D and 3-D change detectors, because the backscatter of the respective images are obtained using the same pulse compression methods; i.e. without the influence of the pulse compression method applied in the normal direction.

The value of h_{short} was set to 3 m, assuming that the 3-D images of vehicles, considered to be the shortest targets causing changes of interest, did not offer improvements in change detection in comparison to the corresponding 2-D images. Selection of this value was based on the following: 1) for spaceborne and airborne SAR, vehicles can be assumed to introduce negligible layover, and 2) if 3-D single-look processing cannot be performed, then those targets can be

better resolved in the 2-D domain. Values of $h_{short} > 0$ m ease the selection of the scale parameter of the CRF model, since DI_{3D}^{tall} and ΔH_{3D}^{tall} do not contain scatterers at the ground level. By extension $i_{short} = h_{short}/\Delta h$.

For the cylindrical neighborhood of the Hausdorff distance we select $\rho_{max} = 10$ m to account for the average size of tall targets in medium density urban areas.

We consider evaluation of the following two scenarios: a) the approach does not exploit height information; i.e. $\beta_1 = 1$ and $\beta_2 = 0$ or b) the method exploits both backscatter and height information; i.e. $\beta_1 = \beta_2 = 1$. In this work β_1 in (5.12) and β_2 in (5.14) are assumed to be class-independent.

The following two neighborhood parameterizations were considered for solving (5.8): a) *fixed*, the voxels have the same amount of neighbors; i.e. $\xi_i = \xi, i = 1, \dots, \xi_t$, and b) *varying*, the scale parameter is computed individually for each voxel with the value minimizing the eigenentropy [146].

The performance of the combined change detector was compared to that of: 1) the 2-D change detector CD-MSQ reported in [120], 2) the approach resulting after thresholding the entire DI_{3D} in (5.5) with EM assuming a Gaussian distribution, referred to here as CD-DI_{3D}, and 3) the method resulting from (5.15), referred to here as CD-HD typically used with LIDAR point clouds. We also evaluate the methods with the images derived after InSAR processing, resulting when retaining the strongest scatterer per normal line.

A synthetic reference 3-D image was manually labelled for numerical evaluation. This reference was projected on to the ground, inverting (5.3), to obtain the corresponding 2-D synthetic reference. Quality assessment was based on the kappa coefficient κ [116]. For the combined approach, we list the mean μ_κ of the κ coefficients calculated by varying the scale parameter ξ_i with values ranging from 10 to 500 voxels. The standard deviation σ_κ was calculated to analyze the sensitivity of the methods to the scale parameter. We also studied the ability of the approaches to detect changes caused by short and tall targets. For this purpose, we computed a curve, referred to here as a kappa profile, representing the kappa coefficient evaluated at each height above ground $h_0 + i\Delta h, i = 0, \dots i_{amb}$ of the 3-D change maps. For CD-MSQ, a pseudo kappa profile was computed after transforming the 2-D change map into a 3-D map using (5.16) and (5.17) with $i = 0, \dots, i_{amb}$. Note that this transformation might bring potential errors from the 3-D processing chain into the transformed map.

5.3.3 Results

The data sets listed in Table 5.2 were used to evaluate the performance of the combined method. In the following, we present the results from the three image pairs, showing the performance of the methods for detection of changes caused by diverse man-made targets, with different temporal resolution. Fig. 5.5(a) shows the 3-D synthetic labelled reference overlaid on the 2-D reference SAR image HIN1a. This image shows the changes with voxels colored in red and green indicating targets that left or entered the area of interest respectively. In Fig. 5.5, patches 1 to 5 indicate changes caused by cars. A change caused by the rotational movement of the jib of a crane (slewing) is marked in patch 6.

Table 5.3 lists the κ coefficient and μ_κ of the maps calculated with the different methods. The combined approach improved the κ coefficient by a factor two in comparison to CD-MSQ or CD-DI_{3D}. Comparison of the performance of the combined variants reveals that when both backscatter and height difference information are utilized; i.e. β_2 was set to 1; the κ coefficient improved by a factor 1.2. Best results were achieved when the scale parameter was calculated individually for each voxel.

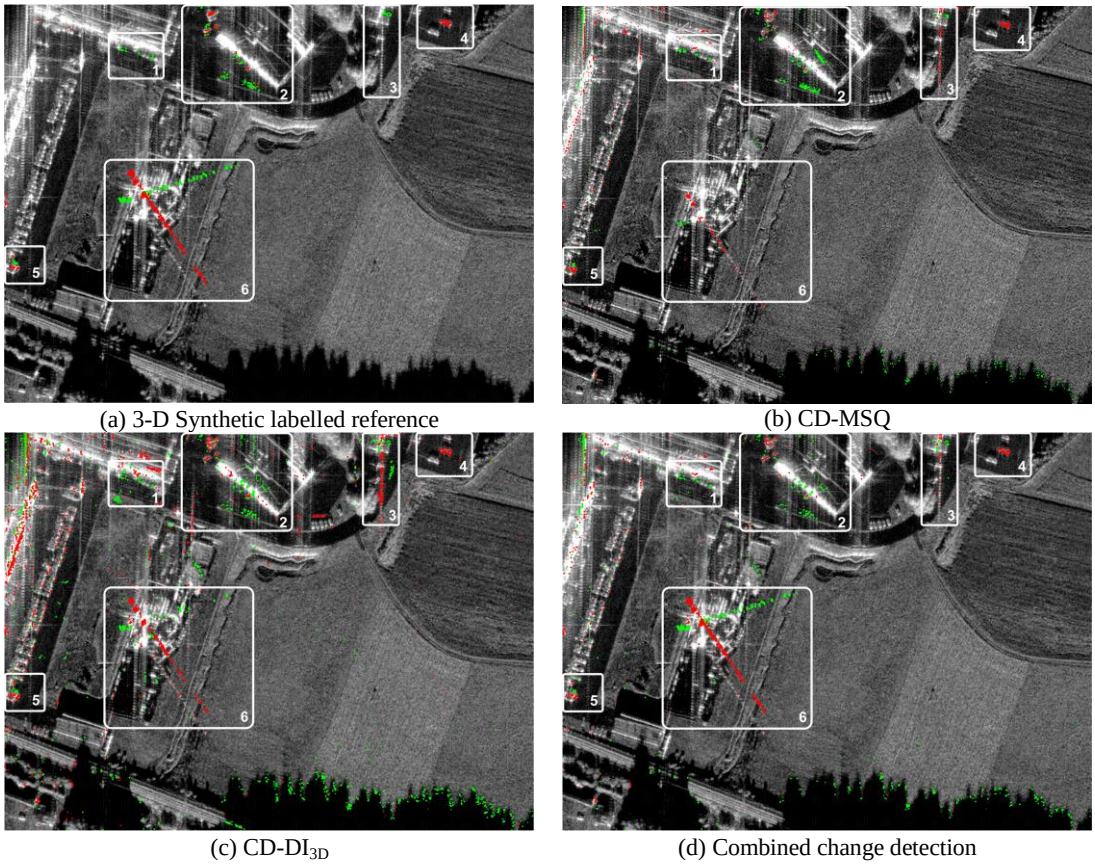

(a) 3-D Synthetic labelled reference (b) CD-MSQ

(c) CD-DI_{3D} (d) Combined change detection

Fig. 5.5 Overlaid change maps computed with the pair HIN1a and HIN2a. (a) 3-D Synthetically labelled reference overlaid on the reference 2-D SAR image. (b) 2-D change map overlaid on the reference SAR image. (c) Top view of the map derived with CD-DI_{3D} overlaid on the 2-D reference image. (d) Top view of the overlaid change map derived with combined change detection with β_2 equal to 1 and a maximum ξ_i of 200 voxels. Pixels marked in red/green indicate that targets left or entered the area of interest.

TABLE 5.3
PERFORMANCE METRICS FOR THE PAIR HIN1A-HIN2A

Input	**Method**			κ
2-D	CD-MSQ			0.1852
3-D	CD-DI_{3D}			0.2270
	CD-HD			0.1011
	Combined	β_2	ξ_i	μ_κ
		0	Fixed	0.4399
		0	Varying	0.4748
		1	Fixed	0.5708
		1	Varying	0.5862

Fig. 5.5 (b) illustrates the change map, calculated with CD-MSQ, overlaid on the 2-D amplitude SAR image HIN1a. Pixels in green/red indicate that targets entered or left the area of interest. Visual inspection shows that the method detects the changes caused by cars, marked in rectangle 1 to 5. However, the change caused by the slewing of the crane, marked in patch 6, is partially detected. Fig. 5.5 (c) shows the top view of the 3-D map computed with CD-DI_{3D}, overlaid on the 2-D amplitude image HIN1a. The change caused by the crane is more perceptible, but there are more errors associated to image artifacts in patch 3.

The overlaid 3-D map calculated with combined change detection when setting β_2 to 1 and a varying neighbourhood scheme with a maximum ξ_i of 200 voxels is depicted in Fig. 5.5 (d). The maximum value of ξ_i corresponds to the configuration yielding the best κ coefficient. Changes caused by cars were detected with accuracy similar to the previous two approaches. Visual inspection of the patch 3 in Fig. 5.5 (b) and (d) revealed that the 3-D map had fewer false alarms caused by range sidelobes. Comparison of the methods using 3-D SAR images indicated that changes caused by short targets were detected better with the combined variants. Based on Fig. 5.5, the detection of the movement of the crane is more perceptible in the change map derived with the combined variant. Fig. 5.6 depicts the kappa profile obtained with the different change detection methods. For changes caused by short targets, best performance was obtained with CD-MSQ, while CD-HD performed worst. One can observe that the combined method resulting when β_2 was set to 1 provided the best performance for changes caused by tall targets. CD-HD performance came in second place. Note that the change maps illustrated in Fig. 5.5 had false alarms related to the shadow cast by a forest area in the southernmost part of the images.

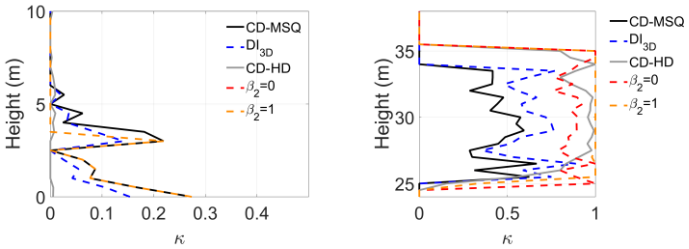

Fig. 5.6 Kappa profile of the image pair HIN1a and HIN2a. a) heights below 10 meters from the ground. b) heights above 24 meters from the ground. For the combined methods, the maximum scale parameter ξ_i was 200 voxels.

Fig. 5.7 (b) illustrates the overlaid change map, calculated with CD-MSQ. Similar to the previous example, visual inspection showed that the method detected the changes caused by cars, indicated by rectangles 1 to 3, but partially missed the change caused by the crane in patch 4. Fig. 5.7 (c) shows a part of the commercial area of Hinwil. Patches 1 to 3 mark changes caused by cars and rectangle 4 changes caused by a crane. The corresponding kappa coefficients are listed in Table 5.4. The combined approaches improve the κ coefficient by a factor two in comparison to CD-MSQ or CD-DI_{3D}. The method CD-HD performed worst. However, the κ delivered by the combined methods did not improve significantly when β_2 was set to 1.

TABLE 5.4
PERFORMANCE METRICS FOR THE PAIR HIN1B-HIN2B

Input	**Method**			κ
2-D	CD-MSQ			0.1588
3-D	CD-DI_{3D}			0.1377
	CD-HD			0.0396
	Combined	β_2	ξ_i	μ_κ
		0	Fixed	0.3356
		0	Varying	0.3413
		1	Fixed	0.3482
		1	Varying	0.3037

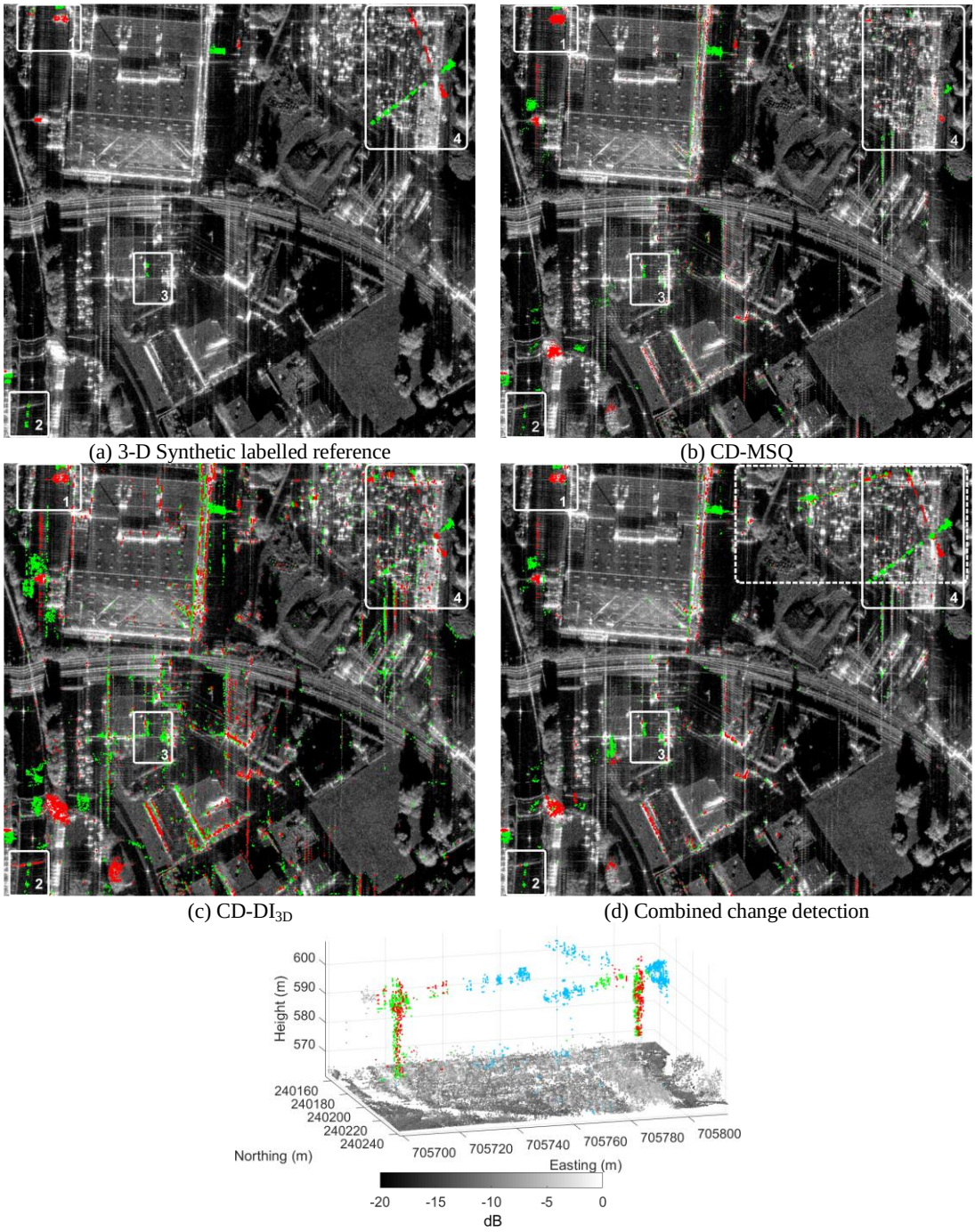

(a) 3-D Synthetic labelled reference

(b) CD-MSQ

(c) CD-DI_{3D}

(d) Combined change detection

(e) Comparison of the combined variants

Fig. 5.7 Overlaid change maps obtained with the pair HIN1b and HIN2b. (a) 3-D synthetically labelled reference overlaid on the reference 2-D SAR image. (b) 2-D change map overlaid on the reference SAR image. (c) Top view of the change map derived with CD-DI_{3D} overlaid on the 2-D reference SAR image. (d) Top view of the overlaid change map derived with combined change detection using β_2 equal to 1 and a maximum ξ_i of 240 voxels. (e) Detail of the overlaid change map indicated by a dashed rectangle in subfigure c). Voxels marked in red/green indicate that targets left or entered the area of interest. Voxels marked in blue indicate changes that are detected with the two combined approaches; i.e. when β_2 was set to zero and one.

Fig. 5.7 (c) shows the overlaid 3-D change map calculated with CD-DI_{3D}, and Fig. 5.7 (d) the map obtained with combined change detection β_2 set to 1 and a varying neighborhood pa-

rameterization scheme with a maximum ξ_i of 240 voxels. Visual inspection of the two maps indicated that the changes caused by the cars in patch 1 and 2 were detected with similar accuracy. However, the false alarm, in red, caused by a moving car in patch 2 was only partially present in the map calculated with the combined approach. One observes that the change map obtained with CD-DI_{3D} has more false alarms, mainly located at roof-edges and the walls of buildings, in comparison to that from the combined variant. The change caused by the slewing of the crane, marked in patch 4, was partially detected with CD-DI_{3D}, as it can be observed in Fig. 5.7 (b) and (c). Fig. 5.8 depicts the kappa profiles obtained with the different methods, pointing out that the combined variants outperformed the other approaches. CD-HD had the worst performance in detecting changes caused by short targets. The combined approach, resulting when β_2 was set to 1 performed worse than when β_2 was zero for changes caused by tall targets. To provide insight into this result, Fig. 5.7 (e) shows a detail of the change map of the area indicated by a dashed rectangle in Fig. 5.7 (d). There, we observe the presence of two cranes, with the western one causing a real change. Blue voxels mark areas where both combined variants detected changes, whereas voxels in red or green mark areas where changes were only detected when β_2 was equal to 1. The rotational movement of the crane was more perceptible when β_2 was set to 1; however; the corresponding change map had false alarms in the tower mast of the crane and the eastern crane. The kappa profiles of the combined methods in Fig. 5.8 (b), support with numbers the previous observations.

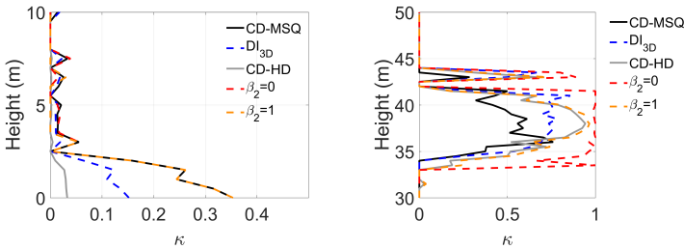

Fig. 5.8 Kappa profile of the image pair HIN1b and HIN2b. a) heights below 10 meters from the ground. b) heights above 30 meters from the ground. For the combined methods, the maximum scale parameter ξ_i was 240 voxels.

Fig. 5.9 (a) shows the 3-D synthetic labelled reference of the pair MEM1 and MEM2. Changes were caused by cars, indicated by rectangles 1 to 4, and a new building, highlighted in green in the center of the image. Table 5.5 lists the κ coefficient of the maps calculated with the different methods. By exploiting backscatter and height difference information, κ improved by a factor 1.15 in comparison to that obtained with CD-HD. Similar to previous examples, best results were given when the neighborhood size was computed individually for each voxel.

TABLE 5.5
PERFORMANCE METRICS FOR THE PAIR MEM1-MEM2

Input	**Method**			κ
2-D	CD-MSQ			0.0604
3-D	CD-DI_{3D}			0.2058
	CD-HD			0.3872
	Combined	β_2	ξ_i	μ_κ
		0	Fixed	0.1556
		0	Varying	0.1784
		1	Fixed	0.4462
		1	Varying	0.4479

Fig. 5.9 (b-d) illustrates the overlaid map computed with CD-MSQ, CD-DI_{3D} and the combined variant respectively. Comparison of the changes caused by cars, marked in patches 1 to 4,

indicated that the maps given from the different methods had abundant misdetections, independently of whether these changes occurred on grass, as in patch 1, or asphalt, as in patches 2, 3 and 4. Based on Fig. 5.10 (a), changes caused by short targets were better detected with the combined variants. The new building in the center of the image had an average height of 10 meters.

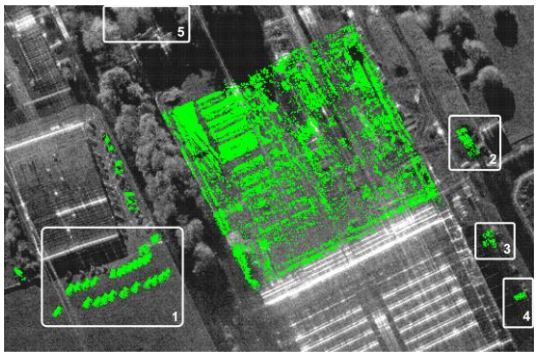

(a) 3-D Synthetic labelled reference

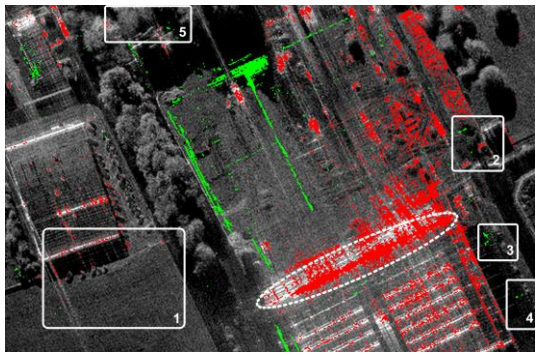

(b) CD-MSQ

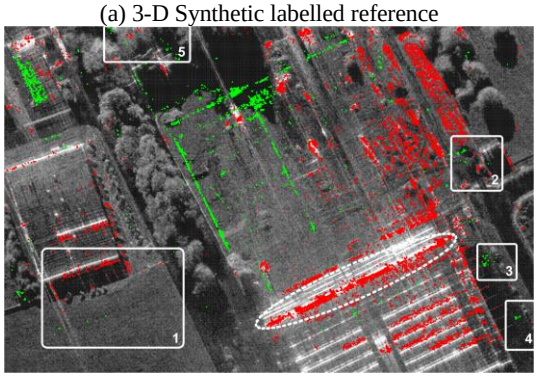

(c) CD-DI_{3D}

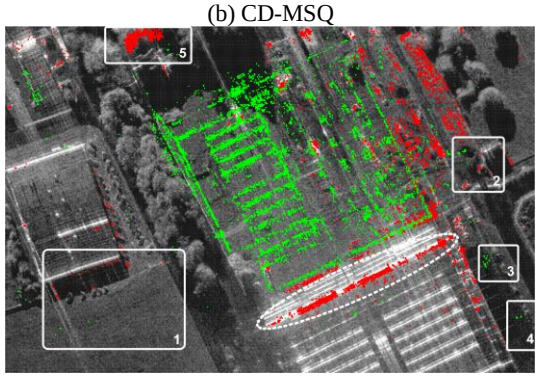

(d) Combined change detection

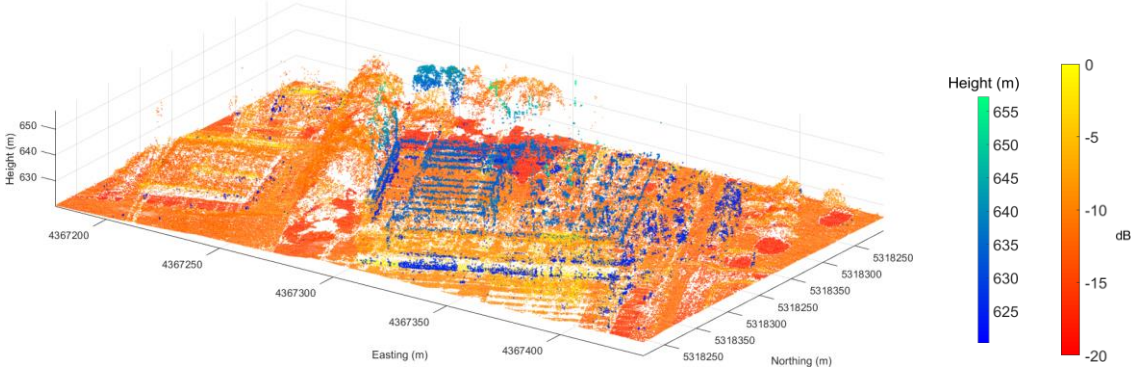

(e) Fusion of the reference 3-D SAR image and change map. Green-blue voxels show the height of the changes.

Fig. 5.9 Overlaid change maps obtained with the pair MEM1 and MEM2. (a) 3-D Synthetically labelled reference overlaid on the reference 2-D SAR image. (b) 2-D change map overlaid on the reference SAR image. (c) Top view of the change map derived with CD-DI_{3D} overlaid on the 3-D reference SAR image. (d) Top view of the overlaid map derived with combined change detection using β_2 equal to 1 and a maximum ξ_i of 140 voxels. Pixels marked in red/green indicate that targets left or entered the area of interest. (e) Fusion of the reference SAR image and the change map (green-blue voxels) obtained from combined change detection.

Visual inspection of the maps in Fig. 5.9 revealed that the combined approach performed best. From the κ profile in Fig. 5.10 (b), the combined method resulting when β_2 was zero yielded moderate results for changes caused by tall targets. The area in a dashed ellipse, shown in Fig. 5.9 (b-d) encloses the wall of a building. The associated changes were false alarms, as

the wall fell in the shadow area of the test SAR image after construction of the nearby building. The associated false alarms, shown in red, were more widespread in the map derived with CD-MSQ in comparison to those calculated with the methods using 3-D images. Fig. 5.9 (e) shows the reference SAR image and the change map (green-blue voxels indicating the height) where one can better observe the change of the building and some false alarms caused by the canopy of the trees in patch 5.

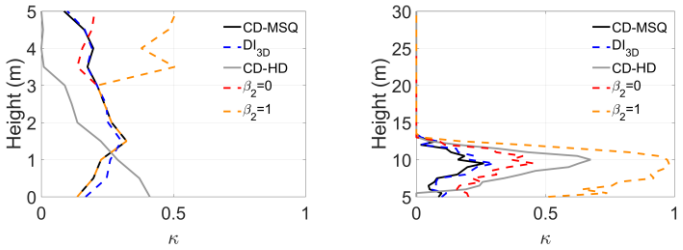

Fig. 5.10 Kappa profile of the image pair MEM1 and MEM2. a) heights below 5 meters from the ground. b) heights above 5 meters from the ground. For the combined methods, the maximum scale parameter ξ_i was 140 voxels.

Table 5.6 lists a global evaluation of the methods, computed by a weighted average of the indicators in Table 5.3 to Table 5.5. For comparison purposes, we include the results obtained with the corresponding 2½-D images derived after InSAR processing. The combined approach provided best results when β_2 was set to one. However, the kappa coefficient worsened using a varying scale configuration in comparison to that using a fixed scale parameter. This can be explained due to the differences in false alarms caused by the western crane of the pair HIN1b-HIN2b shown in Fig. 5.7 (e). Comparison of the kappa coefficients showed that the change detection methods performed best when the 3-D SAR images were used rather than the equivalent 2½-D images. The global value of σ_κ was 0.0686 and 0.0230 with a fixed neighborhood size and β_2 set to zero and one respectively. These values reduced by approximately a factor two when utilizing a varying scale parameter, indicating that the neighborhood parameterization scheme was less sensitive to ξ_i. For the InSAR scenario, the values of σ_κ were similar to those obtained when using the 3-D SAR images.

TABLE 5.6
GLOBAL PERFORMANCE METRICS OF THE CHANGE DETECTORS

Input	**Method**			κ
2-D	CD-MSQ			0.1501
2½-D	CD-DI_{3D}			0.1595
	CD-HD			0.1208
	Combined	β_2	ξ_i	μ_κ
		0	Fixed	0.2825
		0	Varying	0.3217
		1	Fixed	0.4003
		1	Varying	0.3802
3-D	CD-DI_{3D}			0.1786
	CD-HD			0.1425
	Combined	β_2	ξ_i	μ_κ
		0	Fixed	0.3189
		0	Varying	0.3367
		1	Fixed	0.4323
		1	Varying	0.4154

5.4 Discussion and Conclusions

5.4.1 Discussion

A significant improvement of the κ coefficient was demonstrated when applying the combined method in comparison to methods exploiting 2-D or 3-D information separately. On one hand, 2-D change detection can take advantage of single-look processing, utilizing images with better spatial resolution and SNR, or multisquint processing to reduce errors caused by artifacts. Single-look processing mode is more challenging in tomographic SAR due to: 1) a reduced set of baselines, and 2) limitations of the method used for pulse compression and super-resolution in the normal dimension. For comparison purposes, neither CD-MSQ nor the combined approach exploits here single-look processing, however, better performance can be expected if CD-MSQ, and by extension the combined approach, utilizes single-looks. On the other hand, 3-D change detection takes advantage of the three-dimensional structure information, a more accurate radar cross section, and is less sensitive to differences in illumination due to disambiguated layover and foreshortening.

The kappa coefficients listed in Table 5.3 to Table 5.5 showed that the combined approaches provided best results. The parameter β_2 tunes the influence of the height difference in the change detection procedure. In general, better results were obtained when $\beta_2 > 0$. However, this also implies that if CD-HD does not yield compelling results then slightly better performance could be obtained when $\beta_2 = 0$. The performance of the combined methods can be improved in comparison to that reported here by varying the value of β_1 or β_2 or using class-dependent shape parameters. However, automation of those configurations can be challenging without introducing *a priori* knowledge of changes or learning the optimal values from the data in use. The CRF model can be further extended with additional potentials accounting for 3-D features, such as linearity, planarity and scattering but also at the cost of assuming knowledge of the shape of the changes or underlying targets. The combined approaches exploit the infrastructure of the time domain back-projection processor. If the 3-D SAR images are focused with frequency domain methods, then some adaptations are required: 1) voxelization of the point cloud, and 2) replacement of BM4D for a method suitable for denoising point clouds.

From the kappa profiles in Fig. 5.6 (a), Fig. 5.8 (a) and Fig. 5.10 (a), CD-DI_{3D} performs similarly to CD-MSQ but better than CD-HD for changes caused by short targets. Comparison of the maps in Fig. 5.5 (b-c),Fig. 5.7 (b-c),Fig. 5.9 (b-c) indicates that 3-D reconstruction of short targets, like vehicles, might not offer significant improvements for change detection purposes with cubic meter resolution cells sizes.

For changes caused by tall targets, CD-DI_{3D} provided slightly better results than CD-MSQ but worse than those given by CD-HD. However, visual inspection of Fig. 5.7 (c) and (d) revealed that CD-HD can increase the false alarm rate of changes caused by tall targets due to a vertical mis-registration of the scatterers. The kappa profiles in Fig. 5.6 (b), Fig. 5.8 (b) and Fig. 5.10 (b) show that changes caused by tall targets were significantly better detected in the 3-D domain because: 1) the methods can take advantage of the 3-D structure of the targets, and 2) the backscatter estimate of the targets was more accurate as they are focused at their real 3-D position. CD-DI_{3D} and CD-HD were more sensitive to errors caused by image artifacts, as they did not exploit multisquint processing. A 3-D multisquint processor increases considerably the computational complexity in comparison to that in the 2-D spatial domain [120]. For this reason, CD-MSQ or the 3-D combined approaches are more robust against errors caused by artifacts in comparison to CD-DI_{3D}, as can be observed in patch 3 in Fig. 5.5 and patch 2 in Fig. 5.7. In contrast to CD-HD and the combined approaches, CD-DI_{3D} was also more sensitive to mis-registration errors because it does not exploit spatial contextual information.

The methods utilized in this work do not account for errors caused by significant differences in the illumination conditions of the image pair. This could explain the false alarms caused by

the shadows of the trees in Fig. 5.5 and the false alarms caused by the shadow cast by the new building in Fig. 5.9. Shadowed areas can be computed in 2-D with up-to-date DSMs. In 3-D, estimation of the shadowed areas requires analysis of the slant range lines. However, presence of sidelobes in the normal direction and errors in the 3-D reconstruction can cause information loss, increasing the misdetection rate when applying change detection. If the roof of a building is partially reconstructed due to inherently low backscatter (as those in Fig. 5.9), then some elements will cast inexistent shadow areas. This situation requires special consideration in order to not partially eliminate the building itself or nearby targets.

In addition to pulse compression in range and azimuth, 3-D SAR image processing performs pulse compression in normal dimension. This implies that 3-D change detection needs adaptations to mitigate associated errors, such as phase noise. Fig. 5.7 (e) shows some false alarms in the tower masts of the cranes. Inaccuracies in the navigation data or the DTM in use, imprecise geometric calibration and phase noise are potential factors causing mis-registration of the targets in the image pair. Increasing the number of looks at the cost of degrading resolution and SNR, or increasing the number of baselines can be possible solutions to further reduce phase noise.

The false alarms at the bottom of the change maps in Fig. 5.5 could also be caused by differences in extent of the shadow of the trees due to wind. In Fig. 5.9, the trees at the north western side of the new building, in green, were not appropriately focused in the corresponding test SAR image due to windy conditions. These trees did not introduce significant false alarms when utilizing only the backscatter difference; however, in the 3-D domain the difference in structure of the canopy of the focused and unfocused trees can increase false alarms as shown in patch 5 in Fig. 5.9 (d). This suggests that tomographic SAR data of forested areas acquired with unstable weather conditions that can cause defocusing of the imaged trees require careful consideration for change detection purposes. Moreover, visual inspection of the maps in Fig. 5.9 revealed that the methods did not detect the changes caused by the cars in patch 1. Using a dissimilarity function based on second order statistics can be more suitable [23]. The false alarms caused by the wall indicated by the dashed ellipse in Fig. 5.9 (b-d) are spread out in the slant range dimension in the change map derived with CD-MSQ due to layover and double-bounces; i.e. in the 2-D spatial domain the wall is not focused at its real 3-D position.

The kappa coefficients in Table 5.6 show that the performance of the methods improved significantly when the change detectors take advantage of more detailed scene information; i.e. the kappa coefficient improves when using the 3-D images in comparison to that of the 2½-D images. The normal lines of the 2½-D images have maximally one scatterer, and thus contain less information. The limited capability to disambiguate layover causes: 1) an increase of misdetections in normal lines with presence of changes caused by laid-over targets; i.e. detection of the change involves multiple scatterers in the normal direction, and 2) an increase of false alarms in normal lines with unchanged laid-over targets; i.e. the retained strongest scatterer of a normal line of the reference and test images differs due to differences in the noise level, SNR, or coherence, but not due to a change. These factors highlight the benefits of SAR tomography for change detection of man-made targets in urban areas. A larger difference between the kappa coefficients obtained with the 2½-D and 3-D images can be expected in scenarios in the presence of multiple laid-over targets, such as forested areas.

The proposed method might require modifications when applied to 3-D SAR images with very different resolution cell sizes than those in this work. The interval of values of the scale parameter should account for sparser or denser 3-D images bearing in mind the size in voxels of the possible changes of interest. This interval might also vary significantly for image pairs acquired in high-density urban areas. Similarly, the minimum height for tall targets may vary depending on the resolution of the images and the size of the assumed shortest targets causing changes of interest. If 1) the 3-D SAR images can be focused using single-look processing mode, 2) the 2-D processing chain does not offer advantages in the change detection procedure,

and 3) costs and computational considerations can be neglected, then the combined change detection method can be simplified by performing only the second stage of the approach; i.e. the minimum height for tall targets is the ground. However, in that case the performance of the method greatly depended on the parameterization of the neighborhood of the CRF model. The subtraction of the log-transformed SAR images, utilized here as a dissimilarity function in CD-MSQ and the CRF model of the combined approach, can be replaced to better emphasize changes caused by natural distributed targets. Finally, the third stage of the combined approach can be simplified by performing only fusion of the two 3-D change maps assuming an absence of errors caused by the tomographic processing chain

5.4.2 Conclusions

A 2-D and 3-D combined change detector taking advantage of a back-projection tomographic framework was shown to outperform pure 2-D or 3-D methods. Quality assessment indicated that the kappa coefficient improved by a factor two in comparison to other established approaches. The kappa profile showed that the proposed method performed well when detecting changes caused by short and tall targets. Combination of backscatter and height difference information by means of a conditional random field resulted into further performance improvements. Quality assessment of the varying parameterization neighborhood scheme was shown to yield best results while being less sensitive to initial parameters. This work provides first references demonstrating the performance of tomographic SAR data acquired in medium density urban areas for change detection purposes.

Adaptations of the method to incorporate shape information by means of 3-D wavelets and curvelets or other techniques providing shape information could be considered in future work. Progress towards an object-oriented approach exploiting multifrequency or polarimetric SAR data is foreseen.

Acknowledgments

The authors would like to thank O. Frey and M. Volpi for fruitful discussions and the reviewers for their helpful contributions in improving this paper. We acknowledge the Fraunhofer FHR team and the pilots and all institutions involved in the MEMPHIS data collection during the Swiss and German campaigns in 2009 and 2012.

6 SYNOPSIS

6.1 Main results

The main findings of the research carried out in this work are reported in the following. The results are structured according to the research questions formulated in section 1.5, and based on the publications (in chapters 2 to 5) forming this thesis.

6.1.1 For SAR image focusing, how does adaptive pulse compression perform when applied to the signals recorded in slant range in comparison to different deterministic approaches, such as the matched filter?

In contrast to deterministic pulse compression methods such as the matched or mismatched filters, adaptive processing was shown to preserve spatial resolution and reduce sidelobes while producing a maximum SNR loss of 0.17 dB. Based on analysis of the signature of corner reflectors, the spatial resolution improved in average by a factor 1.06 in comparison to that obtained when using a matched filter. The highest sidelobe energy reduction was achieved in the second iteration, independent of the adaptive processing variant and the initialization stage. The net energy difference per image pixel due to sidelobes was in average -0.77 dB and -0.25 dB for the two adaptive processing approaches respectively. This suggested that two iterations are sufficient to reduce some sidelobes inherited from the initialization stage to the noise level.

After applying range adaptive processing, the quality of the corresponding SAR images improved in comparison to that obtained after focusing with deterministic approaches. Analysis of local and global quality indicators showed that when applying adaptive processing in range, the characteristics of the azimuth signals, in terms of spatial resolution and sidelobes, were preserved. This demonstrated that adaptive processing can be utilized independently of the pulse compression method in azimuth, respecting the inherent range-azimuth coupling in SAR. Under mismatch conditions; i.e. when the recorded replicas and the signals of the received pulses do not perfectly match, adaptive processing caused an increase of some sidelobes and a higher SNR loss.

For interferometric SAR, range adaptive processing offered more reliable phase estimates than the matched filter for unmasked targets (masked by nearby sidelobes when applying deterministic pulse compression methods) with strong backscatter. Unmasked de-correlating targets, such as asphalt-covered roads or water bodies, experienced a coherence reduction, while in sidelobe-free areas adaptive processing showed similar coherence to that derived from the images focused with the matched filter. This demonstrates that adaptive pulse compression provides both better amplitude and phase estimates of the range profiles. Image areas that experienced a coherence increase associated to an increase of sidelobes caused by adaptive processing under mismatched conditions still requires further analysis.

For frequency agile systems, fast adaptive processing yielded modest improvements, offering a sidelobe reduction efficiency of -0.57 dB and an average SNR loss of 0.18 dB. The method preserved the spatial resolution while involving a lower computational complexity. It respected the range-azimuth coupling of SAR, preserving the characteristics of the azimuth signals. Based on the quality assessment of the coherence images, the performance of fast adaptive processing regarding the reliability of the phase estimates was found to be moderate. However, it was observed that fast adaptive processing can introduce artifacts in the azimuth dimension when applied to a single sub-band of the range signals.

In global terms, by applying APC under single channel, interferometric and stepped frequency scenarios, the quality of the SAR images, the corresponding phase maps and interferometric coherence images improve. APC preserves the characteristics of the azimuth signals, and can be applied for SAR image focusing without restricting the azimuth compression scheme. Perfor-

mance improvements offered by adaptive processing when utilized for change detection purposes are described in section 6.1.3.

6.1.2 How can SAR change detection take advantage of different pulse compression methods in azimuth, such as single-look and multisquint processing mode?

In SAR-CD the presence of moving targets or image artifacts, such as sidelobes and azimuth ambiguities, increases the classification error, degrading the content of the change maps. The spatial response of some artifacts, such as sidelobes and ambiguities, varies during the aperture time due to their non-permanent scattering regime and anisotropy. Information on the spatial behavior of the targets was collected by means of a multisquint processing mode; by applying pulse compression with real-valued weightings to the signal recorded in the azimuth dimension. As the squinted sub-apertures have lower resolution and are not artifact-free, full-aperture images focused with single-look processing were also utilized to compute changes at nominal resolution with the highest SNR. Using multisquint processing, one can derive a new pair of images where artifacts do not appear in the same image pixels as those of their corresponding single-looks. This permits identification of associated false alarms and their removal from the change map computed with the single-looks. Based on this principle, a change detector combining the advantages of single-look and multisquint SAR processing modes was designed. The performance of the method confirmed that multisquint processing can be utilized to effectively reduce errors caused by image artifacts and moving targets, and when combined with single-looks, SAR-CD does not suffer from a significant decrease of the detection rate in comparison to that offered by single-look processing mode. Results with data sets acquired by F-SAR showed that the kappa coefficient improved on average by a factor 1.9 while preserving 95% of the detection rate compared to that obtained after applying the matched filter in range and azimuth and single-look processing, referred to here as traditional or standard processing. In this manner, SAR-CD applied to human activity monitoring or urban studies can take advantage of both processing methods, as sidelobes and moving targets are typically present in those scenarios. The performance improvements do not involve a significant increase in computation time in comparison to currently existing methods.

For SAR-CD purposes, combination of single-look and multisquint processing was also shown to increase robustness against errors caused by the migration to different image pixels of the shadowed areas, sidelobes, and scatterers of the buildings when the image pair was acquired with slightly different geometries. This property is particularly important when performing change detection with data acquired from drone-SAR or airborne SAR sensors, where inaccuracies in the navigation information and the effect of the wind and turbulence can cause significant flight track offsets. Combination of both processing modes was shown to be effective to reduce false alarms caused by unfocused targets, such as trees under windy conditions.

However, multisquint processing mode applied for SAR-CD purposes could reduce the detection rate for changes caused by buildings due to their inherent high anisotropy. This situation could be alleviated by performing 3-D reconstruction; however, at the cost of longer computation times.

In global terms, SAR-CD can take advantage of multisquint processing mode to mitigate errors caused by artifacts common in SAR imagery. In comparison to traditional change detection based on single-look images, better results are obtained by exploiting information on the spatial behavior of the targets provided by a set of squint images.

6.1.3 How does SAR change detection benefit from combinations of different range and azimuth pulse compression methods?

This research question builds upon the two previous ones. For SAR-CD purposes, matched filtering in range and azimuth combined with single-look processing mode leads to the highest detection rates, but also to the highest false alarm rates.

When applying adaptive processing in range and the matched filter in azimuth in combination with single-look processing mode, the kappa coefficient improved by a factor 1.22 while preserving 98% of the detection rate obtained of that offered by the SAR images focused with standard processing. Errors caused by the presence of image artifacts, mainly sidelobes, were moderately mitigated, while providing detection rates very similar to those obtained with standard processing. This moderate improvement can be explained by the performance of adaptive processing, in terms of sidelobe reduction efficiency, when the transmit waveform is an LFM signal together with the non-ideal matched scenario; i.e. the presence of mismatch between the transmitted and the received signals. If sidelobes mask areas with changes, then range adaptive processing combined with matched filter in azimuth and single-look processing mode is the most suitable configuration to detect and preserve the underlying change. Detection of changes caused by tall targets, such as buildings is also possible, as adaptive processing does not make assumptions on the scattering regime of the targets. This configuration involves a significant increase of the computation time; however, changes are detected at a slightly higher resolution offered by the adaptive processing method (see 6.1.1).

When applying the matched filter in range and azimuth combined with multisquint processing, the change detector provided the second best performance, reducing many errors caused by image artifacts and moving targets. The kappa coefficient improved by a factor 1.52 while preserving 97% of the detection rate in comparison to that offered by SAR images focused with standard processing. However, this configuration produced a decrease in the detection rate for changes caused by tall targets, as for those objects the assumption of the permanent scattering regime is unlikely to be true. If changes are caused by isotropic targets, then exploiting spatial information via multisquint processing is more effective to reduce errors caused by artifacts and moving targets than when range adaptive processing is exploited in isolation.

The configuration obtained when applying range adaptive processing, the matched filter in azimuth and multisquint processing mode lead to the best performance when changes were caused by isotropic targets. In this case, the kappa coefficient improved by a factor 1.86 while preserving 96% of the detection rate of that obtained when the SAR images were focused with standard processing methods. Like the previous case, this configuration can cause misdetections for changes caused by anisotropic targets, such as buildings. Similar to the second configuration, changes were detected at slightly higher resolution than when applying the matched filter in range and single-look in azimuth. However, range adaptive processing combined with multisquint processing in azimuth implies the worst-case time complexity.

Finally, change detection methods exploiting multisquint and adaptive processing provide better results than those using a conventional matched filter combined with single-look processing, although at the cost of a higher computation time or at the cost of potential misdetections of changes caused by anisotropic objects.

6.1.4 What are the implications of three dimensional SAR image focusing for change detection applications?

Pulse compression in the normal dimension is performed using adaptive processing methods due to the typically reduced set of available baselines in SAR tomography. Pulse compression is applied to the signals in the normal dimension after multi-look processing in range and azimuth so that the covariance matrices of the adaptive processing scheme are invertible. For this reason, 3-D SAR image reconstruction can hardly be performed using single-look processing. When the

change detector exploited both 2-D and 3-D SAR images, then the kappa coefficient improved by a factor 2.1 in comparison to that obtained with approaches using 2-D images only. SAR-CD was shown to take advantage of the 2-D SAR focusing chain by exploiting spatial information gathered via multisquint processing to reduce errors caused by artifacts without significantly increasing computation time. On the other hand, SAR-CD can take advantage of the 3-D volumetric structure of the targets, and a more accurate backscatter estimate as targets are focused at their real 3-D position. This suggests that SAR-CD based on 3-D imagery is less sensitive to errors caused by differences in illumination due to the disambiguation of layover and foreshortening. When the method exploited amplitude and height information, then the kappa coefficient improved by a factor 1.23 in comparison to that obtained when utilizing only amplitude data. This confirms that the performance of the approaches improves significantly when utilizing the volumetric structure information offered by SAR tomography when applied to change detection of man-made targets in urban areas.

In contrast to the two-dimensional case, SAR-CD based on 3-D images requires additional steps to mitigate errors caused by phase noise and minimize potential registration noise. Sidelobes in the normal dimension of the 3-D SAR images constrained the identification of shadowed areas. For change detection purposes the computation of shadows based on 3-D SAR images can cause a reduction of the detection rate. Furthermore, tomographic SAR processing of forested areas acquired in unstable weather conditions requires careful consideration for SAR-CD as differences in the structure of the canopy of the unfocused trees caused an increase in the number of false alarms.

Change detection methods combining 2-D and 3-D images outperform traditional 2-D only approaches, and perform well when detecting changes caused by short and tall targets. Combination of backscatter and height information results into further performance improvements, demonstrating the usefulness of SAR tomography for change detection purposes.

6.2 Conclusions

The potential of SAR to perform change detection applied to human activity monitoring and urban studies has been demonstrated by means of multiple airborne SAR experiments conducted with two high-resolution frequency agile sensors within this work.

The achievements in this thesis include contributions to SAR image formation techniques, image quality assessment, and change detection methods. Diverse pulse compression approaches, applied to the signals recorded in range, azimuth and normal dimensions of a typical stripmap configuration, have been studied and evaluated for change detection applications. For this purpose, two change detection schemes were designed to take advantage of additional information derived by exploiting different pulse compression methods and the corresponding focused SAR images. It has been shown that when the processing chain collaborated in the change detection procedure, SAR-CD improved overall performance in terms of detection and recognition of changes and became less sensitive to errors caused by information loss. SAR-CD exploiting standard pulse compression schemes, like the matched filter in range and azimuth combined with single-look processing mode, delivered the best detection but also highest false alarm rates in comparison to results obtained with other pulse compression methods. When applying adaptive processing to the signals in the range dimension, the kappa coefficient improved by a factor of 1.22, increasing to 1.86 when combined with multisquint processing. Change detection methods utilizing combined 2-D and 3-D information improved the kappa coefficient by at least a factor 1.78 in comparison to those obtained with approaches using 2-D or 3-D images only.

Based on the first research question, range adaptive processing can provide 3-D SAR images with lower sidelobes in range and a slightly better spatial resolution in comparison to those focused with the matched filter. Jointly, if a 3-D multisquint processing mode is utilized, then

SAR-CD is expected to better preserve changes caused by buildings and be more robust against false alarms caused by the canopies of the trees when illuminated under different windy conditions. The main reason is that the scatterers of tall static targets will be focused at their real 3-D position, limiting their migration to different image voxels and removal of the potential induced changes. The opposite effect is expected to occur for moving targets, where the scatterers of the canopies of the trees focused under windy conditions are expected to appear in different voxels in the different 3-D squint images. In global terms, a change detector exploiting a combination of adaptive processing, multisquint processing and tomographic reconstruction will potentially be more robust against the presence of image artifacts and moving targets, easing recognition of the changes and providing very similar detection rates to those obtained when applying traditional pulse compression methods and processing schemes. However, due to the increased computational complexity involved, combination of adaptive processing, multisquint processing mode and pulse compression in normal dimension was not analyzed here for SAR-CD purposes.

The methods in this thesis require adaptations when applied to agricultural studies or change detection in forest areas. The utilized dissimilarity function based on the log-ratio is not suitable to properly capture changes caused by natural distributed targets, as the associated changes typically assume relatively small backscatter changes. Dissimilarity functions based on the entropy or second-order statistics can instead be considered to increase the detection rate and reliability of the resulting change maps. The methods require modifications to account for multichannel data in the form of polarimetric and/or multifrequency data sets, and require additional processing and post-processing steps to accommodate SAR imagery acquired with non-linear trajectories.

6.3 Outlook

6.3.1 Polarimetric SAR in change detection

The change detection methods described in this work provide a good basis for detection of man-made targets in urban areas with single polarization data at a given carrier frequency. However, they require adaptations to accommodate additional information in the form of polarimetric and/or multifrequency data sets. Polarimetric SAR (PolSAR) provides information on the scattering mechanisms observed during the SAR data acquisition. When combined with interferometric (PolInSAR) or tomographic (PolTomoSAR) configurations, height, or volume structure and backscatter information can also be derived. Polarimetric information permits characterization of a target by analyzing the properties of the reradiated electromagnetic waves, assumed to be different than those of the incident pulse due to the interaction with the target itself. For example, bare soils can be identified with the power of the odd-bounce scattering, represented by the blue channel, at both S- and X-band in Fig. 6.1. Similarly, trees can be characterized with the power of the cross-polarization, represented by the green channel, in both frequency bands. This information can be exploited to preserve changes caused only by certain objects of interest while discarding the rest. Preliminary work following this research line has been reported in [48].

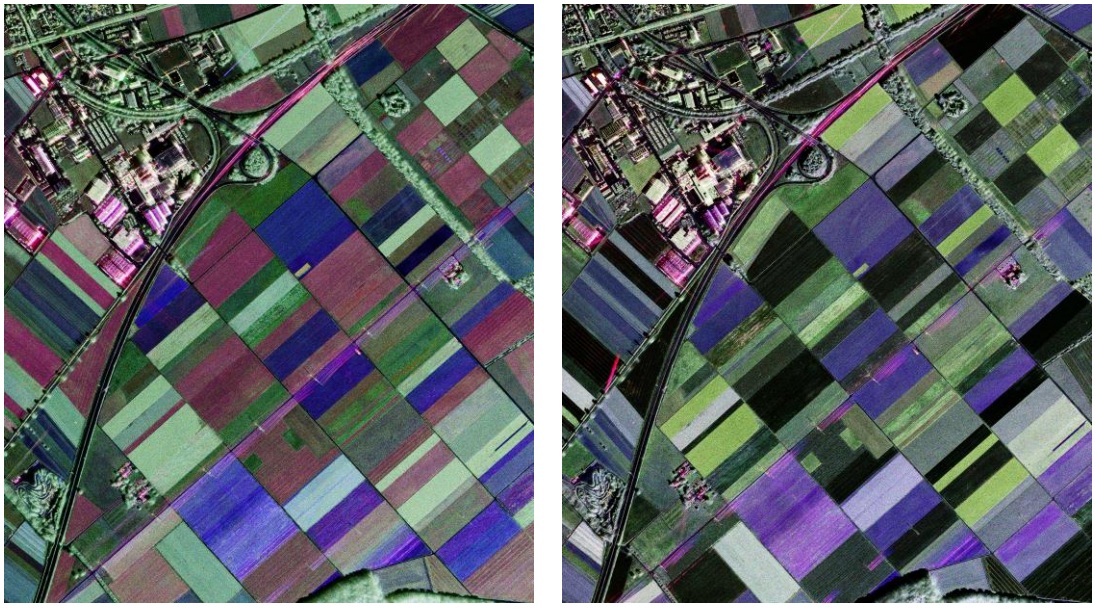

(a) Pauli RGB composite at S-band (b) Pauli RGB composite at X-band

Fig. 6.1 Pauli decomposition with the F-SAR data acquired in Oensingen (Switzerland) in 2010. Red channel representing the power of the even-bounce, blue channel odd-bounce, and green volume scattering.

PolSAR data can take advantage of more sophisticated multidimensional dissimilarity functions, enhancing changes caused by targets of interest. Leading to a more object-based change detection approach, single- or multifrequency PolSAR data could also be utilized at the classification level of the change detection procedure. Building a database of different targets with the corresponding radar backscatter as a function of polarization and wavelength enables simulations of potential changes; i.e. the approach could be configured to detect specific changes based on simulations of the change itself. Development of those methods could yield very accurate results and provide first references in this domain.

Investigations on polarimetric decomposition and classification methods of different targets can be performed to further improve SAR-CD. In urban areas, the presence of a single dominant scattering mechanism, and low entropy values can be expected. In contrast, natural environments are expected to be characterized by mixtures of mechanisms, related to high entropy values. Fig. 6.2 shows the polarimetric characteristics of an urban area and a forest, where the differences of their respective H-α diagrams can be observed. The polarimetric classification of the forest shows that two different tree types, labelled in purple and light blue, were identified. In urban areas, the polarimetric analysis of man-made complex targets, such as commercial and industrial buildings enables retracing the reflections of the backscattered waves at different elements of the buildings and from the interactions between the buildings and the surrounding area. With high-resolution data, it is possible to retrieve very detailed information, such as for example the status of the windows of the skylights or the building material. In some cases it is also possible to distinguish between different asphalt-covered roads.

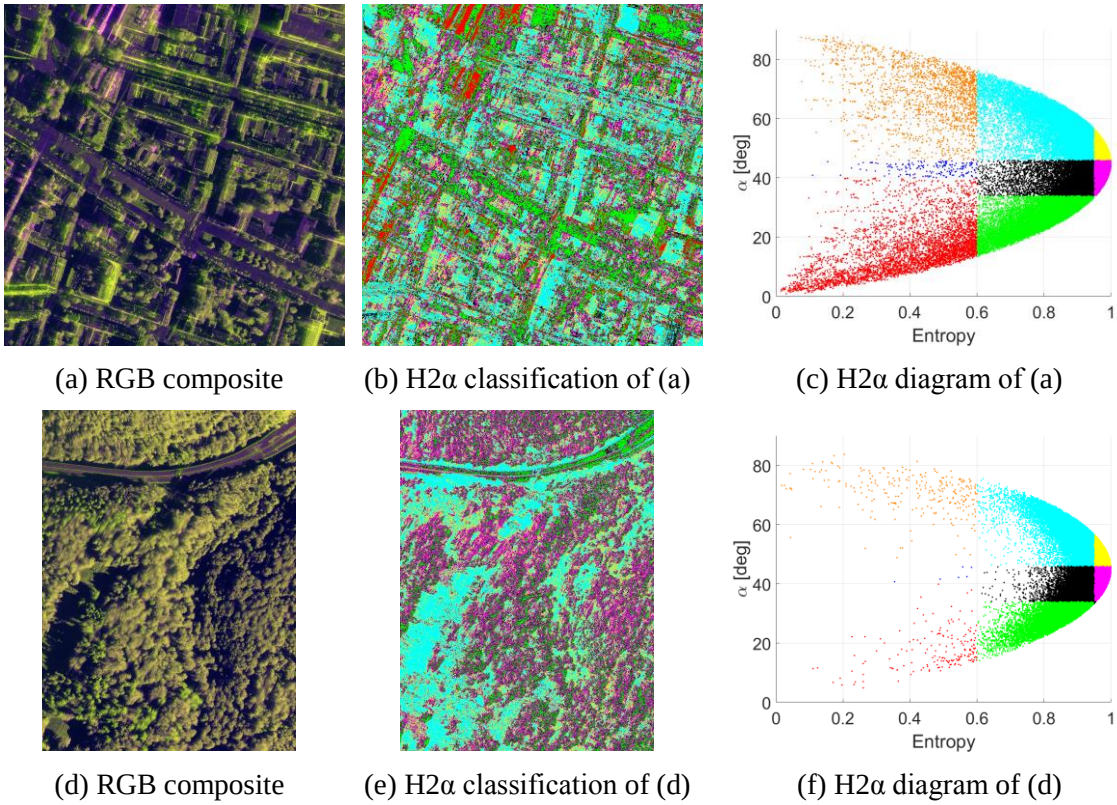

(a) RGB composite (b) H2α classification of (a) (c) H2α diagram of (a)

(d) RGB composite (e) H2α classification of (d) (f) H2α diagram of (d)

Fig. 6.2 Polarimetric analysis of an urban area and a forest with images acquired by the linear DualPol (VV, VH) system MIRANDA-35 at Ka-band. (a) and (d): 2-D polarimetric RGB composite, R=VV, G=VH, B=VV/VH. (b) and (e): polarimetric classification based on the eigen-decomposition H2α. (c) and (f): corresponding scatter plot of the H2α diagrams.

The increased availability of SAR sensors delivering 3-D information increases the scope of change detection applications and accuracy of the methods, particularly for urban studies and forest monitoring, where information on the volumetric structure of objects is more relevant. PolInSAR or PolTomoSAR data can be utilized to further distinguish different backscattering sources and increase the reliability of the tomographic reconstruction. The multisquint framework could be re-adapted to yield squints at higher resolution, while still being able to induce a rotation and displacement of some image artifacts to ease their later identification and removal. Such a framework will enable identification of additional artifacts, such as those related to cross-talk between channels. In addition, errors caused by sidelobes and ambiguities can be better identified and removed because the images of the cross-polarized channels have fewer artifacts of that type. Fig. 6.3 shows a 2-D, 2½-D and height map of some buildings. The 2-D image shows presence of abundant artifacts spread on top of the roofs, mainly localized in the green channel. Depending on the wavelength, PolInSAR or PolTomoSAR applied to change detection in urban scenarios can be exploited to improve the detection rate of changes caused by static man-made targets, characterized with one dominant scattering mechanism, typically odd- or even-bounce, while reducing errors induced by some natural distributed targets, such as trees, often characterized by volume scattering.

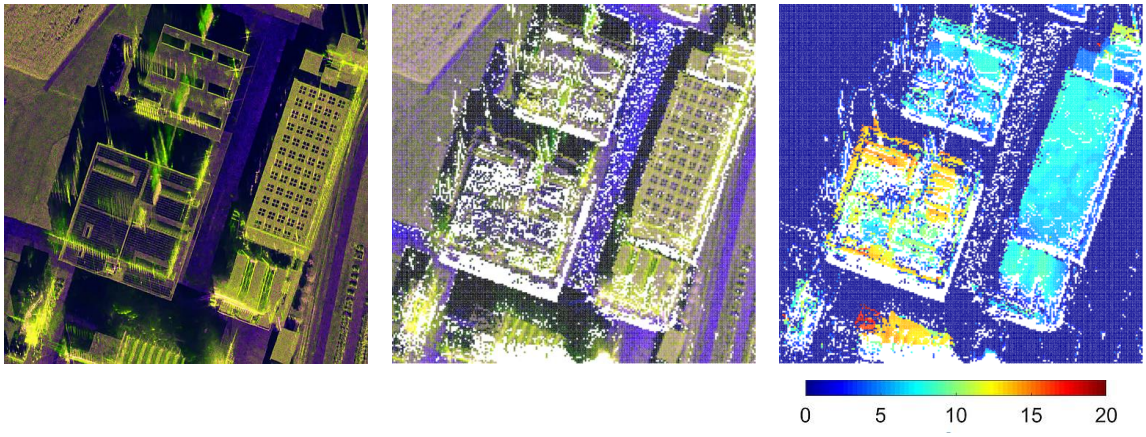

(a) 2-D RGB composite (b) 2½-D RGB composite (c) Height map in meters

Fig. 6.3 Interferometric reconstruction of MIRANDA-35 at Ka-band. (a): 2-D polarimetric RGB composite, R=VV, G=VH, B=VV/VH. (b): top view of the 2½-D polarimetric RGB composite. (c): top view of the 2½-D height map in meters above ground.

6.3.2 The role of the processing chain in SAR-CD

This work has shown that in the urban scenario, 3-D reconstruction can improve the detection of changes caused by tall targets. However, the image focusing method applied here assumes that the SAR images are acquired with a stripmap configuration and that the squint angle is smaller than half of the antenna beamwidth in azimuth. Jointly, the tomographic processor is only valid when the normal dimension is perpendicular to azimuth and slant range dimensions. This does not hold for non-linear flight paths, implying that the tomographic reconstruction of data sets acquired with drone-SAR or light airborne SAR systems requires adaptations to accommodate these new imaging conditions. Fig. 6.4 shows the 3-D reconstruction of SAR data acquired with a non-linear trajectory. One can observe the presence of wrinkles in the ground that can result when the normal dimension is not extracted properly.

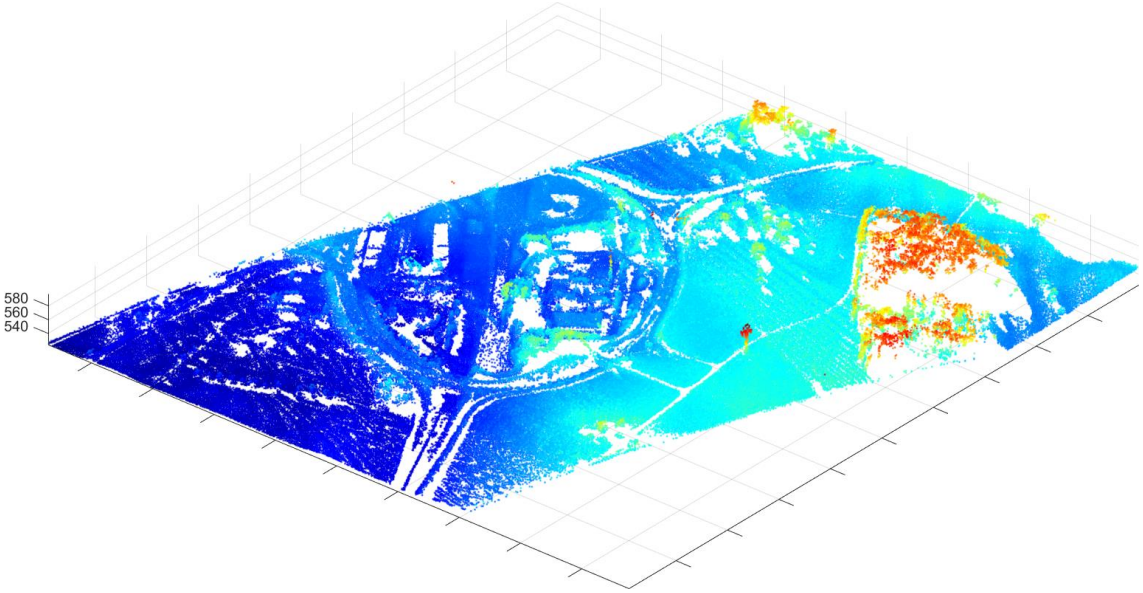

Fig. 6.4 Tomographic reconstruction of MEMPHIS data at Ka-band acquired with a non-linear flight path.

The change detection methods can be further developed by exploiting adaptive processing schemes to reduce false alarms caused by artifacts, or by improving the recognition of changes when considering super-resolution. Here, adaptive processing applied to SAR image focusing has been shown to provide state of the art high quality imagery. However, these techniques have not been analyzed when applied to the signals recorded in the azimuth dimension, or by extension, when applied simultaneously to the signals in range and azimuth. The performance improvements offered by adaptive processing could be compared with that of multisquint processing mode for change detection purposes. Further evaluation of the performance of fast adaptive processing methods and corresponding adaptations to dechirp signals recorded by FMCW SAR sensors should be considered.

Finally, this thesis dealt mainly with SAR data acquired over relatively flat areas. In the future, the application of radiometric terrain correction methods would make it possible to perform change detection in areas with steep topography and using acquisitions from diverging geometries. This would improve the performance of the change detection methods over forested areas in alpine terrain, as well as for monitoring glacier evolution.

LIST OF ABBREVIATIONS

APC	Adaptive Pulse Compression
APES	Amplitude and Phase Estimation
BM3D	Block Matching 3D
BM4D	Block Matching 4D
BP	Basis Pursuit
CD	Change Detection
CRF	Conditional Random Field
DEM	Digital Elevation Model
DI	Difference Image
DLR	*Deutsches Zentrum für Luft- und Raumfahrt e.V.* (German Aerospace Center)
EM	Expectation Maximization
FAPC	Fast Adaptive Pulse Compression
FCM	Final Change Map
FMCW	Frequency Modulated Continuous Wave
Fraunhofer/FHR	Fraunhofer Institute for High Frequency Physics and Radar Techniques
GPU	Graphics Processing Unit
HDVI	High Definition Vector Imaging
ICI	Interferometric Coherence Image
ICM	Initial Change Map
InSAR	SAR Interferometry
IS	Initialization Stage
ISLR	Integrated SideLobe Ratio
KLD	Kullback-Leibler Distance
LFM	Linear Frequency Modulation
LiDAR	Light Detection and Ranging
LRI	Log-Ratio Image
LSMMF	Least Squares Mismatched Filter
MCA	Morphological Components Analysis
MCA-MOM	Morphological Components Analysis Mean of Maximum
MEMPHIS	Millimeterwave Experimental Multifrequency Polarimetric High-resolution Interferometric System
MF	Matched Filter
MFK	Matched Filter with Kaiser window
ML	Maximum Likelihood
MMF	Mismatched Filter
MMSE	Minimum Mean Square Error
MRF	Markov Random Field
MSF	Multisquint Framework
MVM	Minimum Variance Method
PCA	Principal Components Analysis
PolInSAR	Polarimetric Interferometric SAR
PolSAR	Polarimetric SAR

PolTomoSAR	Polarimetric Tomographic SAR
PSF	Point Spread Function
PSI	Persistent Scatterer Inteferometry
PSLR	Peak Sidelobe Ratio
RFI	Radio Frequency Interference
SAR	Synthetic Aperture Radar
SAR-CD	SAR Change Detection
SNR	Signal-to-Noise Ratio
SVA	Spatially Variant Apodization
TDBP	Time Domain Back-Projection
TDC	Time Domain Correlation
TomoSAR	SAR Tomography

REFERENCES

[1] J. B. Campbell and R. H. Wynne, *Introduction to remote sensing*. Guilford Press, 2011.

[2] E. J. Rignot and J. J. Van Zyl, "Change detection techniques for ERS-1 SAR data," *IEEE Transactions on Geoscience and Remote Sensing*, vol. 31, no. 4, pp. 896-906, 1993.

[3] L. Bruzzone and D. F. Prieto, "Automatic analysis of the difference image for unsupervised change detection," *IEEE Transactions on Geoscience and Remote sensing*, vol. 38, no. 3, pp. 1171-1182, 2000.

[4] D. Brunner, G. Lemoine, and L. Bruzzone, "Earthquake damage assessment of buildings using VHR optical and SAR imagery," *IEEE Transactions on Geoscience and Remote Sensing*, vol. 48, no. 5, pp. 2403-2420, 2010.

[5] L. Bruzzone and F. Bovolo, "A novel framework for the design of change-detection systems for very-high-resolution remote sensing images," *Proceedings of the IEEE*, vol. 101, no. 3, pp. 609-630, 2013.

[6] F. Bovolo and L. Bruzzone, "A split-based approach to unsupervised change detection in large-size multitemporal images: Application to tsunami-damage assessment," *IEEE Transactions on Geoscience and Remote Sensing*, vol. 45, no. 6, pp. 1658-1670, 2007.

[7] M. Gong, T. Zhan, P. Zhang, and Q. Miao, "Superpixel-based difference representation learning for change detection in multispectral remote sensing images," *IEEE Transactions on Geoscience and Remote Sensing*, vol. 55, no. 5, pp. 2658-2673, 2017.

[8] T. Yamamoto, H. Hanaizumi, and S. Chino, "A change detection method for remotely sensed multispectral and multitemporal images using 3-D segmentation," *IEEE Transactions on Geoscience and Remote Sensing*, vol. 39, no. 5, pp. 976-985, 2001.

[9] L. Bruzzone and S. B. Serpico, "An iterative technique for the detection of land-cover transitions in multitemporal remote-sensing images," *IEEE transactions on geoscience and remote sensing*, vol. 35, no. 4, pp. 858-867, 1997.

[10] S. Liu, M. Chi, Y. Zou, A. Samat, J. A. Benediktsson, and A. Plaza, "Oil spill detection via multitemporal optical remote sensing images: A change detection perspective," *IEEE Geoscience and Remote Sensing Letters*, vol. 14, no. 3, pp. 324-328, 2017.

[11] S. H. Khan, X. He, F. Porikli, and M. Bennamoun, "Forest change detection in incomplete satellite images with deep neural networks," *IEEE Transactions on Geoscience and Remote Sensing*, vol. 55, no. 9, pp. 5407-5423, 2017.

[12] Y. Zeng, M. E. Schaepman, B. Wu, J. G. Clevers, and A. K. Bregt, "Scaling-based forest structural change detection using an inverted geometric-optical model in the Three Gorges region of China," *Remote Sensing of Environment*, vol. 112, no. 12, pp. 4261-4271, 2008.

[13] F. Bovolo and L. Bruzzone, "A detail-preserving scale-driven approach to change detection in multitemporal SAR images," *IEEE Transactions on Geoscience and Remote Sensing,* vol. 43, no. 12, pp. 2963-2972, 2005.

[14] K. I. Ranney and M. Soumekh, "Signal subspace change detection in averaged multilook SAR imagery," *IEEE Transactions on Geoscience and Remote Sensing,* vol. 44, no. 1, pp. 201-213, 2006.

[15] M. Soumekh, "Signal subspace fusion of uncalibrated sensors with application in SAR and diagnostic medicine," *IEEE Transactions on Image Processing,* vol. 8, no. 1, pp. 127-137, 1999.

[16] K. Ranney and M. Soumekh, "Adaptive change detection in coherent and noncoherent SAR imagery," in *Radar Conference, 2005 IEEE International*, 2005, pp. 195-200.

[17] Y. Ban and O. A. Yousif, "Multitemporal spaceborne SAR data for urban change detection in China," *IEEE Journal of Selected Topics in Applied Earth Observations and Remote Sensing,* vol. 5, no. 4, pp. 1087-1094, 2012.

[18] C. Marin, F. Bovolo, and L. Bruzzone, "Building change detection in multitemporal very high resolution SAR images," *IEEE Transactions on Geoscience and Remote Sensing,* vol. 53, no. 5, pp. 2664-2682, 2015.

[19] P. Gamba, F. Dell'Acqua, and G. Lisini, "Change detection of multitemporal SAR data in urban areas combining feature-based and pixel-based techniques," *IEEE Transactions on Geoscience and Remote Sensing,* vol. 44, no. 10, pp. 2820-2827, 2006.

[20] S. M. Scarborough *et al.*, "A challenge problem for SAR change detection and data compression," in *SPIE Defense, Security, and Sensing*, 2010, vol. 7699, pp. 76990U-76990U-5: International Society for Optics and Photonics.

[21] F. Bovolo, C. Marin, and L. Bruzzone, "A hierarchical approach to change detection in very high resolution SAR images for surveillance applications," *IEEE Transactions on Geoscience and Remote Sensing,* vol. 51, no. 4, pp. 2042-2054, 2013.

[22] M. Rüetschi, M. E. Schaepman, and D. Small, "Using Multitemporal Sentinel-1 C-band Backscatter to Monitor Phenology and Classify Deciduous and Coniferous Forests in Northern Switzerland," *Remote Sensing,* vol. 10, no. 1, p. 55, 2017.

[23] S. Cui, G. Schwarz, and M. Datcu, "A Benchmark Evaluation of Similarity Measures for Multitemporal SAR Image Change Detection," *IEEE Journal of Selected Topics in Applied Earth Observations and Remote Sensing,* vol. 9, pp. 1101-1118, March 2016.

[24] T. Celik and K.-K. Ma, "Unsupervised change detection for satellite images using dual-tree complex wavelet transform," *IEEE Transactions on Geoscience and Remote Sensing,* vol. 48, no. 3, pp. 1199-1210, 2010.

[25] O. Yousif and Y. Ban, "Improving urban change detection from multitemporal SAR images using PCA-NLM," *IEEE Transactions on Geoscience and Remote Sensing,* vol. 51, no. 4, pp. 2032-2041, 2013.

[26] J.-L. Starck, F. Murtagh, and J. M. Fadili, *Sparse image and signal processing: wavelets, curvelets, morphological diversity*. Cambridge university press, 2010.

[27] M. Preiss and N. J. Stacy, "Coherent change detection: Theoretical description and experimental results," Defence Science and Technology Organisation Edinburgh, 2006.

[28] A. Reigber *et al.*, "Very-high-resolution airborne synthetic aperture radar imaging: Signal processing and applications," *Proceedings of the IEEE*, vol. 101, no. 3, pp. 759-783, 2013.

[29] D. Blacknell and H. Griffiths, *Radar automatic target recognition (ATR) and non-cooperative target recognition (NCTR)*. The Institution of Engineering and Technology, 2013.

[30] D. D. Madsen, "Multi-Aperture Coherent Change Detection and Interferometry for Synthetic Aperture Radar," Brigham Young University, 2010.

[31] A. Damini, V. Mantle, and G. Davidson, "A new approach to coherent change detection in VideoSAR imagery using stack averaged coherence," in *IEEE Radar Conference (RADAR)*, 2013, pp. 1-5.

[32] L. M. Novak, "Change detection for multi-polarization multi-pass SAR," in *Proc. of SPIE*, vol. 5808, p. 235, 2005.

[33] L. M. Novak, "Coherent change detection for multi-polarization SAR," in *Signals, Systems and Computers, 2005. Conference Record of the Thirty-Ninth Asilomar Conference on*, pp. 568-573, 2005.

[34] A. Garzelli and C. Zoppetti, "Optimizing SAR change detection based on log-ratio features," in *9th International Workshop on the Analysis of Multitemporal Remote Sensing Images (MultiTemp)*, pp. 1-4, 2017.

[35] K. Dabov, A. Foi, V. Katkovnik, and K. Egiazarian, "Image denoising by sparse 3-D transform-domain collaborative filtering," *IEEE Transactions on Image Processing*, vol. 16, no. 8, pp. 2080-2095, 2007.

[36] A. Schmitt, B. Wessel, and A. Roth, "Curvelet approach for SAR image denoising, structure enhancement, and change detection," 2009.

[37] M. Maggioni, V. Katkovnik, K. Egiazarian, and A. Foi, "Nonlocal transform-domain filter for volumetric data denoising and reconstruction," *IEEE Transactions on Image Processing*, vol. 22, no. 1, pp. 119-133, 2013.

[38] M. K. Ridd and J. Liu, "A comparison of four algorithms for change detection in an urban environment," *Remote sensing of environment*, vol. 63, no. 2, pp. 95-100, 1998.

[39] J. Inglada and G. Mercier, "A new statistical similarity measure for change detection in multitemporal SAR images and its extension to multiscale change analysis," *IEEE transactions on geoscience and remote sensing*, vol. 45, no. 5, pp. 1432-1445, 2007.

[40] F. Bovolo, C. Marin, and L. Bruzzone, "A novel hierarchical approach to change detection with very high resolution SAR images for surveillance applications," in *Geoscience and Remote Sensing Symposium (IGARSS), 2012 IEEE International*, 2012, pp. 1992-1995.

[41] F. Bovolo and L. Bruzzone, "An adaptive technique based on similarity measures for change detection in very high resolution SAR images," in *Geoscience and Remote Sensing Symposium, 2008. IGARSS 2008. IEEE International*, 2008, vol. 3, pp. 158-161.

[42] N. Bouhlel, G. Ginolhac, E. Jolibois, and A. Atto, "Multivariate Statistical Modeling for Multi-Temporal SAR Change Detection using Wavelet Transforms," in *8th International Workshop on the Analysis of Multitemporal Remote Sensing Images (Multi-Temp)*, pp. 1-4, 2015.

[43] S.-K. Choy and C.-S. Tong, "Statistical Wavelet Subband Characterization Based on Generalized Gamma Density and Its Application in Texture Retrieval," *IEEE Transactions on Image Processing*, vol. 19, no. 2, pp. 281-289, 2010.

[44] S. Cui and M. Datcu, "Statistical Wavelet Subband Modeling for Multi-Temporal SAR Change Detection," *IEEE Journal of Selected Topics in Applied Earth Observations and Remote Sensing*, vol. 5, no. 4, pp. 1095-1109, 2012.

[45] J. Ma, M. Gong, and Z. Zhou, "Wavelet fusion on ratio images for change detection in SAR images," *IEEE Geoscience and Remote Sensing Letters*, vol. 9, no. 6, pp. 1122-1126, 2012.

[46] B. Hou, Q. Wei, Y. Zheng, and S. Wang, "Unsupervised change detection in SAR image based on Gauss-log ratio image fusion and compressed projection," *IEEE journal of selected topics in applied earth observations and remote sensing*, vol. 7, no. 8, pp. 3297-3317, 2014.

[47] A. Schmitt, A. Wendleder, B. Wessel, and A. Roth, "Comparison of alternative image representations in the context of SAR change detection," in *Geoscience and Remote Sensing Symposium (IGARSS), 2010 IEEE International*, 2010, pp. 284-287.

[48] E. M. Dominguez, D. Henke, D. Small, and E. Meier, "Fully polarimetric high-resolution airborne SAR image change detection with morphological component analysis," in *Image and Signal Processing for Remote Sensing XXI*, 2015, vol. 9643, p. 964312: International Society for Optics and Photonics.

[49] A. Schmitt and B. Wessel, "Introducing partial polarimetric layers into a curvelet-based change detection," in *8th European Conference on Synthetic Aperture Radar (EUSAR)*, 2010, pp. 1-4.

[50] A. A. Nielsen, K. Conradsen, and H. Skriver, "Change detection in full and dual polarization, single-and multifrequency SAR data," *IEEE Journal of Selected Topics in Applied Earth Observations and Remote Sensing*, vol. 8, no. 8, pp. 4041-4048, 2015.

[51] D. Ciuonzo, V. Carotenuto, and A. De Maio, "On Multiple Covariance Equality Testing with Application to SAR Change Detection," *IEEE Transactions on Signal Processing*, vol. 65, no. 19, pp. 5078-5091, 2017.

[52] A. Marino, S. R. Cloude, and J. M. Lopez-Sanchez, "A new polarimetric change detector in radar imagery," *IEEE Transactions on Geoscience and Remote Sensing*, vol. 51, no. 5, pp. 2986-3000, 2013.

[53] K. Conradsen, A. A. Nielsen, J. Schou, and H. Skriver, "A test statistic in the complex Wishart distribution and its application to change detection in polarimetric SAR data," *IEEE Transactions on Geoscience and Remote Sensing*, vol. 41, no. 1, pp. 4-19, 2003.

[54] P. Kersten, J. Lee, and T. Ainsworth, "A comparison of change detection statistics in POLSAR images," NAVAL RESEARCH LAB WASHINGTON DC REMOTE SENSING DIV2005.

[55] M. Preiss and N. J. Stacy, "Polarimetric SAR coherent change detection," in *7th European Conference on Synthetic Aperture Radar (EUSAR)*, 2008, pp. 1-4.

[56] M. Molinier and Y. Rauste, "Comparison and evaluation of polarimetric change detection techniques in aerial SAR data," in *IEEE International Geoscience and Remote Sensing Symposium, (IGARSS)*, 2007, pp. 2386-2389.

[57] J. Inglada, V. Muron, D. Pichard, and T. Feuvrier, "Analysis of artifacts in subpixel remote sensing image registration," *IEEE Transactions on Geoscience and Remote Sensing*, vol. 45, no. 1, pp. 254-264, 2007.

[58] M. Guizar-Sicairos, S. T. Thurman, and J. R. Fienup, "Efficient subpixel image registration algorithms," *Optics letters*, vol. 33, no. 2, pp. 156-158, 2008.

[59] M. Vespe and H. Greidanus, "SAR image quality assessment and indicators for vessel and oil spill detection," *IEEE Transactions on Geoscience and Remote Sensing*, vol. 50, no. 11, pp. 4726-4734, 2012.

[60] V. T. Vu, T. K. Sjögren, M. I. Pettersson, and A. Gustavsson, "Definition on SAR image quality measurements for UWB SAR," in *SPIE*, 2008, vol. 7109, p. 71091A: International Society for Optics and Photonics.

[61] M. P. Zénere, "SAR Image Quality Assesment," ed: Universidad Nacional de Cordoba, Spain, 2012.

[62] M. I. Skolnik, *Radar handbook*. New York, NY, USA: McGraw-Hill, 1970.

[63] C. Oliver and S. Quegan, *Understanding synthetic aperture radar images*. Boston, MA: Artech House, 1998.

[64] N. Levanon and E. Mozeson, *Radar signals*. New York, NY, USA: John Wiley & Sons, 2004.

[65] M. Soumekh, *Synthetic aperture radar signal processing*. New York, NY, USA: Wiley, 1999.

[66] A. Reigber and A. Moreira, "First demonstration of airborne SAR tomography using multibaseline L-band data," *IEEE Transactions on Geoscience and Remote Sensing*, vol. 38, no. 5, pp. 2142-2152, 2000.

[67] F. J. Harris, "On the use of windows for harmonic analysis with the discrete Fourier transform," *Proceedings of the IEEE*, vol. 66, no. 1, pp. 51-83, 1978.

[68] J. Baden and M. Cohen, "Optimal peak sidelobe filters for biphase pulse compression," in *Record of the IEEE International Radar Conference*, 1990, pp. 249-252.

[69] K. R. Griep, J. Ritcey, and J. J. Burlingame, "Poly-phase codes and optimal filters for multiple user ranging," *IEEE Transactions on Aerospace and Electronic Systems*, vol. 31, no. 2, pp. 752-767, 1995.

[70] S. Mallat, *A wavelet tour of signal processing*. San Diego, CA: Academic, 1998.

[71] E. Candes, L. Demanet, D. Donoho, and L. Ying, "Fast discrete curvelet transforms," *Multiscale Modeling & Simulation*, vol. 5, no. 3, pp. 861-899, 2006.

[72] J. Ma and G. Plonka, "A review of curvelets and recent applications," *IEEE Signal Processing Magazine*, vol. 27, no. 2, pp. 118-133, 2010.

[73] M. N. Do and M. Vetterli, "The finite ridgelet transform for image representation," *IEEE Transactions on image Processing*, vol. 12, no. 1, pp. 16-28, 2003.

[74] J. Bobin, J.-L. Starck, J. M. Fadili, Y. Moudden, and D. L. Donoho, "Morphological component analysis: An adaptive thresholding strategy," *IEEE Transactions on Image Processing*, vol. 16, no. 11, pp. 2675-2681, 2007.

[75] T. Celik, "Unsupervised change detection in satellite images using principal component analysis and k-means clustering," *IEEE Geoscience and Remote Sensing Letters*, vol. 6, no. 4, pp. 772-776, 2009.

[76] J. Kittler and J. Illingworth, "Minimum error thresholding," *Pattern recognition*, vol. 19, no. 1, pp. 41-47, 1986.

[77] J. E. Cilliers and J. C. Smit, "Pulse compression sidelobe reduction by minimization of L p-norms," *IEEE Transactions on Aerospace and Electronic Systems*, vol. 43, no. 3, pp. 1238-1247, 2007.

[78] T. K. Sarkar and R. D. Brown, "An ultra-low sidelobe pulse compression technique for high performance radar systems," in *IEEE National Radar Conference*, 1997, pp. 111-114.

[79] H. C. Stankwitz, R. J. Dallaire, and J. R. Fienup, "Nonlinear apodization for sidelobe control in SAR imagery," *IEEE Transactions on Aerospace and Electronic Systems*, vol. 31, no. 1, pp. 267-279, 1995.

[80] H. Stankwitz and M. Kosek, "Super-resolution for SAR/ISAR RCS measurement using spatially variant apodization," in *17th Annual Meeting and Symposium of the Proceedings of the Antenna Measurement Techniques Association (AMTA)*, Williamsburg, VA, 13-17 November, 1995, pp. 251-256.

[81] C. F. Castillo-Rubio, S. Llorente-Romano, and M. Burgos-García, "Spatially variant apodization for squinted synthetic aperture radar images," *IEEE Transactions on Image Processing*, vol. 16, no. 8, pp. 2023-2027, 2007.

[82] L. M. Ulander, H. Hellsten, and G. Stenstrom, "Synthetic-aperture radar processing using fast factorized back-projection," *IEEE Transactions on Aerospace and Electronic Systems*, vol. 39, no. 3, pp. 760-776, 2003.

[83] B. Barber, "Theory of digital imaging from orbital synthetic-aperture radar," *International Journal of Remote Sensing*, vol. 6, no. 7, pp. 1009-1057, 1985.

[84] O. Frey, C. Magnard, M. Rüegg, and E. Meier, "Focusing of airborne synthetic aperture radar data from highly nonlinear flight tracks," *IEEE Transactions on Geoscience and Remote Sensing,* vol. 47, no. 6, pp. 1844-1858, June 2009.

[85] P. López-Dekker and J. J. Mallorquí, "Capon- and APES-based SAR processing: Performance and practical considerations," *IEEE Transactions on Geoscience and Remote Sensing,* vol. 48, no. 5, pp. 2388-2402, 2010.

[86] J. Capon, "High-resolution frequency-wavenumber spectrum analysis," *Proceedings of the IEEE,* vol. 57, no. 8, pp. 1408-1418, August 1969.

[87] P. Stoica, H. Li, and J. Li, "A new derivation of the APES filter," *IEEE Signal Processing Letters,* vol. 6, no. 8, pp. 205-206, 1999.

[88] G. R. Benitz, "High-definition vector imaging," *Lincoln Laboratory Journal,* vol. 10, no. 2, pp. 147-170, 1997.

[89] O. Frey and E. Meier, "Combining time-domain back-projection and Capon beamforming for tomographic SAR processing," in *IEEE International Geoscience and Remote Sensing Symposium (IGARSS)*, 2008, vol. 2, pp. 445-448.

[90] F. Lombardini and A. Reigber, "Adaptive spectral estimation for multibaseline SAR tomography with airborne L-band data," in *International Geoscience and Remote Sensing Symposium (IGARSS)*, 2003, vol. 3, pp. 2014-2016.

[91] S. D. Blunt and K. Gerlach, "Adaptive pulse compression via MMSE estimation," *IEEE Transactions on Aerospace and Electronic Systems,* vol. 42, no. 2, pp. 572-584, April 2006.

[92] S. D. Blunt, B. K. Gerlach, and T. Higgins, "Aspects of radar range super-resolution," in *IEEE Radar Conference*, 2007, pp. 683-687.

[93] S. D. Blunt, A. K. Shackelford, K. Gerlach, and K. J. Smith, "Doppler compensation & single pulse imaging using adaptive pulse compression," *IEEE Transactions on Aerospace and Electronic Systems,* vol. 45, no. 2, pp. 647-659, 2009.

[94] S. D. Blunt and T. Higgins, "Dimensionality reduction techniques for efficient adaptive pulse compression," *IEEE Transactions on Aerospace and Electronic Systems,* vol. 46, no. 1, pp. 349-362, 2010.

[95] H. Schimpf, H. Essen, S. Boehmsdorff, and T. Brehm, "MEMPHIS–a fully polarimetric experimental radar," in *IEEE International Geoscience and Remote Sensing Symposium (IGARSS)*, Toronto, Canada, 2002, vol. 3, pp. 1714-1716.

[96] M. Schmitt, "Three-dimensional reconstruction of urban areas by multi-aspect TomoSAR data fusion," in *Joint Urban Remote Sensing Event (JURSE)*, 2015, pp. 1-4.

[97] T. Higgins, S. D. Blunt, and K. Gerlach, "Gain-constrained adaptive pulse compression via an MVDR framework," in *IEEE Radar Conference*, 2009, pp. 1-6.

[98] T. Higgins, S. D. Blunt, and A. K. Shackelford, "Time-range adaptive processing for pulse agile radar," in *International Waveform Diversity and Design Conference (WDD)*, 2010, pp. 115-120.

[99] R. T. Lord, "Aspects of Stepped-Frequency Processing for Low-Frequency SAR Systems," Ph.D. dissertation, Department of Electrical Engineering, University of Cape Town, Rondebosch, South Africa, 2000.

[100] C. Magnard, M. Frioud, D. Small, T. Brehm, H. Essen, and E. Meier, "Processing of MEMPHIS Ka-Band Multibaseline Interferometric SAR Data: From Raw Data to Digital Surface Models," *IEEE Journal of Selected Topics in Applied Earth Observations and Remote Sensing*, vol. 7, no. 7, pp. 2927-2941, July 2014.

[101] A. Reigber, E. Alivizatos, A. Potsis, and A. Moreira, "Extended wavenumber-domain synthetic aperture radar focusing with integrated motion compensation," *IEE Proceedings-Radar, Sonar and Navigation*, vol. 153, no. 3, pp. 301-310, June 2006.

[102] C. Magnard, M. Frioud, D. Small, T. Brehm, and E. Meier, "Analysis of a maximum likelihood phase estimation method for airborne multibaseline SAR interferometry," *IEEE Journal of Selected Topics in Applied Earth Observations and Remote Sensing*, pp. 1072-1085, 2016.

[103] E. Rodriguez and J. Martin, "Theory and design of interferometric synthetic aperture radars," *IEE Proceedings F (Radar and Signal Processing)*, vol. 139, no. 2, pp. 147-159, April 1992.

[104] I. G. Cumming and F. H. Wong, *Digital processing of synthetic aperture radar data: algorithms and implementation*. Artech House, 2005.

[105] E. Liu, J. Wang, and T. Wang, "Phase imbalance compensation in SAR/ISAR quadrature demodulation," in *2nd Asian-Pacific Conference on Synthetic Aperture Radar (APSAR)*, 2009, pp. 459-463.

[106] B. Razavi, "Design considerations for direct-conversion receivers," *IEEE Transactions on Circuits and Systems II: Analog and Digital Signal Processing*, vol. 44, no. 6, pp. 428-435, 1997.

[107] A. W. Doerry, "Anatomy of a SAR Impulse Response," *Sandia report SAND2007-5042, Unlimited Release*, 2007.

[108] J.-S. Lee, M. R. Grunes, and G. De Grandi, "Polarimetric SAR speckle filtering and its implication for classification," *IEEE Transactions on Geoscience and remote sensing*, vol. 37, no. 5, pp. 2363-2373, 1999.

[109] J.-S. Lee, A. R. Miller, and K. W. Hoppel, "Statistics of phase difference and product magnitude of multi-look processed Gaussian signals," *Waves in random media*, vol. 4, no. 3, pp. 307-320, 1994.

[110] P. Prats and J. J. Mallorqui, "Estimation of azimuth phase undulations with multisquint processing in airborne interferometric SAR images," *IEEE Transactions on Geoscience and Remote Sensing*, vol. 41, no. 6, pp. 1530-1533, June 2003.

[111] M. Younis, C. Fischer, and W. Wiesbeck, "Digital beamforming in SAR systems," *IEEE Transactions on Geoscience and Remote Sensing*, vol. 41, no. 7, pp. 1735-1739, 2003.

[112] E. M. Dominguez, D. Henke, D. Small, and E. Meier, "High Resolution Airborne SAR Image Change Detection in Urban Areas with Slightly Different Acquisition

Geometries," *The International Archives of Photogrammetry, Remote Sensing and Spatial Information Sciences*, vol. 40, no. 3, p. 127, 2015.

[113] C. Prati and F. Rocca, "Focusing SAR data with time-varying Doppler centroid," *IEEE Transactions On Geoscience and Remote Sensing*, vol. 30, no. 3, pp. 550-559, 1992.

[114] M. Leigsnering, M. G. Amin, F. Ahmad, and A. M. Zoubir, "Multipath Exploitation and Suppression for SAR Imaging of Building Interiors: An overview of recent advances," *IEEE Signal Processing Magazine*, vol. 31, no. 4, pp. 110-119, 2014.

[115] D. Henke, E. Mendez Dominguez, D. Small, M. E. Schaepman, and E. Meier, "Moving target tracking in single- and multichannel SAR," *IEEE Transactions on Geoscience and Remote Sensing*, vol. 53, no. 6, pp. 3146-3159, 2015.

[116] M. Gong, L. Su, M. Jia, and W. Chen, "Fuzzy clustering with a modified MRF energy function for change detection in synthetic aperture radar images," *IEEE Transactions on Fuzzy Systems*, vol. 22, no. 1, pp. 98-109, 2014.

[117] K. He, J. Sun, and X. Tang, "Guided image filtering," *IEEE Transactions on Pattern Analysis and Machine Intelligence*, vol. 35, no. 6, pp. 1397-1409, 2013.

[118] F. Bovolo, C. Marin, and L. Bruzzone, "Freight traffic surveillance in VHR SAR images by multiscale information extraction," in *Tyrrhenian Workshop on Advances in Radar and Remote Sensing (TyWRRS)*, pp. 164-171, 2012.

[119] E. M. Domínguez, C. Magnard, M. Frioud, D. Small, and E. Meier, "Adaptive Pulse Compression for Range Focusing in SAR Imagery," *IEEE Transactions on Geoscience and Remote Sensing*, vol. 55, no. 4, pp. 2262-2275, 2017.

[120] E. M. Domínguez, E. Meier, D. Small, M. E. Schaepman, L. Bruzzone, and D. Henke, "A Multisquint Framework for Change Detection in High-Resolution Multitemporal SAR Images," *IEEE Transactions on Geoscience and Remote Sensing*, vol. 56, no. 6, pp. 3611 - 3623, 2018.

[121] P. Prats and J. J. Mallorqui, "Estimation of Azimuth Phase Undulations with Multisquint Processing in Airborne Interferometric SAR Images," *IEEE Transactions on Geoscience and Remote Sensing*, vol. 41, no. 6, pp. 1530-1533, 2003.

[122] C. Magnard, T. Brehm, H. Essen, and E. Meier, "High resolution MEMPHIS SAR data processing and applications," in *Progress in Electromagnetics Research Symposium (PIERS)*, Kuala Lumpur, Malaysia, 2012, pp. 328-332.

[123] K. Choi, I. Lee, and S. Kim, "A feature based approach to automatic change detection from Lidar data in urban areas," *Int. Arch. Photogramm. Remote Sens. Spat. Inf. Sci*, vol. 18, pp. 259-264, 2009.

[124] D. Rebolj, N. Č. Babič, A. Magdič, P. Podbreznik, and M. Pšunder, "Automated construction activity monitoring system," *Advanced engineering informatics*, vol. 22, no. 4, pp. 493-503, 2008.

[125] D. Ali-Sisto and P. Packalen, "Forest change detection by using point clouds from dense image matching together with a LiDAR-derived terrain model," *IEEE Journal of Selected*

Topics in Applied Earth Observations and Remote Sensing, vol. 10, no. 3, pp. 1197-1206, 2017.

[126] D. Marinelli, C. Paris, and L. Bruzzone, "A Novel Approach to 3-D Change Detection in Multitemporal LiDAR Data Acquired in Forest Areas," *IEEE Transactions on Geoscience and Remote Sensing*, 2018.

[127] T. Pollard and J. L. Mundy, "Change detection in a 3-D world," in *IEEE Conference on Computer Vision and Pattern Recognition, CVPR'07*, 2007, pp. 1-6.

[128] R. Qin, J. Tian, and P. Reinartz, "3D change detection–approaches and applications," *ISPRS Journal of Photogrammetry and Remote Sensing*, vol. 122, pp. 41-56, 2016.

[129] T. Zhang and M. Cen, "Robust DEM co-registration method for terrain changes assessment using least trimmed squares estimator," *Advances in Space Research*, vol. 41, no. 11, pp. 1827-1835, 2008.

[130] A. Sasagawa, K. Watanabe, S. Nakajima, K. Koido, H. Ohno, and H. Fujimura, "Automatic change detection based on pixel-change and DSM-change," *The International Archives of Photogrammetry, Remote Sensing and Spatial Information Sciences*, vol. 37 (Part B7), pp. 1645-1650, 2008.

[131] R. Qin and A. Gruen, "3D change detection at street level using mobile laser scanning point clouds and terrestrial images," *ISPRS Journal of Photogrammetry and Remote Sensing*, vol. 90, pp. 23-35, 2014.

[132] C. Yang, Y. Pang, and U. Soergel, "Monitoring of Building Construction by 4D Change Detection Using Multi-temporal SAR Images," *ISPRS Annals of Photogrammetry, Remote Sensing & Spatial Information Sciences*, vol. 4, 2017.

[133] M. A. Richards, "A Beginner's Guide to Interferometric SAR Concepts and Signal Processing [AESS Tutorial IV]," *IEEE Aerospace and Electronic Systems Magazine*, vol. 22, no. 9, pp. 5-29, 2007.

[134] X. X. Zhu and R. Bamler, "Demonstration of super-resolution for tomographic SAR imaging in urban environment," *IEEE Transactions on Geoscience and Remote Sensing*, vol. 50, no. 8, pp. 3150-3157, 2012.

[135] P. J. Besl and D. N. McKay, "A method for registration of 3-D shapes," *IEEE Trans. Pattern Anal. Mach. Intell.*, vol. 14, no. 2, pp. 239-256, Feb. 1992.

[136] O. Frey and E. Meier, "3-D time-domain SAR imaging of a forest using airborne multibaseline data at L-and P-bands," *IEEE Transactions on Geoscience and Remote Sensing*, vol. 49, no. 10, pp. 3660-3664, 2011.

[137] O. Frey, F. Morsdorf, and E. Meier, "Tomographic imaging of a forested area by airborne multi-baseline P-band SAR," *Sensors*, vol. 8, no. 9, pp. 5884-5896, 2008.

[138] F. Lombardini and F. Gini, "Model order selection in multi-baseline interferometric radar systems," *EURASIP Journal on Advances in Signal Processing*, vol. 2005, no. 20, pp. 3206-3219, 2005.

[139] P. Rosen *et al.*, "Synthetic aperture radar interferometry," *Proceedings of the IEEE*, vol. 88, no. 3, pp. 333-382, March 2000 2000.

[140] F. Lombardini and F. Cai, "Temporal decorrelation-robust SAR tomography," *IEEE Transactions on Geoscience and Remote Sensing*, vol. 52, no. 9, pp. 5412-5421, 2014.

[141] C.-A. Deledalle, L. Denis, G. Poggi, F. Tupin, and L. Verdoliva, "Exploiting patch similarity for SAR image processing: the nonlocal paradigm," *IEEE Signal Processing Magazine*, vol. 31, no. 4, pp. 69-78, 2014.

[142] C.-A. Deledalle, L. Denis, S. Tabti, and F. Tupin, "MuLoG, or How to apply Gaussian denoisers to multi-channel SAR speckle reduction?," *IEEE Transactions on Image Processing*, vol. 26, no. 9, pp. 4389-4403, 2017.

[143] S. Tebaldini, "Single and multipolarimetric SAR tomography of forested areas: A parametric approach," *IEEE Transactions on Geoscience and Remote Sensing*, vol. 48, no. 5, pp. 2375-2387, 2010.

[144] X. X. Zhu and R. Bamler, "Tomographic SAR inversion by L1-norm regularization-The compressive sensing approach," *IEEE Transactions on Geoscience and Remote Sensing*, vol. 48, no. 10, pp. 3839-3846, 2010.

[145] D. P. Huttenlocher, G. A. Klanderman, and W. J. Rucklidge, "Comparing images using the Hausdorff distance," *IEEE Transactions on pattern analysis and machine intelligence*, vol. 15, no. 9, pp. 850-863, 1993.

[146] M. Weinmann, B. Jutzi, S. Hinz, and C. Mallet, "Semantic point cloud interpretation based on optimal neighborhoods, relevant features and efficient classifiers," *ISPRS Journal of Photogrammetry and Remote Sensing*, vol. 105, pp. 286-304, 2015.

[147] C. Sutton and A. McCallum, "An introduction to conditional random fields," *Foundations and Trends in Machine Learning*, vol. 4, no. 4, pp. 267-373, 2012.

[148] J. Besag, "On the statistical analysis of dirty pictures," *Journal of the Royal Statistical Society. Series B (Methodological)*, pp. 259-302, 1986.

[149] C. Magnard, M. Frioud, D. Small, T. Brehm, H. Essen, and E. Meier, "Processing of MEMPHIS Ka-Band Multibaseline Interferometric SAR Data: From Raw Data to Digital Surface Models," *IEEE Journal of Selected Topics in Applied Earth Observations and Remote Sensing*, vol. 7, no. 7, pp. 2927-2941, 2014.

[150] C.-A. Deledalle, L. Denis, F. Tupin, A. Reigber, and M. Jäger, "NL-SAR: A unified nonlocal framework for resolution-preserving (Pol)(In) SAR denoising," *IEEE Transactions on Geoscience and Remote Sensing*, vol. 53, no. 4, pp. 2021-2038, 2015.

[151] M. Schmitt and U. Stilla, "Adaptive multilooking of airborne single-pass multi-baseline InSAR stacks," *IEEE Transactions on Geoscience and Remote Sensing*, vol. 52, no. 1, pp. 305-312, January 2014 2014.

[152] M. Schmitt, "Reconstruction of urban surface models from multi-aspect and multi-baseline interferometric SAR," Technische Universität München, 2014.

[153] D. Small, "Flattening gamma: Radiometric terrain correction for SAR imagery," *IEEE Transactions on Geoscience and Remote Sensing*, vol. 49, no. 8, pp. 3081-3093, 2011.

CURRICULUM VITAE

Elías Méndez Domínguez
12th March 1981
Spanish

Education

2014－2018 Ph.D. candidate University of Zurich (Switzerland), Department of Geography, Remote Sensing Laboratories (RSL). Thesis title: *Change Detection with Synthetic Radar Imagery*.

2008－2009 Master of Advanced Studies in Electromagnetic Engineering: Basics and Applications, Escuela Superior de Ingenieros de Telecomunicación, University of Vigo, Vigo (Spain).

1999－2006 Telecommunications Engineering, Escuela Superior de Ingenieros de Telecomunicación, University of Vigo, Vigo (Spain). M.S. degree title: *Propagation study of low radar targets*.

1995－1999 Secondary School, Colegio Marista Santa María, Ourense (Spain).

Professional experience

2010－2018 Scientific collaborator, University of Zurich, Department of Geography, Remote Sensing Laboratories (RSL), Zurich, Switzerland: SAR image processing and applications.

2009 FP6 Marie Curie Early Stage Research Training at THALES B.V. Surface Radar Unit and in cooperation with IRCTR-TUDelft in Delft, (Nederland): pulse compression of radar phase-coded and OFDM signals.

2008 Traineeship at the Sensors, Radar and Cyber-Security Unit of the Joint Research Centre of the European Commission, Ispra (Italy): MIMO SAR through wall imaging and electromagnetic characterization of building materials.

Graduate courses

- Promotion Seminar I & II
- Principles and Theory
- Graduate School Retreat I & II
- Scientific Writing
- Scientific Drawing
- Project Management
- Voice Training and Presentation Skills I & II

Oral contributions

- Photogrammetric Image Analysis (PIA), 2015, Munich, Germany.
- SPIE Remote Sensing (SPIE), 2015, Toulouse, France.

- Remote Sensing Colloquium, 2017, Zurich, Switzerland.
- 12th European Conference on Synthetic Aperture Radar (EUSAR), 2018, Aachen, Germany.

Teaching

- GEO 443, Lecture SAR III (2013 – 2017)

Publications

Peer-reviewed first author publications:

E. M. Domínguez, C. Magnard, M. Frioud, D. Small, and E. Meier, "Adaptive Pulse Compression for Range Focusing in SAR Imagery," *IEEE Transactions on Geoscience and Remote Sensing*, vol. 55, no. 4, pp. 2262-2275, 2017.

E. M. Domínguez, E. Meier, D. Small, M. E. Schaepman, L. Bruzzone, and D. Henke, "A Multisquint Framework for Change Detection in High-Resolution Multitemporal SAR Images," *IEEE Transactions on Geoscience and Remote Sensing*, 2018.

E. M. Domínguez, C. Magnard, E. Meier, D. Small, M. E. Schaepman, and D. Henke, "A Back-Projection Tomographic Framework for VHR SAR Image Change Detection," submitted to *IEEE Transactions on Geoscience and Remote Sensing*, 2018.

Other scientific publications

Peer-reviewed publications:

P. D'Odorico, A. Gonsamo, B. Pinty, N. Gobron, N. C. Coops, **E. Mendez**, and M. E. Schaepman, "Intercomparison of fraction of absorbed photosynthetically active radiation products derived from satellite data over Europe," *Remote sensing of environment*, vol. 142, pp. 141-154, 2014.

D. Henke, **E. M. Dominguez**, D. Small, M. E. Schaepman, and E. Meier, "Moving target tracking in single- and multichannel SAR," *IEEE Transactions on Geoscience and Remote Sensing*, vol. 53, no. 6, pp. 3146-3159, 2015.

D. Henke, **E. M. Dominguez**, D. Small, M. E. Schaepman, and E. Meier, "Moving Target Tracking in SAR Data Using Combined Exo-and Endo-Clutter Processing," *IEEE Transactions on Geoscience and Remote Sensing*, vol. 56, no. 1, pp-251-263, 2017.

Conference contributions:

E. M. Dominguez, D. Henke, D. Small, and E. Meier, "High Resolution Airborne SAR Image Change Detection in Urban Areas with Slightly Different Acquisition Geometries," *The International Archives of Photogrammetry, Remote Sensing and Spatial Information Sciences*, vol. 40, no. 3, p. 127, 2015.

E. M. Dominguez, D. Henke, D. Small, and E. Meier, "Fully polarimetric high-resolution airborne SAR image change detection with morphological component analysis," in *Image and Signal Processing for Remote Sensing XXI*, 2015, vol. 9643, p. 964312: International Society for Optics and Photonics.

E. M. Dominguez, M. Frioud, D. Small, and D. Henke, "Range Adaptive Processing and Multisquint Processing Mode for SAR Image Change Detection," in *12th European Conference on Synthetic Aperture Radar (EUSAR)*, Aachen, Germany, 2018.

Reports (report authors listed in alphabetical order):

M. Frioud, C. Magnard, E. Meier, and **E. Méndez Domínguez**, "Annual report 2011: Development of a Modular and Flexible SAR Processor," in *Report to the Federal Authorities of the Swiss Confederation*, Remote Sensing Laboratories, Department of Geography, University of Zurich, Zurich, Switzerland, 2012.

M. Frioud, C. Magnard, E. Meier, and **E. Méndez Domínguez**, "Annual report 2012: Development of a Modular and Flexible SAR Processor," in *Report to the Federal Authorities of the Swiss Confederation*, Remote Sensing Laboratories, Department of Geography, University of Zurich, Zurich, Switzerland, 2013.

M. Frioud, C. Magnard, E. Meier, **E. Méndez Domínguez**, and A. Schubert, "Annual report 2012: SAR Signatures," in *Report to the Federal Authorities of the Swiss Confederation*, Remote Sensing Laboratories, Department of Geography, University of Zurich, Zurich, Switzerland, 2013.

M. Frioud, C. Magnard, E. Meier, **E. Méndez Domínguez**, and A. Schubert, "Annual report 2013: SAR Signatures," in *Report to the Federal Authorities of the Swiss Confederation*, Remote Sensing Laboratories, Department of Geography, University of Zurich, Zurich, Switzerland, 2014.

M. Frioud, C. Magnard, E. Meier, and **E. Méndez Domínguez**, "Annual report 2014: Development of a Modular and Flexible SAR Processor," in *Report to the Federal Authorities of the Swiss Confederation*, Remote Sensing Laboratories, Department of Geography, University of Zurich, Zurich, Switzerland, 2015.

M. Frioud, C. Magnard, E. Meier, **E. Méndez Domínguez**, and A. Schubert, "Annual report 2014: SAR Signatures," in *Report to the Federal Authorities of the Swiss Confederation*, Remote Sensing Laboratories, Department of Geography, University of Zurich, Zurich, Switzerland, 2015.

M. Frioud, C. Magnard, E. Meier, **E. Méndez Domínguez**, and A. Schubert, "Annual report 2015: SAR Signatures," in *Report to the Federal Authorities of the Swiss Confederation*, Remote Sensing Laboratories, Department of Geography, University of Zurich, Zurich, Switzerland, 2016.

J. Fagir, M. Frioud, C. Magnard, E. Meier, **E. Méndez Domínguez**, and A. Schubert, "Annual report 2016: SAR Signatures," in *Report to the Federal Authorities of the Swiss Confederation*, Remote Sensing Laboratories, Department of Geography, University of Zurich, Zurich, Switzerland, 2017.

J. Fagir, M. Frioud, D. Henke, E. Meier, **E. Méndez Domínguez**, and A. Schubert, "Annual report 2017: SAR Signatures," in *Report to the Federal Authorities of the Swiss Confederation*, Remote Sensing Laboratories, Department of Geography, University of Zurich, Zurich, Switzerland, 2018.

ACKNOWLEDGMENTS

This dissertation was funded by armasuisse W+T. I would like to thank the staff for their financial, technical and logistical support, and in particular to Peter Wellig for the long standing support of the SARLab, for the organization of the measurement campaigns, and for the freedom given to perform my research.

A special thank you goes to my former supervisor Erich Meier. He supported my work with his ideas and motivation. I am very thankful for his confidence in me, for always being available to discuss new research projects and ideas, for providing the contacts and founding sources of the projects involved in this thesis, and for transmitting his passion and enthusiasm in SAR related topics.

I would to thank my current supervisor Daniel Henke, for the technical support, research ideas and supervision. I am also very grateful for his guidance when writing the papers, for improving my critical thinking and showing me a more scientific perspective of my work. Thank you also for the nice time spent in the coffee breaks, the jokes exchanged and good tips in sports related topics.

I would like to express my gratitude to Michael E. Schaepman for his support, good advice and suggestions, and also for giving me the opportunity to join the SARLab team. Thank you for helping me with your knowledge in remote sensing and with your experience in the publication procedure as well as when writing this thesis.

I also wish to thank David Small and Adrian Schubert for sharing their knowledge and experience on SAR calibration related issues, for their contribution to my research, and for their revisions of the manuscripts. I also thank Lorenzo Bruzzone for fruitful discussions in the progress meetings and also for his technical support and advice.

I would like to thank my colleagues at SARLab. My special thanks to Christophe Magnard and Max Frioud who greatly contributed to parts of this work with their technical knowledge, experience and advice. Thank you also for the nice coffee breaks and conversations at lunch time. Many thanks to Julian Fagir, Emiliano Casalini, and Christoph Rohner for the good atmosphere in the office, for the good moments at lunch or in the coffee breaks, when playing kicker and for their friendship. Many thanks to my fellows at RSL for the nice moments and work environment.

I also wish to thank Rita Ott, Sandra Altorfer, and Bruno Weber for their kindness and for the time spent helping me to get in contact with the Swiss administration and society, for informatics related issues, and also for their characteristic good mood and willingness to help.

I would like to thank the SAR Technology Department of the Microwaves and Radar Institute at the German Aerospace Center DLR, in particular, Jens Fischer and Andreas Reigber for the cooperation, organization and execution of the measurement campaigns with the F-SAR sensor, and for their willingness to answer my questions and provide technical support with the F-SAR sensor.

Finally, I would like to extend my thanks to my friends, and above all I would like to thank my family for their never-ending support and for all of the sacrifices made to support my career and life. Special thanks to my dad, because this work would have not been possible without him.

Thank you all !!